MEASUREMENT OF THE CP ASYMMETRY IN SEMIMUONIC B DECAYS PRODUCED IN $P\overline{P}$ COLLISIONS AT $\sqrt{S} = 1.96$ TEV

BY

CHRISTOPHER PHILLIP MARINO

B.S., University of Memphis, 2000
B.A., University of Memphis, 2000
M.S., University of Illinois at Urbana-Champaign, 2002

DISSERTATION

Submitted in partial fulfillment of the requirements
for the degree of Doctor of Philosophy in Physics
in the Graduate College of the
University of Illinois at Urbana-Champaign, 2007

Urbana, Illinois

Doctoral Committee:

Professor Mats Selen, Chair
Professor Kevin Pitts, Director of Research
Professor John Stack
Professor Matthias Grosse Perdekamp

Abstract

We measure the asymmetry between positive and negative same-sign muon pairs originating from semileptonic decays of pairs of B hadrons. Low transverse momentum dimuon pairs are evaluated to determine B hadron content using a log likelihood fit to two-dimensional impact parameter significance templates. Corrections are made for asymmetries arising from the detector, trigger, and hadrons which are reconstructed as muons. Using 1.1 million muon pairs from data corresponding to an integrated luminosity of 1.6 fb^{-1}, we find 210,000 same-sign muon pairs with both muon candidates coming from B decays. After corrections, we measure a semileptonic asymmetry from neutral B mixing of $A_{SL} = 0.0080 \pm 0.0090(stat) \pm 0.0068(syst)$. This asymmetry can be interpreted as a constraint on the complex phase of the CKM matrix element V_{ts} by using the B^0 neutral mixing contribution measured at the B factories. We measure the CP violating asymmetry from B_s mixing to be $A^s_{SL} = 0.020 \pm 0.028$.

For by Him all things were created, both in the heavens and on earth, visible and invisible... He is before all things, and in Him all things hold together.

Acknowledgments

I would like to thank Vyacheslav Krutelyov for his assistance in determining the trigger efficiencies for our specific requirements in this analysis. Thanks to Alberto Annovi, Stefano Torre and Paolo Giromini for providing Herwig templates and other cross-checks of this analysis. I also thank Jonathan Lewis, Paolo Giromini, Petar Maksimovic, Sandro De Cecco, Sinead Farrington, Diego Tonelli, Cheng-Jun Lin, Manfred Paulini, and Marco Rescigno who provided thoughtful assistance in evaluating and checking the analysis methods. Thanks to Mike Kasten, Jonathan Lewis, Tom Wright, and Simone Donati for helping to commission the Track Trigger Upgrade project.

I appreciate the University of Illinois for giving me the opportunity and experience of completing this doctoral thesis. Thanks to Wendy Wimmer, Donna Guzy, Rene Dunham, and Tonya Ayers for helping me to navigate all the details of funding and university requirements. Thanks to Professor Jim Wolfe for helping me manage a very necessary semester off without getting off track. I would also like to thanks fellow grad students Andrea Esler, Peter Doksus, Ulysses Grundler, Jim Kraus, Ed Rodgers, Alice Bridgeman, Sarah Budd, and Greg Thompson for their help and sympathy in classwork, analysis research, hardware commisioning and maintaining sanity. This thesis was also supported in part by the United States Department of Energy under grant DE-FG02-91ER40677.

I would like to thank my advisor, Kevin Pitts, for all the time, insight and encouragement he invested in my research at the University of Illinois. I would certainly never have survived the difficulties of a large collaboration and learning so many new things all at once without his direction, steadiness, and practicality. It his certainly to his credit to have advised one who knew so little about elementary particle physics and computer programming to the completion of a dissertation which drew so heavily on both.

Thanks to Anyes Taffard who helped me get on my feet in understanding CDF software and data, and who also provided so much assistance with the XTRP and Track Trigger Upgrade. Thanks to Heather Gerberich for many enjoyable talks and rallying round to help me complete the final pieces of the analysis and documentation. I also appreciate Olga Norniella taking over the XTRP maintanence so I could write this thesis.

My family has been a great support in the process of coming to and surviving graduate school. Despite the fact that they rarely had any idea what I was talking about, they listened to my progess, and they encouraged and prayed for me. My mom and dad have provided wisdom, perspective, and joy. My daughter Ruth while not actually contributing materially, and sometimes depriving me of much needed sleep has, however, been a source of delight, pride, and motivation for efficiency.

My lovely bride Damaris has been a great strength, a faithful prayer, and a loving encourager. She has endured much uncertainty, many inopportune XTRP pages, and an often captious husband. I truly appreciate her belief in my abilities, her patience with me, and her fulfillment of her promise to share all my sorrows and all my joys.

Table of Contents

List of Tables

List of Figures

Chapter 1

Introduction

The study of b quark physics began with discovery of the Υ meson at Fermi National Laboratory Accelerator (Fermilab) in Batavia, Illinois in 1977 [1]. The b quark is unique and interesting in that it is both massive and comparatively long-lived. Measured to be on the order of 100 times heavier than the similar d quark, and nearly 5 times as massive as a proton, the b cannot decay within its quark family, *i.e.* to the more massive top. Thus it must decay via the weak interaction, generally to charm, giving it a long, observable lifetime.

B mesons are bound states of a b quark and a lighter quark. B decays can provide information about five of nine elements of the Cabibbo-Kobayashi-Maskawa (CKM) matrix which governs flavor-changing weak decays, and CP violation is expected to be large for a number of B decay modes some of which have now been observed. This thesis presents a measurement of CP asymmetry in B decays. This measurement helps constrain a complex phase of CKM matrix element which has not been well probed. A value inconsistent with zero would be an indication of CP violation beyond the physics of described by the Standard Model.

1.1 Fundamental Particles

Though questions and theories concerning the fundamental building blocks of matter date top the ancient Greek philosophers, the modern subject of elementary particle physics is said to have begun with J.J. Thompson's observation of the electron in 1897. During the following decades new particles were discovered - mostly in cosmic ray experiments - and the theory of quantum electrodynamics was developed by Dirac. This theory laid the theoretical foundation to an understanding of elementary particle physics and predicted the existence of antimatter which was observed shortly thereafter. In the 1950s particle accelerators and new detectors were being developed. Even more new particles were discovered leading to uncertainty as to whether so many could be really fundamental. In 1961, Murray Gell-Mann and George Zweig organized the known baryons in a way that suggested they were all composed of a few true, as of yet unobserved, fundamental particles which Gell-Mann named quarks [2]. Like Dirac's prediction of the positron, the quark theory predicted the existence of a new baryon, the Ω^-, and it was discovered several years later. After this, the existence of additional quarks were observed, the theory of quantum electrodynamics(QED) [3] was expanded to include the weak interaction, and quantum chromodynamics(QCD) [4], governing strong interactions, was developed. These ideas and discoveries came together to form the Standard Model of particle physics which has

been highly successful in describing almost all experimental observations in elementary particle physics. The Standard Model has survived years of precision testing at the highest available energies, and in 1995 the top quark it predicted was observed at Fermilab.

1.2 The Standard Model

The Standard Model of particle physics describes all matter as constructed from twelve elementary particles - six quarks and six leptons. These quarks and leptons are fermions with spin values of $\frac{1}{2}$. They can be grouped into three generations or families as is shown in Table 1.1 which lists their properties. The leptons each carry integral electric charge, 0 or 1, while the quarks carry a fractional charge of either $+\frac{2}{3}$ or $-\frac{1}{3}$ (in units of the charge of the electron, e). Each particle has a corresponding antiparticle with the same mass and lifetime but opposite charge and magnetic moment.

Particle	Charge	1st generation	2nd generation	3rd generation
quarks	$+\frac{2}{3}$	up, u	charm, c	top, t
	$-\frac{1}{3}$	down, d	strange, s	bottom, b
leptons	-1	electron, e	muon, μ	tau, τ
	0	electron neutrino, ν_e	muon neutrino, ν_μ	tau neutrino, ν_τ

Table 1.1: Elementary building blocks of matter.

Interactions between particles are governed by nature's four fundamental forces. The electromagnetic force and the weak force can be described by a quantum field theory with local gauge invariance. The unified electroweak model, QED, and a corresponding gauge theory describing the strong force, QCD, form the basis for Standard Model interactions. Forces are mediated by carriers called gauge bosons which arise from the framework of the gauge theories; the carriers are listed in Table 1.2. Gravity, the weakest of the fundamental forces is not described by the Standard Model because no such theory has yet been established for gravity.

Force	Carrier	Spin/Parity
Electromagnetic	photon, γ	1^-
Weak	$W^\pm$	1^-
	Z^0	1^+
Strong	gluon, g	1^-

Table 1.2: Fundamental force carriers of the Standard Model

In addition to the omission of gravity, other questions persist despite the overwhelming success of the Standard Model. For example, the origin of mass, and the existence of neutrino mass has not been described by the Standard Model. Also, there is no mechanism to fully account for the

asymmetry of matter and antimatter evident in our universe - as discussed further in Section 1.5 - providing motivation to search for CP asymmetry beyond the Standard Model.

1.3 The CKM Matrix

The quark mixing matrix found in the Standard Model Lagrangian, called the Cabibbo-Kobayashi -Maskawa(CKM) matrix, V_{CKM} is a 3 × 3 unitary matrix [5, 6]. The CKM matrix represents weak eigenstates which are rotated flavor eigenstates, and the matrix elements are the interaction couplings of the weak boson $W^{\pm}$ to the quarks,

$$V_{CKM} = \begin{pmatrix} V_{ud} & V_{us} & V_{ub} \\ V_{cd} & V_{cs} & V_{cb} \\ V_{td} & V_{ts} & V_{tb} \end{pmatrix}. \tag{1.1}$$

The CKM matrix is parameterized using the four free parameters determined by its unitarity. A standard parameterization choice uses three mixing angles θ_{12}, θ_{13}, and θ_{23} and a complex phase responsible for CP violation, δ. Using the abbreviations $s_{ij} = \sin\theta_{ij}$ and $c_{ij} = \cos\theta_{ij}$ the CKM matrix can be written as [7],

$$V_{CKM} = \begin{pmatrix} c_{12}c_{13} & s_{12}c_{13} & s_{13}e^{-i\delta} \\ -s_{12}c_{23} - c_{12}s_{23}s_{13}e^{-i\delta} & c_{12}c_{23} - s_{12}s_{23}s_{13}e^{-i\delta} & s_{23}c_{13} \\ s_{12}s_{23} - c_{12}c_{23}s_{13}e^{-i\delta} & -c_{12}s_{23} - s_{12}c_{23}s_{13}e^{-i\delta} & c_{23}c_{13} \end{pmatrix}. \tag{1.2}$$

Another parameterization was suggested by Wolfenstein [8]. This representation is motivated by experimental evidence that the matrix elements were on the order of different powers of the Cabibbo angle, θ_c. The parameters A,ρ,λ, and η are free inputs determined by experiment where

$$V_{CKM} = \begin{pmatrix} 1 - \lambda^2/2 & \lambda & A\lambda^3(\rho - i\eta) \\ -\lambda & 1 - \lambda^2/2 & A\lambda^2 \\ A\lambda^3(1 - \rho - i\eta) & -A\lambda^2 & 1 \end{pmatrix} + \mathcal{O}(\lambda^4). \tag{1.3}$$

The Wolfenstein parameterization is an approximation but is correct to the order λ^4 where $\lambda = \sin(\theta_c) \simeq 0.22$ [9]. Figure 1.1 shows the most commonly used triangle constructed using the Wolfenstein parameterization and the unitarity condition given by equation 1.4 [10].

$$V_{ud}V_{ub}^* + V_{cd}V_{cb}^* + V_{td}V_{tb}^* = 0 \tag{1.4}$$

The CKM matrix is essential to understanding electroweak b physics, and in particular it makes particle-antiparticle oscillations possible [11]. One major goal of flavor physics to measure and constrain the CKM elements which define fundamental Standard Model parameters. Current experimental constraints on the CKM parameters in the unitary triangle plane are shown in Figure 1.2. The uncertainty for all of the measurements displayed in Figure 1.2 is dominated by theoretical rather than experimental uncertainty with the exception of $\sin 2\beta$. A number of experiments have measured $\sin 2\beta$, but the most precise ones have come recently from the B

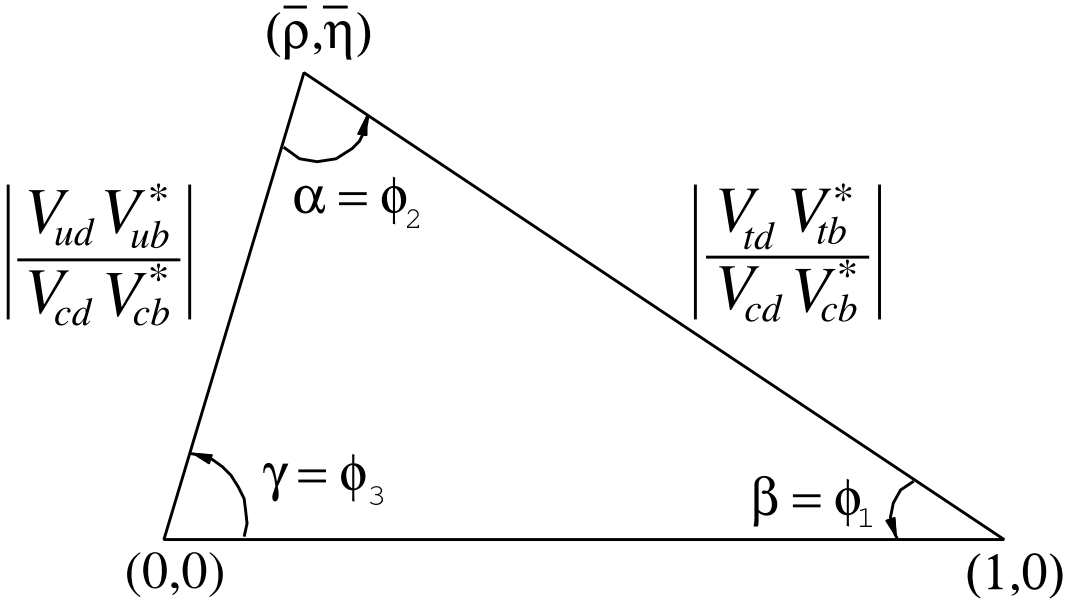

Figure 1.1: Triangle representation of the unitarity of the CKM Matrix using ρ and η from the Wolfenstein parameterization.

factories [12]. In Figure 1.2 the combined world average of $\sin 2\beta$ places a constraint on the CKM angle β which is shown as a shaded ray with its uncertainty along the right triangle side. Here

$$\beta = \phi_1 = \arg\left(-\frac{V_{cd}V_{cb}^*}{V_{td}V_{tb}^*}\right) \tag{1.5}$$

as shown in Figure 1.1. Similarly, the world average measured values of the neutral B mixing mass differences[1], Δm_d and Δm_s are displayed as an annulus in Figure 1.2 with their uncertainties constraining the length on the same side of the unitary triangle [13].

Lifting the constraints of the Standard Model increases the parameters which would describe the various mixing measurements. One standard example is that of a fourth generation. If there are fundamental and unobserved quarks and leptons, there is no reason for the current CKM matrix to be unitary. By combining a number of measurements in manner shown in Figure 1.2, CKM unitarity can be over-constrained giving an indication of the existence of physics beyond the Standard Model.

In regard to constraining the CKM matrix, this dissertation is concerned primarily with the complex phase of V_{ts}. In the Standard Model this is expected to be very small and does not even appear to the order λ^3 in the commonly used Wolfenstein CKM parameterization. However, from the full parameterization it can be seen that a complex phase is expected, and contributions from beyond the Standard Model may cause the phase to be larger than expectations. Since the complex phase of V_{ts} is poorly constrained it is a promising place to search for new physics.

[1] Described in Section 1.4

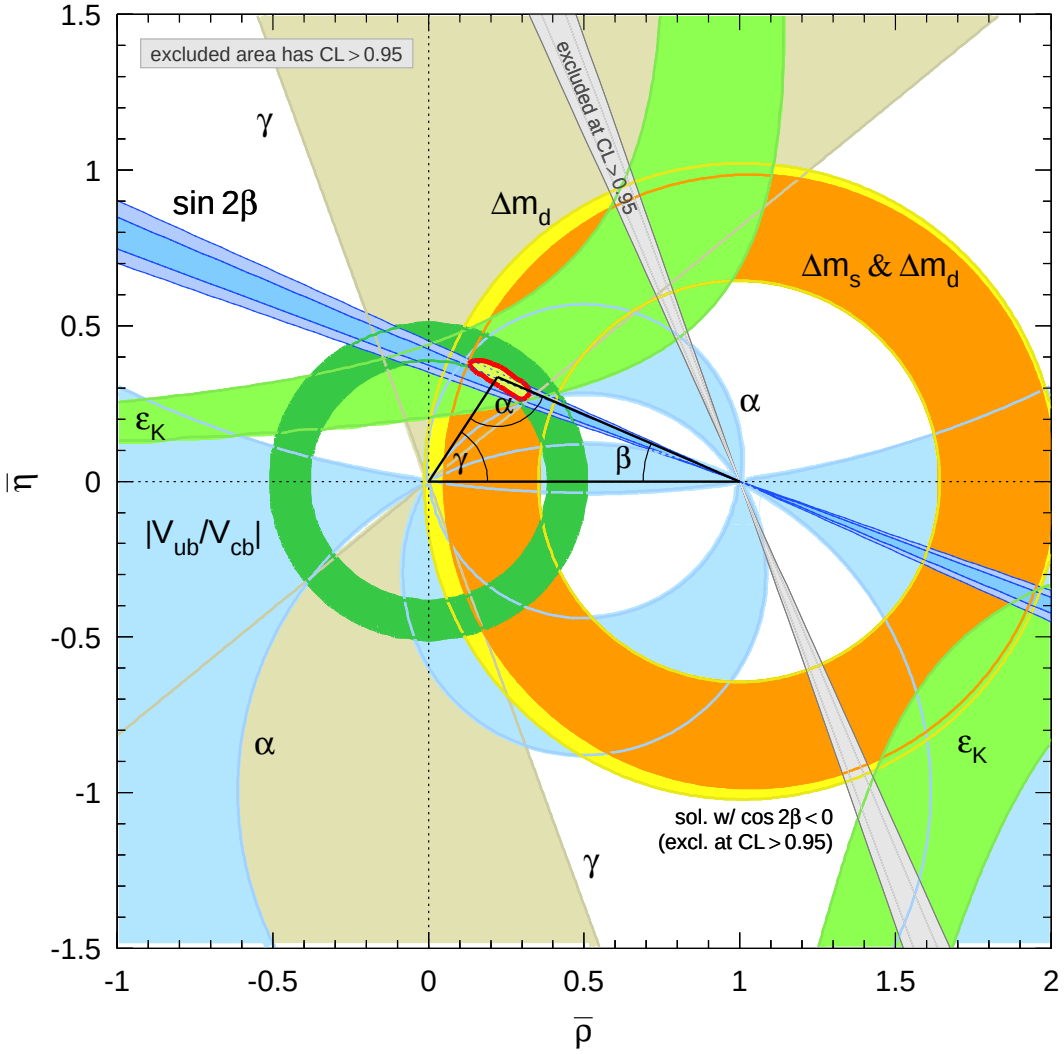

Figure 1.2: Experimental constraints on the $\rho - \eta$ plane as of the 2006 PDG.

1.4 Neutral Meson Mixing

In 1956, Lande at Brookhaven found the long lived weak eigenstate kaon predicted by the quantum-mechanical mixing developed by Gell-Mann and Pais the previous year [9, 14, 15]. In addition to neutral kaon mixing, $B^0\overline{B}^0$ and $B_s^0\overline{B}_s^0$ meson pairs also oscillate, where $B^0 = |\bar{b}d\rangle$ and $\overline{B}_s^0 = |b\bar{s}\rangle$. Neutral D meson mixing, expected to be very small in the Standard Model, was thought for some time to be absent entirely or perhaps too small to be observable due to the Cabibbo suppression of the D meson oscillation processes but not of D meson decay processes [10, 16]. However, the some recent publications suggest evidence for $D^0 - \overline{D}^0$ oscillations [17, 18].

1.4.1 B Meson Mixing

Neutral B mesons have been observed by several high energy experiments and measured to very high precision [10]. B_s mesons have been known to oscillate very quickly for sometime, but had not until recently been measured. In 2006 $D0$ reported the first bound on the B_s mixing frequency [19], and a few months later CDF observed B_s oscillations and measured $|V_{ts}|$ with high experimental precision [20]. The magnitude of B meson flavor mixing was an important parameter to measure for theoretical aspects of the Standard Model, and its determination was one of the major goals of the Tevatron Run II physics program. In the CDF measurement of B_s mixing frequency (shown in Figure 1.3), only the magnitude of CKM element $|V_{ts}|$ is determined and the complex phase due to CP violation is not constrained.

1.4.2 Mixing Formalism

As in the neutral kaon system, the off diagonal matrix elements cause flavor changing and give nonzero contributions for $B^0 \to \overline{B}^0$ and $B_s^0 \to \overline{B}_s^0$. Second-order W-exchange processes are responsible for neutral this mixing in the Standard Model (see example in Figure 1.4). Mixing probability is derived by defining eigenstates of a standard mixing Hamiltonian defined as $\mathbf{M} - \frac{i}{2}\mathbf{\Gamma}$ and allowing them to evolve in time as in [9, 21]. The states are identified as heavy, H, and light, L.

$$\begin{aligned} |B_H\rangle &= p\,|B^0\rangle - q\,|\overline{B}^0\rangle \\ |B_L\rangle &= p\,|B^0\rangle + q\,|\overline{B}^0\rangle \end{aligned} \tag{1.6}$$

This is the most general characterization of B^0 mixing eigenstates[2], but of interest is the limit $q = p = \frac{1}{\sqrt{2}}$ where CP is invariant[3] and the vectors are normalized. Including decay probability and phase time dependence in a state initially B^0, at time t the state is defined as

$$|\Psi(t)\rangle = \frac{1}{\sqrt{2}}\left(e^{-im_L t - t/2\tau_L}|B_L\rangle + e^{-im_H t - t/2\tau_H}|B_H\rangle\right) \tag{1.7}$$

[2] B_d mixing will be used exclusively for now, but the B_s formalism is identical.

[3] CP violation will be addressed in the following section, but is predicted to be small by the Standard Model and existing measurements.

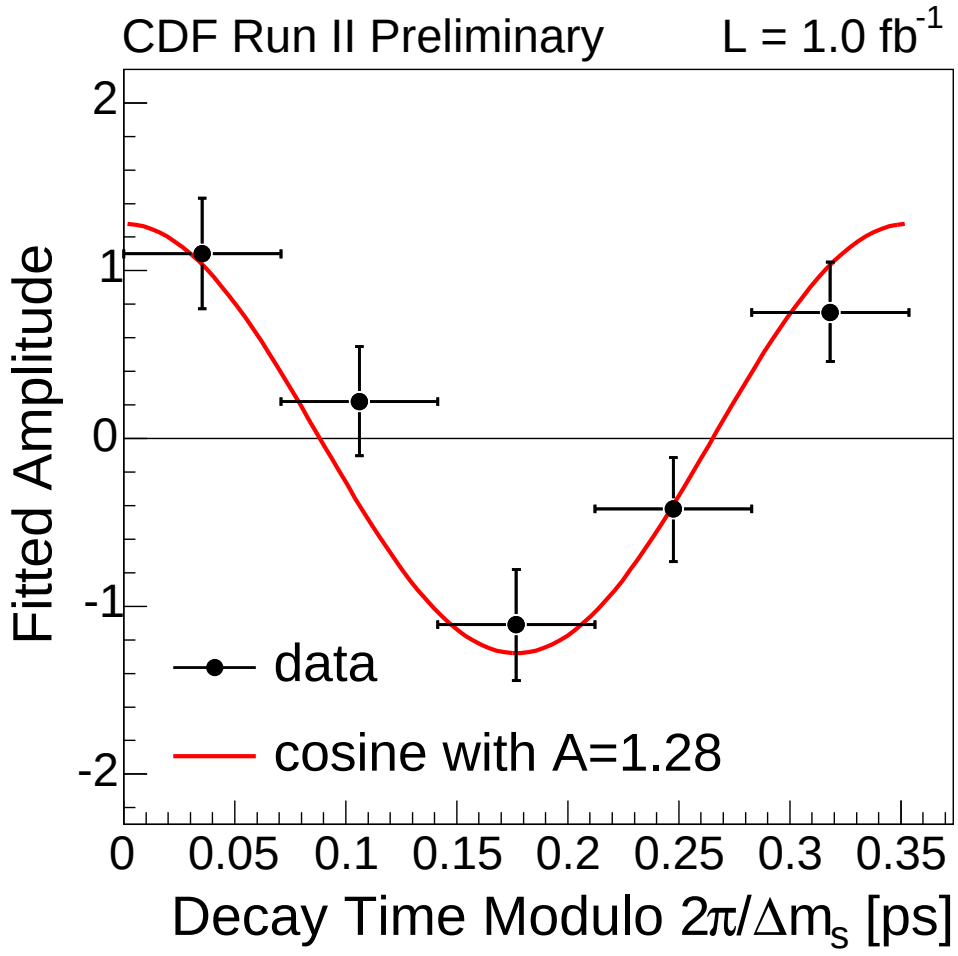

Figure 1.3: The time domain plot of $B_s\overline{B}_s$ oscillations. Five bins of proper decay time modulo the observed oscillation period $2\pi/\Delta m_s$.

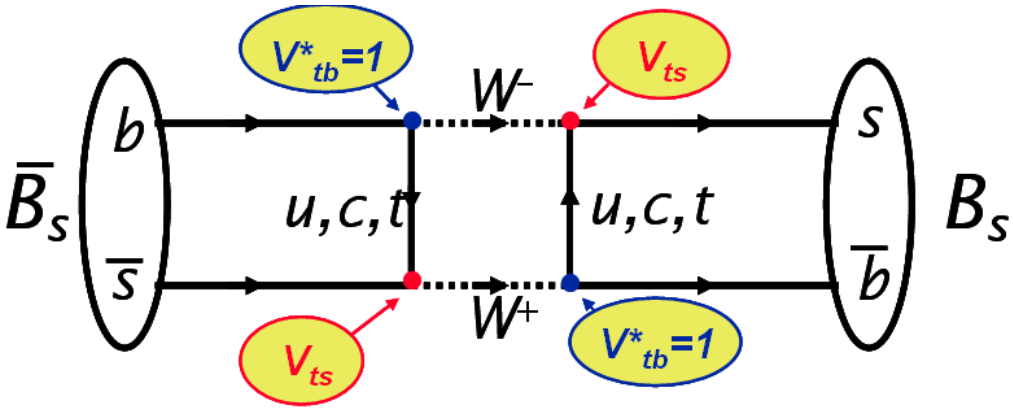

Figure 1.4: One of the lowest order Feynman diagrams contributing to B_s mixing. Also contributing is the box diagram with W and quark sides transposed. The processes are identical for B^0 mixing.

where m_L, and m_H are masses of each state, and τ_L, τ_H are the lifetimes. Now the probability of mixing can be found by taking $|\langle\overline{B}^0|\Psi(t)\rangle|^2$. Defining $\Delta m = m_H - m_L$ and $\Gamma = (\Gamma_H + \Gamma_L)/2$, where Γ_H is the decay width equal to $1/\tau_H$, we have

$$Prob(B^0 \to \overline{B}^0, t) = \frac{1}{2}e^{-\Gamma t}[1 - \cos(\Delta m t)] \tag{1.8}$$

This equation includes the assumptions that CP violation in the mixing is small and the lifetime difference $\Delta\Gamma = \Gamma_H - \Gamma_L$ is negligible. In the Standard Model $\Delta\Gamma/\Gamma$ for the B_d system is expected to be below 1%, but is predicted to be on the order of 10% for $\Delta\Gamma_s/\Gamma_s$ [10]. Under these assumptions, we can write

$$\Delta m = 2|M_{12}|, \quad \Delta\Gamma = 2\frac{\Re(M_{12}\Gamma_{12}^*)}{|M_{12}|}. \tag{1.9}$$

Then using the theoretical calculation for the dispersive part of the box diagram in the approximation that the t quark dominates [22], the off-diagonal element of the mass matrix is

$$M_{12} = -\frac{G_F^2 m_W^2 \eta_B m_{B^0} B_{B^0} f_{B^0}^2}{12\pi^2} S_0\left(\frac{m_t^2}{m_W^2}\right)(V_{td}^* V_{tb})^2 \tag{1.10}$$

where G_F is the Fermi constant, m_W and m_t the masses of the W boson and top quark, and m_{B^0}, f_{B^0}, and B_{B^0} are the mass, weak decay constant and bag parameter of the B^0 meson respectively. The $S_0(x)$ is a known function well approximated by $0.784x^{0.76}$, and η_B is a QCD correction on the order of 0.6 [9, 10]. Equations 1.9 and 1.10 can be combined to relate the mass difference to the CKM matrix elements,

$$\Delta m_d = \frac{G_F^2 m_W^2 \eta_B m_{B^0} B_{B^0} f_{B^0}^2}{6\pi^2} S_0\left(\frac{m_t^2}{m_W^2}\right)|V_{td}^* V_{tb}|^2. \tag{1.11}$$

The derivation of the mass difference for B_s^0 mixing, Δm_s is the same.

1.4.3 Time-integrated Mixing Parameter

χ_d is defined as the parameter resulting from the mixing probability being integrated over all time. Using integration by parts χ_d can be simplified to a form containing the ratio of the mass difference between the weak eigenstates, Δm_d, and average widths of the weak eigenstates, Γ_d. The exponential decay term ensures that χ_d is non-zero for $\Delta m_d \neq 0$, and we find

$$\chi_d = \frac{x_d^2}{2(1+x_d^2)}. \tag{1.12}$$

Here $x_d = \Delta m_d/\Gamma_d$, and this definition of χ_d is important for evaluating CKM matrix elements. χ_d can also be defined in terms of leptons produced through the decay of a mixed B hadron compared to all leptons produced from b decay

$$\chi_d = \frac{\Gamma(B^0 \to \overline{B^0} \to \mu^+ X)}{\Gamma(B \to \mu X)}. \tag{1.13}$$

The formalism is the same to find the time-integrated mixing parameter for B_s mixing, χ_s. Averaging over flavors, as both B_d and B_s are produced, χ_0[4] is defined as follows

$$\chi_0 = f_d \cdot \chi_d + f_s \cdot \chi_s. \tag{1.14}$$

Here f_d and f_s are the fractions of produced B_d and B_s mesons, and χ_s is the corresponding value for B_s^0 mixing. This leptonic decay definition of χ_0 is particularly significant as χ_0 cannot be measured directly, but produced lepton pairs are easily collected for analysis. In the case of no mixing, a $B\overline{B}$ pair will produce a pair of oppositely signed leptons through semileptonic decay. However, a B or $\overline{B}$ which mixes will produces a lepton of the same sign as its partner. Therefore, the measurable quantity of interest in the determination of a $B\overline{B}$ mixing magnitude is the ratio, R, of like-sign lepton pairs to the opposite sign lepton pairs all produced by b decay. There are four possibilities for a $b\overline{b}$ decay[5].

1. b mixes (prob. χ_0) and $\bar{\text{b}}$ decays normally (prob. $1-\chi_0$) producing like signs
2. b decays normally (prob. $1-\chi_0$) and $\bar{\text{b}}$ mixes (prob. χ_0) producing like signs
3. b mixes (prob. χ_0) and $\bar{\text{b}}$ mixes (prob. χ_0) producing opposite signs
4. b decays normally (prob. $1-\chi_0$) and $\bar{\text{b}}$ decays normally (prob. $1-\chi_0$) producing opposite signs.

For a sample of muons from only $b\overline{b}$ semileptonic decays χ_0 is related to R in the following way:

$$R = \frac{N(\mu^+\mu^+) + N(\mu^-\mu^-)}{N(\mu^-\mu^+)} = \frac{2\chi_0(1-\chi_0)}{\chi_0^2 + (1-\chi_0)^2} \tag{1.15}$$

[4] The time-integrated mixing parameter is also commonly referred to as $\overline{\chi}$, but we have reserved χ and $\overline{\chi}$ as the time-integrated mixing probabilities for neutral B and $\overline{B}$ hadrons respectively. χ_0 then is $\frac{1}{2}(\chi + \overline{\chi})$.

[5] In this discussion we are ignoring the contribution to same-sign muon pairs from sequential decays (discussed in Section 6.3) for simplicity. However, this is not a negligible contribution, and a more complete discussion of the issues and corrections in a measurement of χ_0 are discussed in Appendix F.

1.5 CP Violation

The evidence of the physical universe establishes a large matter-antimatter asymmetry. Charge-Parity (CP) violation is one of the necessary conditions for baryogenesis, or the generation of this asymmetry [23], and there are a number of models to describe CP violation [16, 24]. CP violation can be described in the Standard Model in terms of the CKM parameters [6]. The complex phase of the Yukawa couplings in the CKM matrix accurately accounts for the CP violation observed in the K and B meson systems described below, but fails to account to the cosmological asymmetry by several orders of magnitude [10].

1.5.1 CP Violation in K Mesons

CP violation was first observed in K meson decays [25]. The weak eigenstates had originally been thought to be CP eigenstates as well, but K_L with $CP = -1$ was observed to decay to a two pion final state with $CP = +1$. Since this was observed in the context of mixing it is indirect CP violation arising from the weak K eigenstates being an admixture of CP eigenstates to a degree quantified by the parameter ϵ [26]. Direct CP violation, that is arising from the decay process itself, has also been observed in the kaon system [27] but occurs at a level 3 orders of magnitude less than indirect CP violation.

1.5.2 CP Violation in B Mesons

The Standard Model predicted value for ϵ_B, the is on the order of 10^{-3} [10], but other theoretical models suggest a greater value, as in [28]. Also, direct CP violation which is expected to dominate in the B meson system [26], has been observed [29, 30].

The strong interaction produces pairs of b quarks and anti-quarks in high energy collisions. There is a large semileptonic branching ratio for B hadron decays; nearly 11% of B hadrons produced will decay in the following way,

$$b \to W^* c \to \mu^- \nu_\mu c. \tag{1.16}$$

Muons are also a clean signature on which events can be easily triggered. We expect to find pairs of semileptonic decays of these quarks where $b \to \mu^-$ and $\overline{b} \to \mu^+$ except when mixing occurs. By looking at events where only one b mixes, we can look for any residual asymmetry that may be evidence of CP violation.

A sample of same-sign muon pairs provides a constraint on the CP violating parameter ϵ_B, which is defined as $(1 - q/p)/(1 + q/p)$, where $q/p = 1$ is the limit for CP invariance from the mixing formalism. CP violation in B mixing results in different probabilities for B and $\overline{B}$ giving rise to an asymmetry of like sign dilepton events. For dimuons, the number of $\mu^+\mu^+$ would be different than the number of $\mu^-\mu^-$ for a sample of data where one of the B mesons has undergone mixing. This is defined as the CP violating charge asymmetry, A_{CP}, and it is related to ϵ_B in the following way:

$$A_{CP} = \frac{N(\mu^+\mu^+) - N(\mu^-\mu^-)}{N(\mu^+\mu^+) + N(\mu^-\mu^-)} = \frac{8(1-\overline{\chi})}{D}\left(f_d\chi_d\frac{Re\epsilon_d}{1+|\epsilon_d|^2} + f_s\chi_s\frac{Re\epsilon_s}{1+|\epsilon_s|^2}\right) \tag{1.17}$$

$$D = 2\overline{\chi}(1-\overline{\chi}) + 2f_{seq}\{\overline{\chi}^2 + (1-\chi)^2\}$$

Here, $\epsilon_{d,s}$ is the parameter ϵ_B for $B_{d,s}$ mixing. While the B factories have already made good measurements of ϵ_d in dimuon events [31], ϵ_s must be determined at the Tevatron.

1.5.3 CP Violating Phase of V_{ts}

CKM matrix element V_{ts} contains a complex phase which is suppressed by the λ^4, where λ is the Cabibbo angle.

$$V_{ts} = -\cos\theta_{12}\sin\theta_{23} - \sin\theta_{12}\cos\theta_{23}\sin\theta_{13}e^{-i\delta} \tag{1.18}$$

Standard Model(SM) plus existing measurements predicts CP violation in $B_s\overline{B_s}$ mixing at the order of 10^{-4}. A measurement larger than this could indicate CP violation from new physics processes. In 2006 $D\emptyset$ made the first high precision measurement, the results of their measurement are shown in Figure 1.5 [32]. This analysis uses a complimentary approach.

A method using the experimental determined results from the B factories for the A_{CP} from B_d mixing and the best known values for mixing probabilities and fragmentation fractions is outlined in [33] to extract A^s_{CP}.

We can then use the relation [34],

$$A^s_{CP} = \frac{\Delta\Gamma_s}{\Delta M_s}\tan\phi_s, \tag{1.19}$$

to relate the extracted asymmetry to the CP violating phase of in B_s mixing, ϕ_s, where [35]

$$\phi_s = \arg\left(\frac{-V_{tb}V^*_{ts}}{V_{cb}V^*_{cs}}\right). \tag{1.20}$$

1.6 $b\overline{b}$ Pair Production

Protons are not fundamental particles, and simple proton model includes two u quarks and one d quark. The proton is known, however, to also contain gluons by which the proton is held together, and sea quarks in addition to the three valence quarks. Sea quarks are $q\overline{q}$ pairs, general lighter quarks which can be produced from gluon splitting but annihilate back to a gluon. All of these constituents are referred to as partons, and all carry a fraction of the proton momentum and can play a role in $p\overline{p}$ QCD interactions.

In $p\overline{p}$ collisions, like those at the Tevatron $b\overline{b}$ pairs can be produced via several processes. Feynman diagrams for the leading order QCD interactions are shown in Figure 1.6 and are referred to as flavor creation processes. However, for inclusive b production in the kinematic

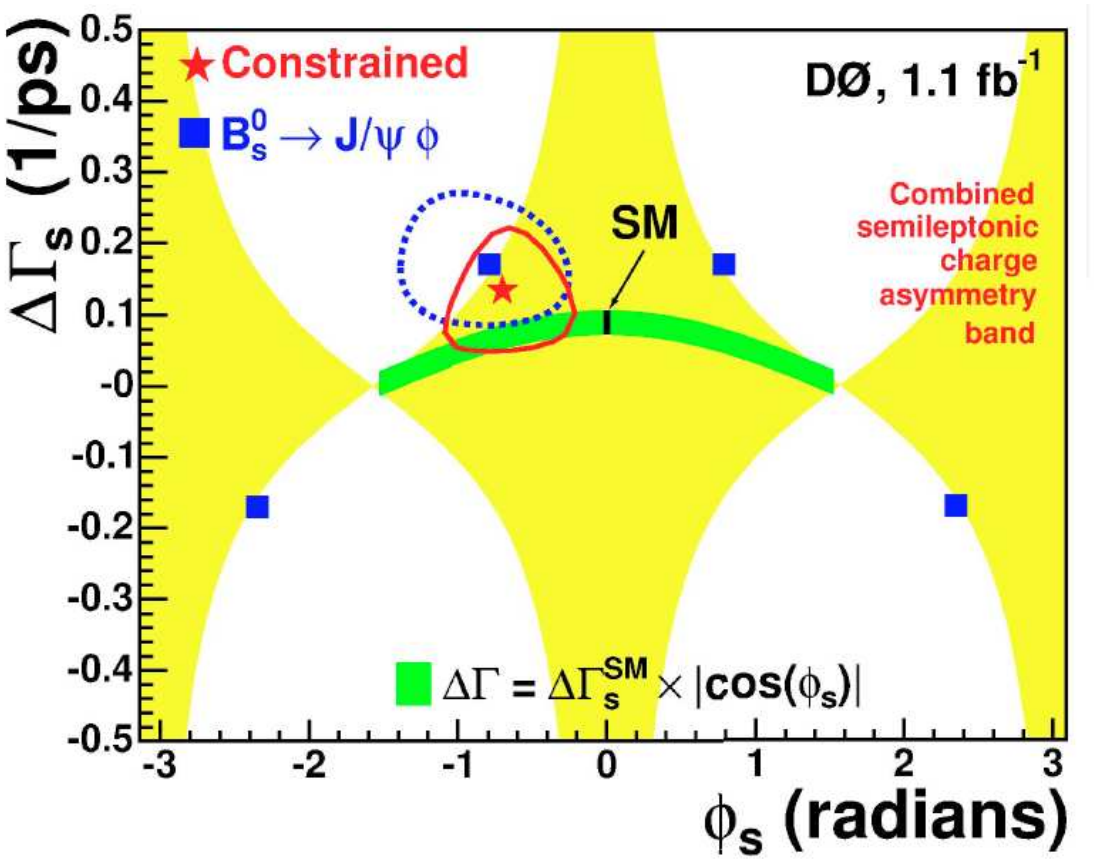

Figure 1.5: A combined fit showing the results of a measurement $\Delta\Gamma_s$ using $B_s \to J/\psi\phi$ decays constrained by the allowed contours in the $\Delta\Gamma_s - \phi_s$ plane as determined by the D0 measurement of A^s_{CP}.

range of interest for accurate reconstruction of the B hadron decay products, flavor creation accounts for less than 35% of $b\overline{b}$ pair production [36].

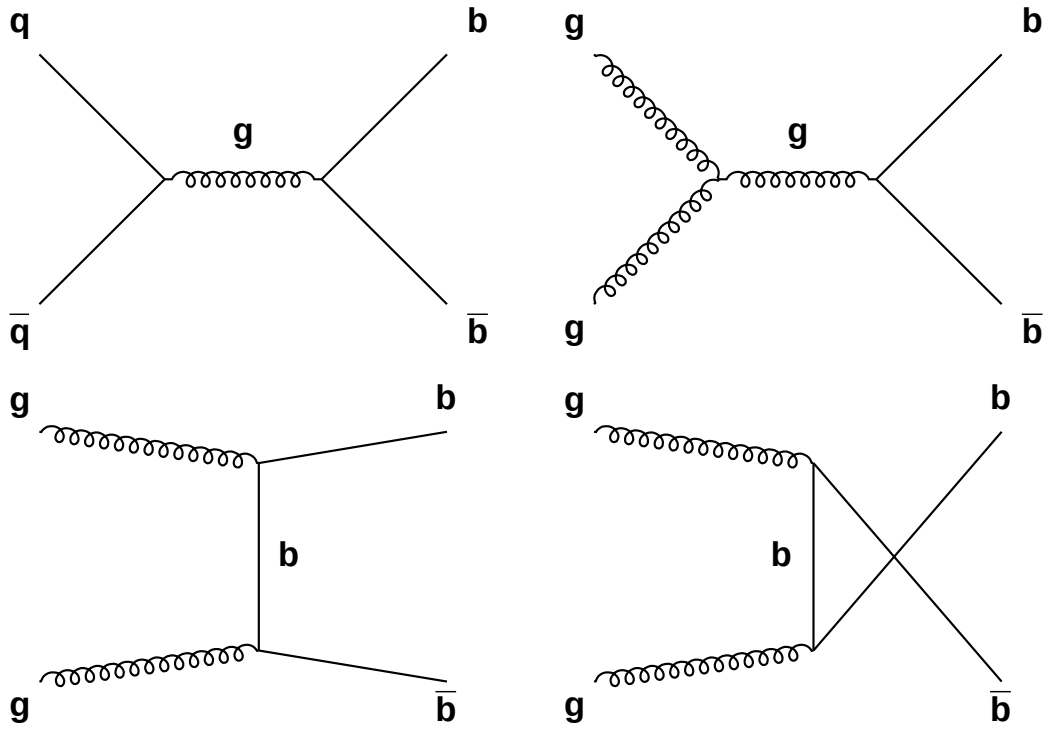

Figure 1.6: Feynman diagrams for leading order $b\overline{b}$ production processes. Flavor creation through $q\overline{q}$ annihilation and gluon fusion.

Next-to-leading order (NLO) $b\overline{b}$ production includes the flavor creation processes with gluon radiation in the final state. Also, included in NLO processes are flavor excitation which is the dominant process for inclusive production of b quarks with a transverse momentum > 5 GeV in the central detector, and gluon splitting which is only a significant mode of production at low transverse momentum. Feynman diagrams for these $b\overline{b}$ production processes are shown in Figure 1.7. For the dataset used in this analysis where both the b and $\overline{b}$ are required to be central[6], the dominant production mechanism is flavor creation.

[6] The term central here refers to particles boosted in the transverse direction relative to the colliding proton beams and reconstructed in the central part of the detector. See Section 2.2.

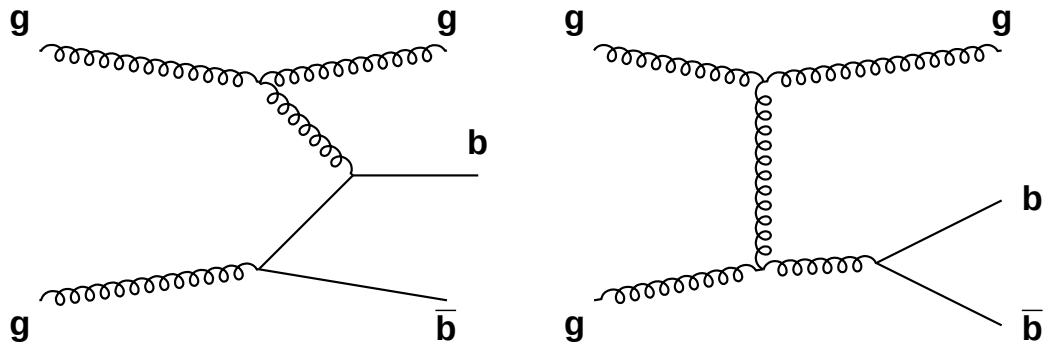

Figure 1.7: Feynman diagrams for two next-to-leading order $b\bar{b}$ production processes: flavor excitation (a) and gluon splitting(b).

Chapter 2

Experimental Apparatus

The data studied in this dissertation is produced at the Fermilab Tevatron accelerator and collected by the Run II Collider Detector at Fermilab (CDF-II). This chapter provides an overview of the accelerator and detector which have been more fully documented elsewhere. It also describes in some detail the major detector components and the trigger system essential to the analysis.

2.1 The Tevatron

The Tevatron at Fermilab is currently the world's highest energy particle physics collider. The Tevatron accelerator complex produces proton and antiproton beams which are collided at 1.96 TeV center of mass energy. The Tevatron is a circular synchrotron 2 km in diameter. It employs nearly 800 dipole and about 200 quadrapole superconducting magnets kept at a temperature of 4.3 K by large scale cryogenic cooling with liquid helium. The machine holds 36 bunches of protons(p) and antiprotons($\overline{p}$) spaced 396 ns apart. The radio-frequency(RF) buckets used to accelerate the particles define these bunches. Once the beams are injected and accelerated, collisions are allowed to occur at two points in the main ring, and the detectors CDF-II and D0 are located at these points. Figure 2.1 shows the various parts of the accelerator complex used for the production, storage and colliding of the beams.

2.1.1 Proton Production

The creation of a proton beam begins with hydrogen gas contained in the Cockcroft-Walton pre-accelerator. Electrical discharges ionize the gas creating H^- ions which are subsequently separated from other particle species by a magnetic field and accelerated to 750 keV by the diode-capacitor voltage multiplier. The separation and acceleration occurs every 66 ms to segment the beam into bunches which are injected into the linear accelerator(Linac). The 150 m long Linac further accelerates the beam bunches to 400 MeV and injects them into the Booster. At injection the ions are passed through a thin carbon foil which strips off the electron leaving a beam of bare protons. The Booster is a synchotron of about 150 m in diameter in which the protons are collected. After about 10-12 revolutions of the beam around the Booster the beam reaches maximum intensity; it is then accelerated to 8 GeV and sent to the Main Injector.

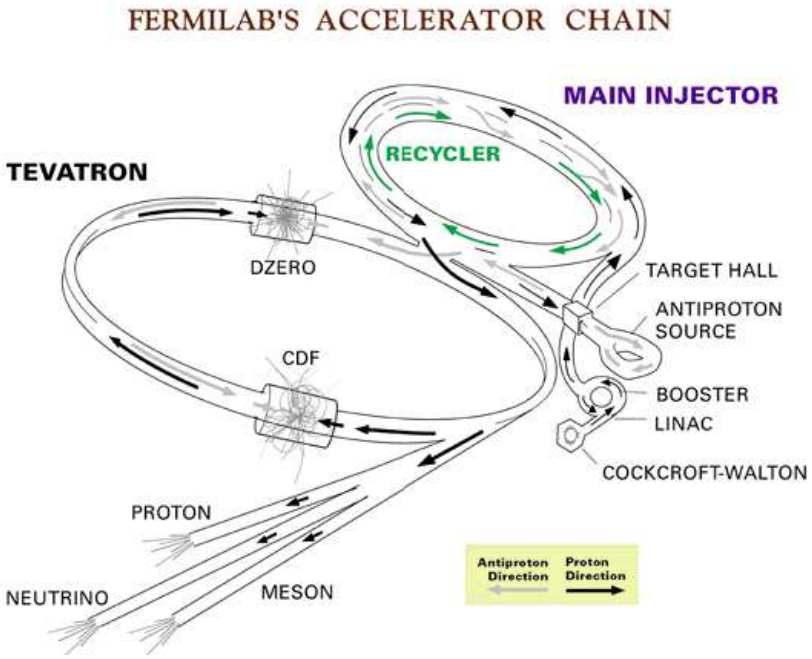

Figure 2.1: The accelerator complex at Fermilab as used for the collection, acceleration, and collision of protons and antiprotons.

2.1.2 Antiproton Accumulation

The Main Injector is a multi-purpose synchrotron exactly seven times the circumference of the Booster. It serves to

- accept 8 GeV protons from the Booster
- accelerate protons to 120 GeV for antiproton production
- accept 8 GeV antiprotons from the antiproton accumulator
- accelerate protons and antiprotons to 150 GeV for injection into the Tevatron.

The first two functions are performed during collider accumulation mode and the second two during collider injection mode. In accumulation mode the Main Injector receives a set of 84 proton bunches (about 5×10^{12} protons) from the Booster every 2 seconds. The protons are accelerated to 120 GeV and then directed toward the Target Hall where they are collided with nickel alloy target. The resulting shower of particles is focused into a parallel beam by a cylindrical lithium lens. This beam which has a similar bunch structure as the incident proton beam is passed through a pulsed dipole magnet. The magnetic field separates the negatively charged particles with about 8 GeV of kinetic energy. About 20 antiprotons are produced for every 10^6 protons on target, and these are collected in the Antiproton Source. In the Antiproton Source the antiprotons are de-bunched into a continuous beam adiabatically through RF manipulations and their range of momentum is reduced through stochastic cooling. The beams are also narrowed in

these processes which minimize any accompanying beam loss. The antiprotons are accumulated in the Antiproton Source until a sufficient stack has been acquired for collisions in the Tevatron, a process which takes around 10-20 hours.

Since 2004, an additional Recycler Ring located in the same tunnel as the Main Injector has provided additional storage of antiprotons. Limiting the stack size in the Antiproton Source allows an optimization of antiproton accumulation rate. This rate is the largest limiting factor in Tevatron running.

2.1.3 Collisions and Luminosity

In order to create collisions, antiproton accumulation is stopped and the Main Injector(MI) switches to collider injection mode. Seven sets of protons are received from the Booster, and accelerated to 150 GeV in the MI. They are coalesced into a single bunch before being injected into the Tevatron. The process is repeated every 12 seconds until 36 proton bunches of about 3 $\times 10^{11}$ p are loaded into the Tevatron. Twelve bunches each separated by 21 RF buckets (396 ns) are grouped together into three trains of bunches. The trains have a larger separation of 139 RF buckets, and these gaps provide the space needed to insert antiprotons without disturbing the protons and to safely the abort the beam. Antiprotons are extracted from the Antiproton source and the Recycler and are injected in sets of four coalesced bunches each of about 6 $\times 10^{10} \overline{p}$ until 36 bunches are circulating in the Tevatron. The antiproton bunch spacing is a mirror image of the proton spacing and circles the Tevatron in the opposite direction sharing the same magnet and vacuum systems. Electrostatic separators minimize beam interactions allowing each beam to be controlled independently in their helical orbits. The Tevatron RF system then accelerates both beams until they have an energy of 980 GeV. At this energy, a single particle circles the Tevatron in 21 μs at 0.9999996 c.

Once the beams are fully accelerated they can be brought into collisions by the focusing quadrapole magnets. The two collider detectors CDF and D0 are built around the collision points. Quadrapoles installed on either side of each detector reduce the spatial distribution of the beam to maximize the probability of $p\overline{p}$ interactions. The Tevatron collider performance is evaluated in terms of the instantaneous luminosity, $\mathcal{L}$, which is the coefficient between the rate of process and its cross-section, σ.

$$rate\ [\frac{events}{s}]\ =\ \mathcal{L}\ [\frac{1}{cm^2 s}] \times \sigma\ [cm^2] \tag{2.1}$$

The instantaneous luminosity for $p\overline{p}$ collisions can be approximated as

$$\mathcal{L}\ =\ \frac{f N_B N_p N_{\overline{p}}}{2\pi(\sigma_p^2 + \sigma_{\overline{p}}^2)} \times H(\frac{\sigma_\mu}{\beta^*}), \tag{2.2}$$

where f is the frequency of revolution, N_B is the number of bunches, $N_{p/\overline{p}}$ is the number of protons/antiprotons, and $\sigma_{p/\overline{p}}$ is the beam size for protons/antiprotons at the interaction point. There is a correction factor, H, which depends on the bunch shape and crossing angle of the beams. The instantaneous luminosity degrades exponentially over time as particles are lost due to beam-beam interactions and collisions. During ideal operation the beam will be intentionally

dumped after 15-20 hours of recording collisions and replaced with a new store of antiprotons which have been collected in the meantime. One the most important aspects of Run II has been the improvements in higher instantaneous and integrated luminosity through more efficient storing, cooling and, and transferring of antiprotons. Figure 2.2 shows the improvement of the Tevatron's peak luminosities during Run II.

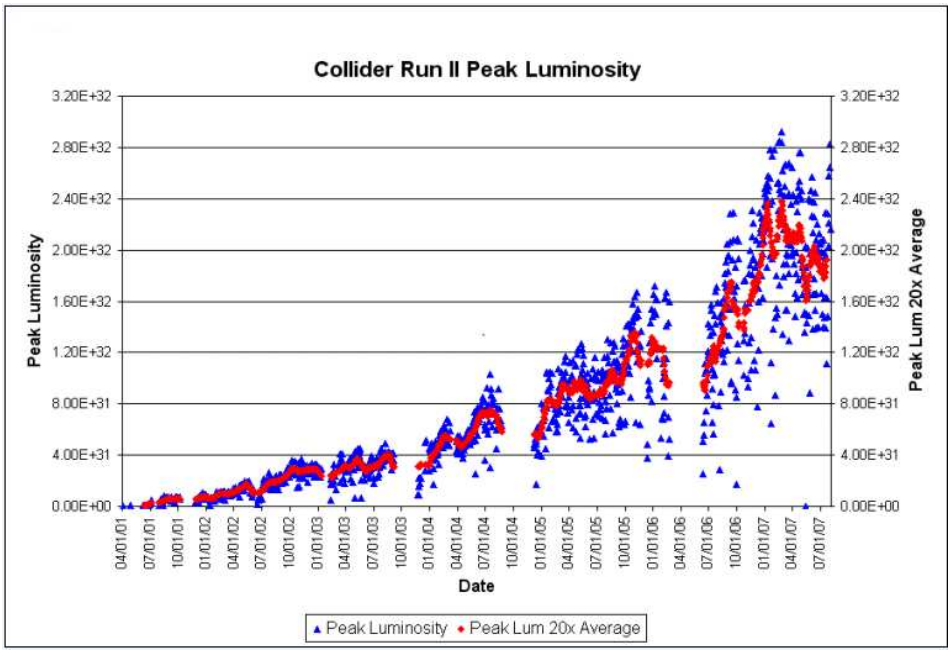

Figure 2.2: Tevatron peak instantaneous luminosity averaged between CDF and D0 from April 2001 to July 2007. Increases reflect the beam division upgrades in storage, cooling and transfer of antiprotons.

2.2 CDF Detector

The CDF Detector referred to throughout this thesis is in fact the CDF-II Detector and represents a substantial upgrade in many aspects over the CDF Detector used in Run I. A brief overview of the detector is given followed by a fuller description of the components relevant to this analysis. A detailed description of the entire detector and trigger can be found the Technical Design Reports of the CDF-II detector [37]. It was designed and built and it is operated and maintained by the CDF collaboration, a team of several hundred physicists and engineers representing more than 60 universities in more than a dozen countries. In June 2001, the first data was recorded with the CDF-II detector.

2.2.1 Detector Overview

In order to take advantage of the full scope of physics in a hadron collider environment, the CDF detector is not geared to any one particular physics measurement. As a multi-purpose detector it is optimized to extract the essential properties of all types of particles produced in $p\overline{p}$ collisions. As seen in the cross-section of the detector shown in Figure 2.3, the CDF detector consists of a collection of tracking systems enclosed in a solenoidal magnetic field, an electromagnetic (EM) calorimeter, a hadronic calorimeter, and a muon detection system that includes several drift chambers and steel shielding. Charged particle momentum and displacement can be determined from the tracking systems, but neutral particles pass through undetected. The energy of photons, however, can still be measured by the EM calorimeter which also measures electron energy. Hadron energy is measured in the hadronic calorimeter. The muons, which are minimally ionizing, will constitute the majority of particles detected in the outer drift chambers.

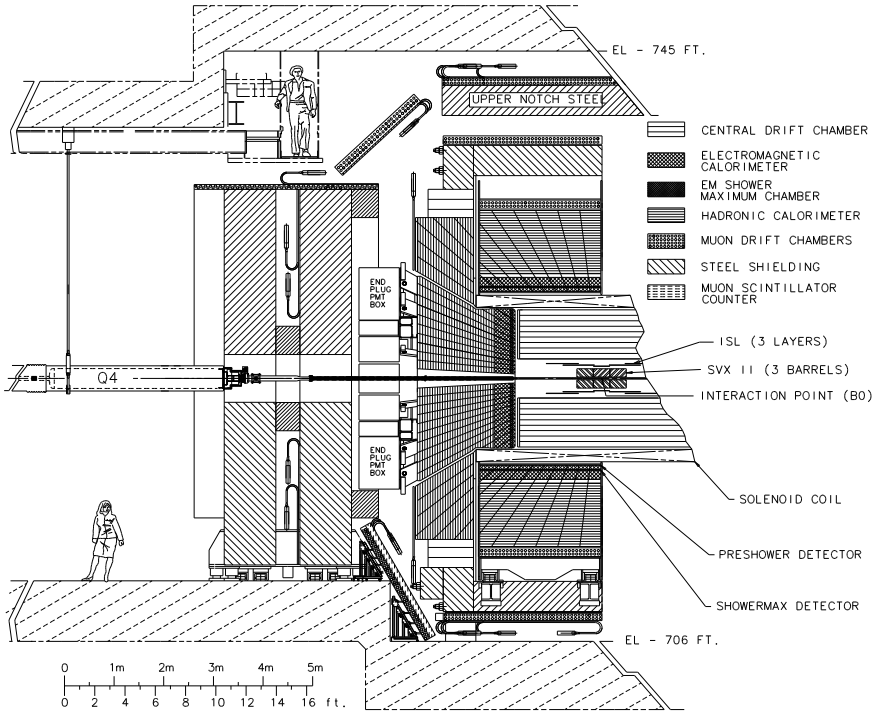

Figure 2.3: One half of the CDF-II detector from an elevation view. The various sub-detector systems are symmetric both azimuthally and forward-backward.

2.2.2 Coordinate System

CDF uses a coordinate system with the origin at the B0 beam interaction point. The z-axis is defined to be parallel to beamline pointing in the direction of proton circulation. The y-axis points vertically upward, and the x-axis radially outward from the Tevatron's center. The $x-y$ plane is referred to as the transverse plane. Since, the $p\overline{p}$ colliding beams are unpolarized, the observed

physics and thus the detector design are azimuthally symmetric. Therefore, it is convenient to use cylindrical geometry(r, ϕ, z) to describe the coordinate system. The plane defined by the radius, r, and the azimuthal angle, ϕ is also transverse. The term longitudinal is used to refer to the z-axis. Additionally, the polar angle θ from a polar coordinate system (r, ϕ, θ) is used to describe position relative to the origin along the beamline.

In $p\overline{p}$ collisions, not all of the center of mass energy is absorbed in the interaction. Any particular parton inside the proton carries a only a fraction of the proton's momentum, thus colliding partons in general have unequal longitudinal components of momenta. This effect results in the center of mass system being boosted along the longitudinal direction. Therefore, in such environments it is customary to use a longitudinal variable which is invariant under such boosts. This quantity, called the rapidity, is given by

$$Y = \frac{1}{2} \ln[\frac{E + p\cos(\theta)}{E - p\cos(\theta)}], \tag{2.3}$$

where E is the particle's energy and p is it's momentum. Rapidity transforms linearly, according to $Y' = Y + \tanh^{-1}\beta$ under a boost β so that Y is invariant. Practically, this expression is approximated by the pseudo-rapidity, η, which is the massless or ultra-relativistic limit of Y and requires only momentum information.

$$\eta = \frac{1}{2} \ln[\frac{p + p_z}{p - p_z}] = -\ln[\tan(\frac{\theta}{2})] \tag{2.4}$$

Given the azimuthal symmetry and rapidity invariance, the detector components are segmented in η and ϕ wherever possible allowing kinematic distributions to be more simply analyzed. The following sections describe the sub-detectors more explicitly, giving emphasis to the components used for this analysis.

2.2.3 Tracking Systems

Charged particles can be tracked in the detector by finding the ionized particles they create as they pass through the detector's material. By localizing the ionization in clusters of hits the particle's trajectory can be reconstructed electronically. Three-dimensional charged particle tracking is achieved through a system of three inner silicon detectors, a large outer drift chamber, and a superconducting solenoid. The 1.4 T magnetic field from the solenoid causes the charged particles to curve providing momentum information as they travel through the 1.4 meters of the tracking systems. Figure 2.4 displays the CDF tracking system layout for an $r - z$ cross-section. The tracking system is symmetric in ϕ.

Central Outer Tracker

The Central Outer Tracker (COT) [38] particlesis a cylindrical multi-wire open-cell drift chamber. It provides charged particle tracking in the region of $|z| < 155$ cm and of radii between 44 and 132 cm. The COT contains 96 sense wire layers which are arranged radially into eight super-layers. Each super-layer is divided into ϕ cells each of which has 12 sense wires. As the drift

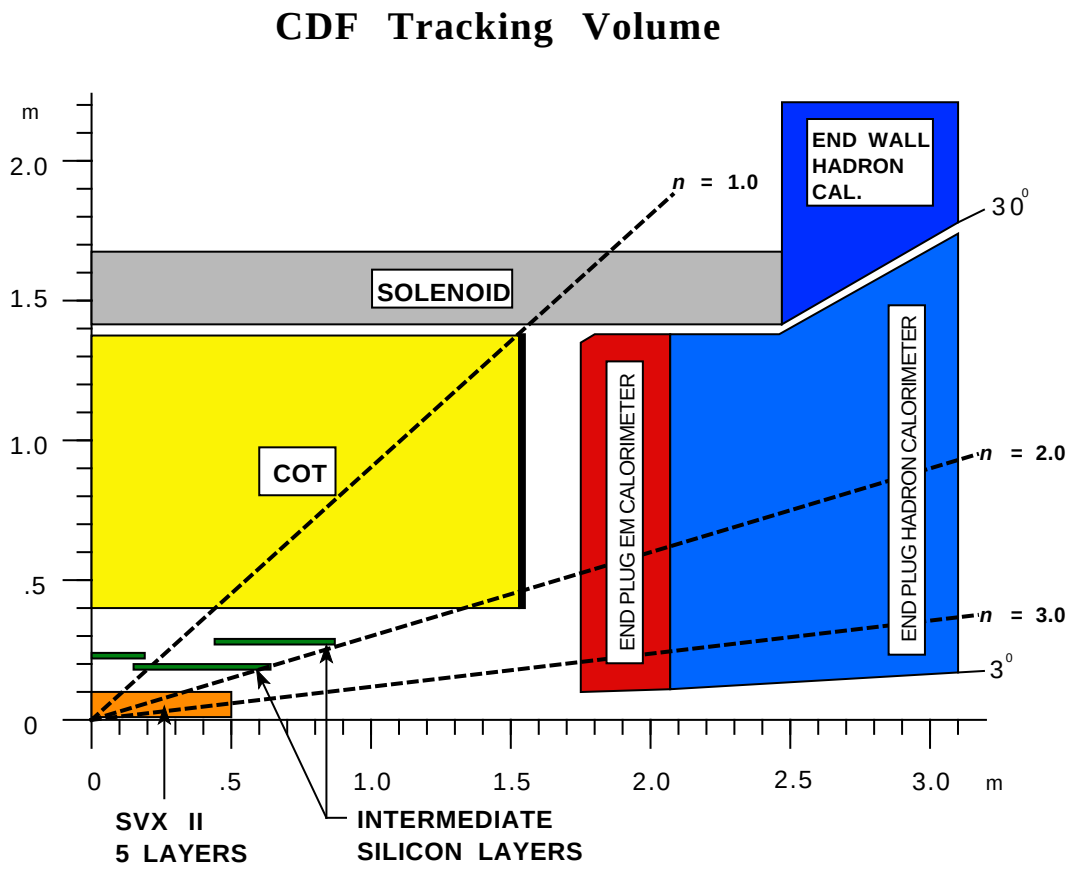

Figure 2.4: One quadrant of the CDF detector tracking layout which is enclosed by the solenoid and the forward calorimetry.

distance is approximately the same for all eight super-layers, the number of cells per super-layer increases from 168 up to 480 moving out radially. The entire COT contains 30,240 sense wires of 40 μm diameter and made of gold plated Tungsten. Four super-layers employ sense wires oriented parallel to the beam, for a measurement of hit coordinates in the $r-\phi$ plane. These are alternated radially with stereo super-layers whose wires are strung at a small stereo angle ($\pm 2°$) with respect to the beam. This layout provides an accurate measurement of transverse momentum, but less accurate information in the $r-z$ plane for the z-component of momentum. The super-layers also contain potential wires and are divided by cathode field panels creating an electric field throughout. Figure 2.5 shows the layout of the COT from an endplate.

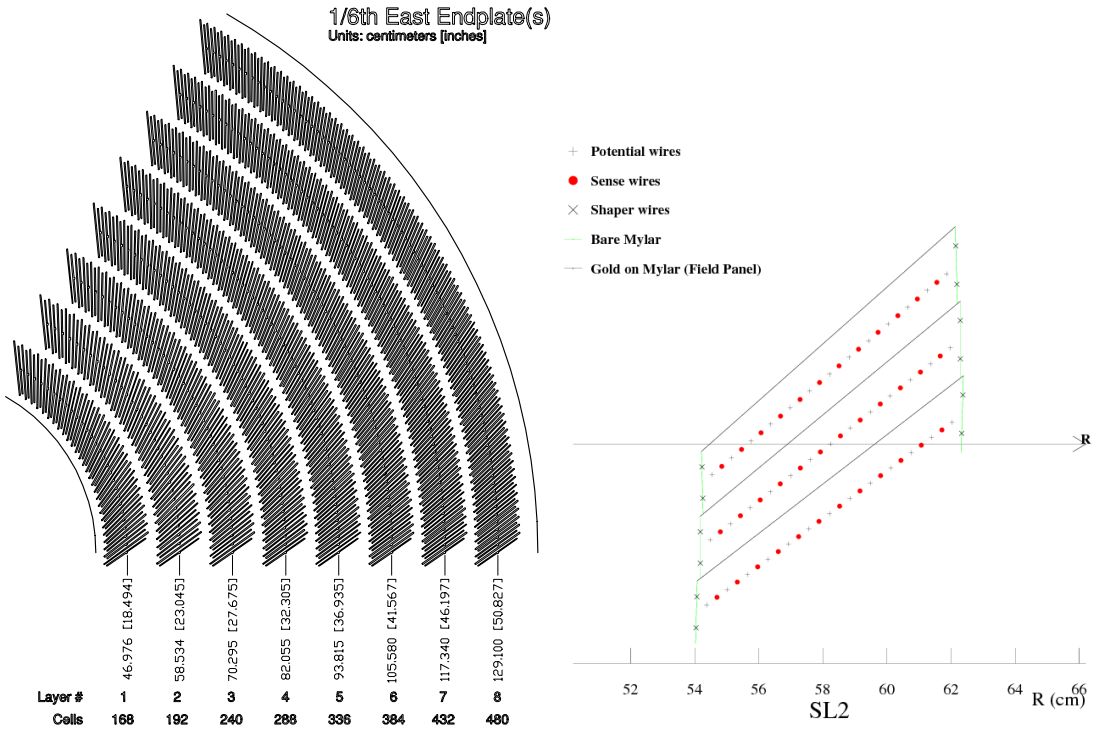

Figure 2.5: COT layout: 1/6 of an endplate(left), and wires in a supercell(right).

The COT is filled with a 50:50 Argon-Ethane gas mixture which functions as the active medium. Charged that travel through the chamber leave a trail of ionized electrons in the gas. Electrons drift toward the sense wires at a Lorentz angle of 35° being in both the chamber's electric field and the magnetic field which immerses the whole tracking volume. The supercells are tilted by 35° away from the radial so that the ionization electrons drift in the ϕ direction. The electric field very close to the sense wires is large, and when electrons get near a wire the acceleration causes further ionization resulting in a $\sim 10^4$ amplification. The $r-\phi$ position of the particle with respect to the sense wire is inferred from the arrival time of the electrical signal. The recorded position points are later processed by pattern recognition software reconstructing a helical track. The particle helices are described by the following parameters:

- C, curvature of the helix, inversely proportional to p_T
- d_0, impact parameter, distance to the beam from point of closest approach
- ϕ_0, azimuthal coordinate of the p_T vector from point of closest approach
- z_0, z coordinate of the p_T vector from point of closest approach
- $\cot\theta$, slope of helix step versus diameter.

Particles which have $|\eta| < 1$ pass through all eight COT super-layers.

Silicon Vertex Detector II

The accurate measurement of tracks close to the beamline is essential for many CDF physics analyses. In this work a precise determination of impact parameters is needed to identify B hadron decay products. Silicon micro-strip detectors which were pioneered for a hadron collider environment at CDF during Run I perform this function.

Silicon strip detectors are ideal for precision measurements close to the beam for two reasons. The silicon is able to sustain the high radiation doses characteristic of this region. In addition, the semi-conducting small band-gap silicon is ideal for providing fast electronic circuit readout and can be finely segmented for high precision measurements of position. A silicon tracking detector is composed of finely spaced silicon strips acting as reverse-biased $p-n$ junctions. The p-type (p^+) silicon strips are implanted on an n-type (n^-) silicon substrate with a distance of about 60 μm between them. On the opposite side n-type (n^+) silicon is deposited and may also be segmented. When a charged particle passes through the substrate it causes electron-hole pair ionization. Electrons drift toward the n^+ side and holes toward the p^+ strips. Charge deposition will be read out on one or more strips producing a localized signal. The p side strips provide hits giving $r-\phi$ position information, and the n side, if segmented, can provide z position information.

The Silicon VerteX detector II (SVX-II) [39] is built in three cylindrical barrels each 29 cm long. Each barrel is made of five concentric layers of double-sided silicon sensors and divided into twelve wedges called ladders. Table 2.1 shows the stereo angle, radial position and strip information for the SVX-II layers. Four silicon sensors are stacked longitudinally in each ladder and the readout electronics are mounted at both ends. The ladders have some azimuthal overlap at the edges for alignment purposes. The impact parameter resolution, essential to this analysis, is also considered a measure of SVX-II performance; it is about 35 μm.

Layer	$r-\phi$ strips	Stereo strips	Stereo angle	$r-\phi$ pitch	Stereo pitch	Active width
0	256	256	90°	60 μm	141 μm	15.3 mm
1	384	576	90°	62 μm	126 μm	23.8 mm
2	640	640	+1.2°	60 μm	60 μm	38.3 mm
3	768	512	90°	60 μm	141 μm	46.0 mm
4	896	896	-1.2°	65 μm	65 μm	58.2 mm

Table 2.1: Mechanical summary of the sensor layout for the SVX-II layers. Each layer has an active length of 72.4 mm

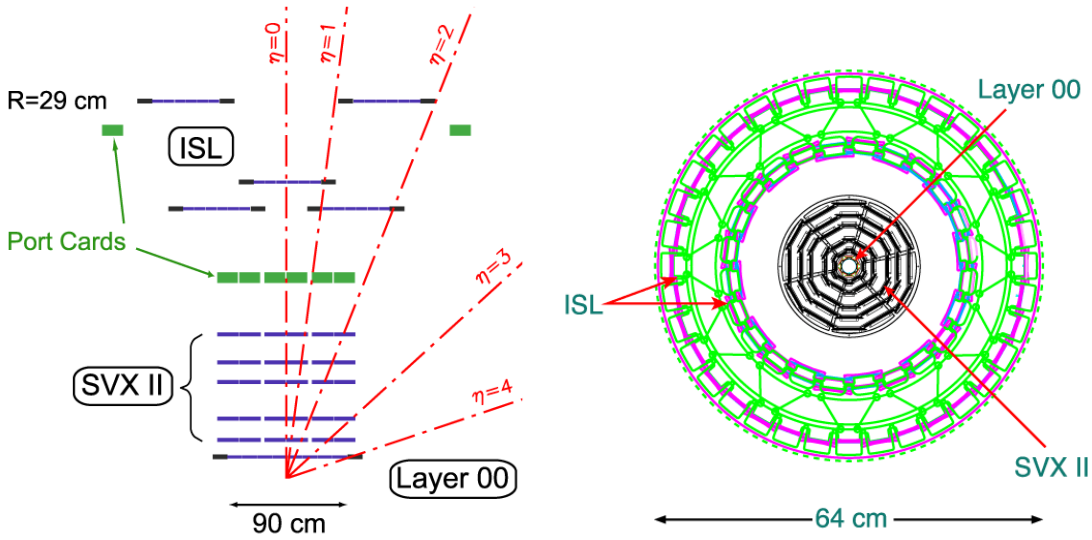

Figure 2.6: Layout of the silicon detectors: side-view of the detectors not drawn to scale (left), and end-view of the detectors centered around the beamline (right).

Layer 00 and Intermediate Silicon Layer

The innermost silicon detector, Layer 00 (L00) is made of single-sided silicon sensors placed directly on the beamline at a radius of 2 cm. It provides full azimuthal and $|z| < 47$ cm longitudinal coverage. Not all early CDF data has usable L00 hit information, but L00 has been correctly aligned and calibrated for use in much of the later data. It helps to recover the degradation in resolution due to multiple scattering from the cooling system and readout electronics of the central system. No L00 hits were used in the final track selection for this analysis.

The Intermediate Silicon Layer (ISL) is a double-sided silicon detector segmented into 12 wedges like the SVX-II. It consists of one central layer at a radius of 23 cm to provide an intermediate position measurement between the SVX-II and the Central outer tracker. Additionally, two layers at radii of 20 cm and 29 cm in the region of $1.0 \leq |\eta| \leq 2.0$ provide forward tracking information. The ISL strips have a 1.2° stereo angle.

Figure 2.6 shows the coverage of the silicon detector subsystems.

2.2.4 Muon Systems

Muons being over 200 times more massive than electrons undergo far less bremsstrahlung radiation. Unlike pions(π) and kaons(K) they are not subject to strong interactions with nuclei in matter. Therefore, a muon created in collisions with enough energy will pass through the calorimeter systems with minimal ionizing interactions. This property of muons is exploited in the CDF detector by placing the muon systems radially outside the calorimetry. Additional steel absorbers are also used to further reduce the chance of other particles reaching the muon

chambers.

Four systems of drift chambers and scintillation counters are used in the detection of muons and cover a range of $|\eta| < 1.5$ [40]:

- CMU - Central MUon detector
- CMP - Central Muon uPgrade
- CMX - Central Muon eXtension
- IMU - Intermediate MUon detector.

Figure 2.7 shows the coverage of the muon detectors and Table 2.2 summarizes their design parameters. The scintillation counters, CSP and CSX, help suppress backgrounds from out-of-time interactions for the CMP and CMX chambers respectively.

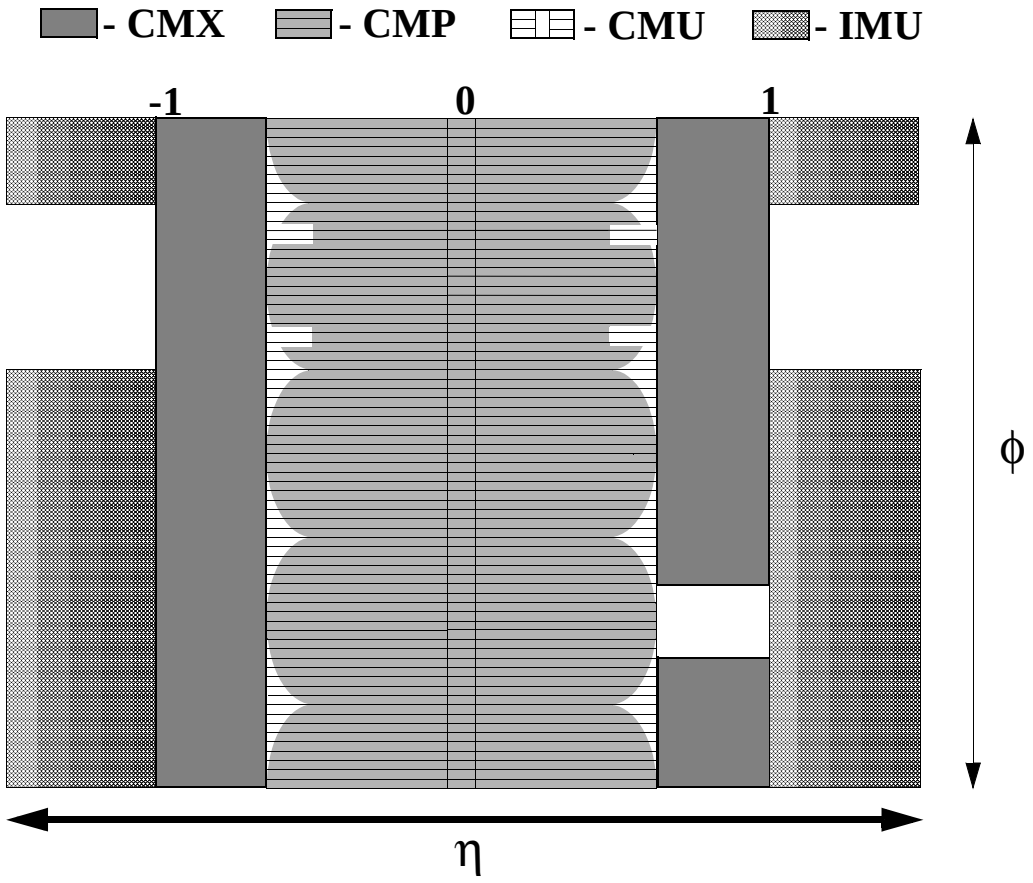

Figure 2.7: Muon detector coverage in η and ϕ for the CDF muon chambers.

The muon drift chambers like the COT employ sense wires parallel to the beamline and are filled with a 50:50 Argon-Ethane gas mixture. Muon candidates are identified as track segments

	CMU	CMP	CMX	IMU
Coverage in pseudo-rapidity	$\|\eta\| < 0.6$	$\|\eta\| < 0.6$	$0.6 < \|\eta\| < 1.0$	$1 < \|\eta\| < 1.5$
Number of drift tubes	2304	1076	2208	1728
Number of scintillation counters	-	269	324	864
Pion interaction length	5.5	7.8	6.2 - 10	6.2 - 20
Minimum μ p_T	1.4 GeV	2.2 GeV	1.4 - 2.0 GeV	1.4 - 3.0 GeV
Multiple scattering resolution	12 cm/p_T	15 cm/p_T	13 cm/p_T	13-25 cm/p_T

Table 2.2: Physics parameters for the various CDF muon systems.

in the chambers and are called muon stubs. A muon stub is matched with a track measured by the COT to reduce background from noise in the electronics and from hadrons which manage to reach the muon chambers.

While heavy material shielding reduces the number of hadrons faking muons in the detectors, it increases the effects of multiple Coulomb scattering. Coulomb scattering is the elastic scattering of a point-like particle (muon in this case) on a massive charge (nuclei of the material), and many small angle deflections may contribute before the muon reaches the detector. This effect complicates the track-stub matching, but the mismatch distribution is Gaussian and can be accounted for.

CMU

The Central MUon detector (CMU) is located right around the outside of the hadronic calorimetry at a radius of 347 cm from the beamline. The CMU is segmented into 24 wedges of 15° in ϕ, but only 12.6° of each wedge is active instrumentation leaving a 2.4° between each wedge and an azimuthal acceptance of 84 %. The CMU is also divided into an East(positive η) and West (negative η)halves with a coverage of $|\eta| < 0.6$. Each wedge is further segmented into three 4.2° modules each of four layers of four drift cells. The sense wires in the drift cells are made of stainless steel and kept at +2325 V. They are offset by 2 mm in alternating layers to improve hit resolution - about 250 μm in the $r - \phi$ plane and about 1 mm in z. The timing information from the drift cells is used to reconstruct a muon stub. Muons of $p_T > 1.4$ GeV can reach the CMU.

CMP

The Central Muon uPgrade (CMP) is a second set of muon drift chambers placed behind 60 cm of additional steel absorbers. This material provides an extra 2.3 pion interaction lengths to further limit the probability of hadronic punch-through to the CMP. The CMP chambers are single wire drift tubes which are rectangular in shape (2.5 cm × 15 cm). They are 640 cm long and configured in four layers with alternate half-cell staggering. The overall shape of the CMP is that of a rectangular box around the central detector. It is the only major detector component which is not azimuthally symmetric, and thus its coverage in $|\eta|$ varies as a function of ϕ as seen in Figure 2.7. Muons of $p_T > 2.2$ GeV can reach the CMP. The CMU and CMP have a large overlap in coverage and are often used together; the same scintillators are used for both detectors, CMP helps to cover to CMU ϕ gaps and the CMU covers the CMP η gaps. However,

the sample of muons which register a stub in both detectors is the least contaminated by fake muons and are referred to as CMUP muons. Only CMUP muons are used for this analysis.

2.2.5 Other Detector Components

This sections provides a brief overview of the remaining major detector components. These systems are at most indirectly involved in the data and analysis presented in this dissertation.

Calorimetry

The CDF calorimetry is composed of several systems of electromagnetic(EM) and hadronic scintillator sampling calorimeters which are segmented in a uniform pattern of projective towers. The tower geometry provides an even segmentation in ϕ and η pointing back to the interaction region. Each calorimetry subsystem is uniform in ϕ and all five subsystems combined provide coverage for EM objects and hadrons out to $|\eta| < 3.6$:

- Central Electromagnetic (CEM), $|\eta| < 1.1$
- Central Hadron (CHA), $|\eta| < 0.9$
- Wall Hadron (WHA), $0.7 < |\eta| < 1.3$
- Plug Electromagnetic (PEM), $1.1 < |\eta| < 3.6$
- Plug Hadron (WHA), $0.7 < |\eta| < 1.3$

The calorimetry has a segmentation of 0.1 in η and 15° in ϕ, except for the plug calorimeter between $1.1 < |\eta| < 2.1$ where the ϕ wedges are 7.5°. The calorimeters use an active medium of polystyrene based scintillators which are alternated with absorber material. CEM and PEM use lead sheets for absorber material, while the CHA and WHA use steel and the PHA uses iron. As a particle traverses a layer of absorber material and interacts with the nuclei, it's energy is reduced and it produces a particle shower as it is stopped. The active medium is used to determine the energy of a shower. The total energy deposited in the scintillator at all layers determines the energy of the incident particle. The EM calorimetry interacts with electrons via Bremsstrahlung radiation and photons through conversions until there is not enough energy for more of these interactions. Hadronic showers are produced by hadrons interacting with nuclei via the strong interaction. Shower maximum detectors are embedded in the EM detectors at about 6 radiation lengths to help differentiate between electrons and photons.

Time of Flight

The Time of Flight detector (TOF) [42] is a cylindrical array of 216 scintillating bars each about 300 cm in length and with a 4 cm × 4 cm cross section. It is located just between the COT and the Solenoid at a radius of about 140 cm. The TOF system is designed to help identify low momentum charged hadrons by measuring the arrival time of the particle with respect to the bunch crossing time. This time is dependent on the particle's mass and especially helps to differentiate pions and kaons.

Cherenkov Luminosity Counters

The Cherenkov Luminosity Counters (CLC) [41] are used to measure the instantaneous luminosity ($\mathcal{L}$) of collisions at CDF. The luminosity can be inferred from the equation

$$\mu \times f_{BC} = \sigma_{p\overline{p}} \times \mathcal{L} \tag{2.5}$$

where the Tevatron bunch crossing frequency (f_{BC}) is known from the RF system, the inelastic $p\overline{p}$ cross section ($\sigma_{p\overline{p}}$) is know to about 4% uncertainty, and the average number of interations per bunch crossing (μ) is measured by the CLC. The CLC is composed of two assemblies of 48 conical isobutane filled Cherenkov counters. They are placed in the forward and backward regions at $3.7 < |\eta| < 4.7$. Excellent timing resolution allows the CLC to differentiate between beam losses which are typically out of time and particles from $p\overline{p}$ interactions. The CLC can measure the luminosity with a total uncertainty of less than 6%.

2.3 CDF Trigger System

In order to acquire useful data from the CDF detector a trigger system is necessary due to the overwhelming background of inelastic $p\overline{p}$ inherent in a hadron collider environment. The nominal crossing rate is 1.7 MHz though this is averaged over the beam abort gaps. The instantaneous rate during for bunch trains is 2.5 MHz, and at luminosities of $\sim 10^{32} s^{-1} cm^{-1}$ there are about 2 interactions per crossing. Storing detector readout from every crossing (about 200 kbytes) would require the ability to record about 500 Gbytes/s. This rate is not only unattainable with current technology, it would also result in an unwieldy and largely uninteresting dataset. The CDF trigger system addresses these issues by using partial detector readout to examine every event and applying physics algorithms to select events determined to be the most interesting.

At the beginning of Run II, CDF had the capacity to write out events at a rate of approximately 75 Hz. This capacity has increased to a rate of 150 Hz at the time of writing; however, this still requires the elimination of 99.994% of collision events. The reduction is accomplished by the trigger in three-levels, narrowing the selection with additional information at each level. The general goal is to accept as many interesting events as possible while keeping the deadtime at 5% or less. The deadtime is a measure of inability to readout interesting events because all the available slots for events passing to the next level are full.

At the first level of the trigger only rough algorithms are used, and not all the detector components (particularly the Silicon sub-detectors) are read out. The front end electronics have a pipeline of 42 clock cycles (132 ns) during which the first level decision must be made. The rate of events passed to the second level is around 25 kHz. Events not selected are ignored and drop out of the pipeline. The next level incorporates additional information including readout from the Silicon detectors and reduces the rate to 900 Hz. Level 1 and 2 triggering mechanisms are hardware based and use custom electronics. Level 3 is a software based trigger algorithm implemented on a farm of about 500 computers. It has almost all the information available in the offline reconstruction. Figure 2.8 shows the data flow of the CDF trigger system.

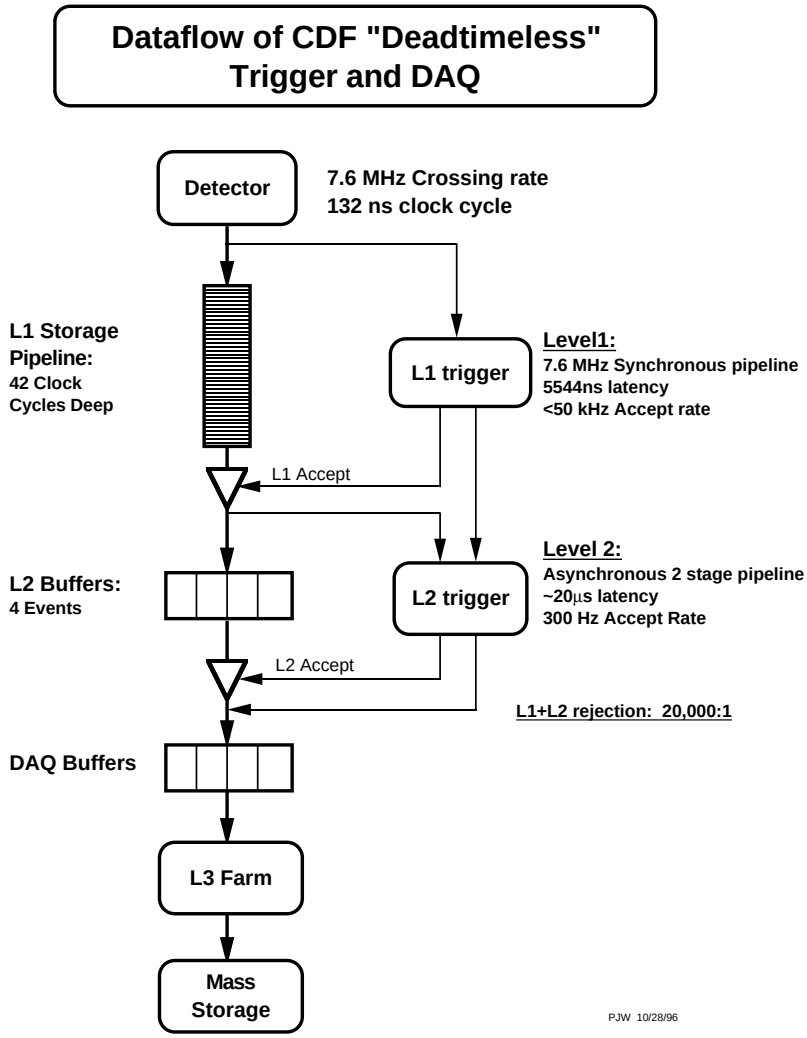

Figure 2.8: Digram of the data acquisition system for the CDF-II trigger.

Each subset of data is classified according to its specific trigger paths. Several higher level triggers may use a common Level 1 trigger with tighter constraints on different measurable quantities. The trigger path is defined by the trigger requirements met at all three levels, and confirming the trigger path offline is important to many analyses. Confirmation eliminates the contribution of volunteer events, events which may met the requirements for the higher level trigger of interest but have not passed the associated Level 1 trigger. This analysis confirms the trigger selection for every event in the offline analysis.

2.3.1 Level 1

The Level 1 trigger (L1) is a synchronous system of custom electronic hardware designed to analyze every event and produce an accept or reject decision. This must be done on the order of

5 μs, before the buffers storing the data must be cleared, and at a rate of 25 MHz. L1 decisions are made based on partial information from the COT (only the 4 axial superlayers are used for two-dimensional tracks), the calorimeters (total energy and some single tower information), and muon systems (stubs in the CMU, CMP, and CMX). The eXtremely Fast Tracker (XFT) performs a rough track reconstruction and passes the tracks to the extrapolation unit (XTRP). The XTRP processes the tracks and feeds the three L1 subprocess: L1 CAL, L1 TRACK, and L1 MUON. L1 MUON and L1 CAL also incorporate the information available from the calorimetry and muon systems respectively to trigger on muon, electron, and photon objects, on jets, and on total transverse energy or missing transverse energy. The L1 TRACK triggers events based only on tracking algorithms. All three subprocesses report decisions to the Global Level 1 system which accepts or rejects each event. Accepted events are buffered for Level 2 analysis.

XFT

The XFT [44] processes tracks from the axial superlayers of the COT, only in the $r-\phi$ plane, in time for each L1 decision. It reports the p_T and a good approximation of the track's ϕ position from the angle of the p_T in superlayer 6. The pattern recognition is based on pre-defined patterns of COT hits coming from the beamline. The XFT is capable of reconstructing tracks with $p_T >$ 1.5 GeV with an efficiency of around 95% and a fake rate of only a few percent. The angular segmentation is 1.25°, but the XFT achieves a resolution of ~ 5 mrad. The momentum resolution is $\sigma_{p_T}/p_T = 0.016 p_T$. The XFT reports all reconstructed tracks to the extrapolation unit to be processed for L1 triggers. Recently, a confirmation bit from Stereo superlayers was added to L1 XFT processing. This addition has made it possible to reduce the number of fake XFT tracks which had sharply risen with luminosity increases.

XTRP and L1 TRACK

The extrapolation unit (XTRP) [43] receives reconstructed track information from each of the parallel XFT processors. Based on the azimuthal position and transverse momentum of a track and accounting for multiple scattering the XTRP then roughly identifies the areas in the muon detectors and calorimetry which should be checked for hits. Matching hits would confirm a L1 muon or electron. This extrapolation information is passed to the L1 CAL and L1 MUON subprocesses.

Some XTRP tracks are also passed across the backplane of the electronics crate to the L1 TRACK processor which is also located in the crate. The L1 TRACK can accept two tracks per 15° ϕ wedge of the XFT. It also only accepts tracks with $p_T > 2.0$ GeV and a maximum of 9 tracks per event. Various L1 track-only triggers are formed with two-track topologies corresponding to primarily heavy flavor physics processes. The L1 track board firmware examines all combinations of two tracks for every trigger in each event. Chapter 3 describes the hardware upgrade project completed to the L1 track board as a part of this thesis research at CDF.

2.3.2 Level 2

A diagram of the decision process from the detector through Level 2 is shown in Figure 2.9. Level 2 is an asynchronous combination of hardware and software triggers which processes events in the order they are accepted by Level 1. Level 2 also incorporates additional information from the shower max drift chambers in the central EM calorimeter(CES) and the axial hits from the SVX-II detector. This additional information is combined with the Level 1 information to produce Level 2 objects. There are several areas in which decisions are improved at Level 2 to reduce the 25 kHz Level 1 rate to 900 Hz. Information from the CES drastically reduces the electron rate by removing fake electrons. Better ϕ and p_T resolution from the SVX allow tighter matching and high p_T thresholds for many muon, electron, and jet triggers. A precise measurement of the track impact parameter, d_0, greatly enhances the ability of track triggers to identify heavy flavor.

Silicon Vertex Trigger

The Silicon Vertex Trigger (SVT) [45] is one of CDF's most powerful tools. It is especially effective at identifying heavy flavor hadronic decays which would otherwise be nearly impossible due to the inelastic background. The SVT combines the data from the XTRP and the SVX detector to identify displaced tracks indicative of B hadron decays. The impact parameter resolution of the SVT is about 35 μm, similar to the resolution available offline. This displacement resolution allows identification of tracks whose origination point is inconsistent with the primary interaction region.

A typical event is processed by Level 2 in about 20-30 μs. In order for the SVT to readout the SVX detector information and process it in that time, the intrinsic wedge structure of the SVX and XTRP is exploited. Each of the 15° wedges is processed in parallel with the XTRP track information being extrapolated inward to SVX detector. In order to achieve the necessary resolution the SVT requires hits in all four axial SVX layers associated with the XTRP seed track.

2.3.3 Level 3

The final level of the CDF trigger involves the reduction of rate from about 600-900 Hz down to about 100-150 Hz. The criteria for Level 3 triggers are similar to their Level 2 counterparts but involve the full event reconstruction. The output for each event passing the Level 2 trigger is readout via optical fibers from all the sub detectors and sent to one of about 500 commercial computers running LINUX. This PC farm contains the Level 3 trigger software. An event which is accepted at Level 3 is then written to mass storage.

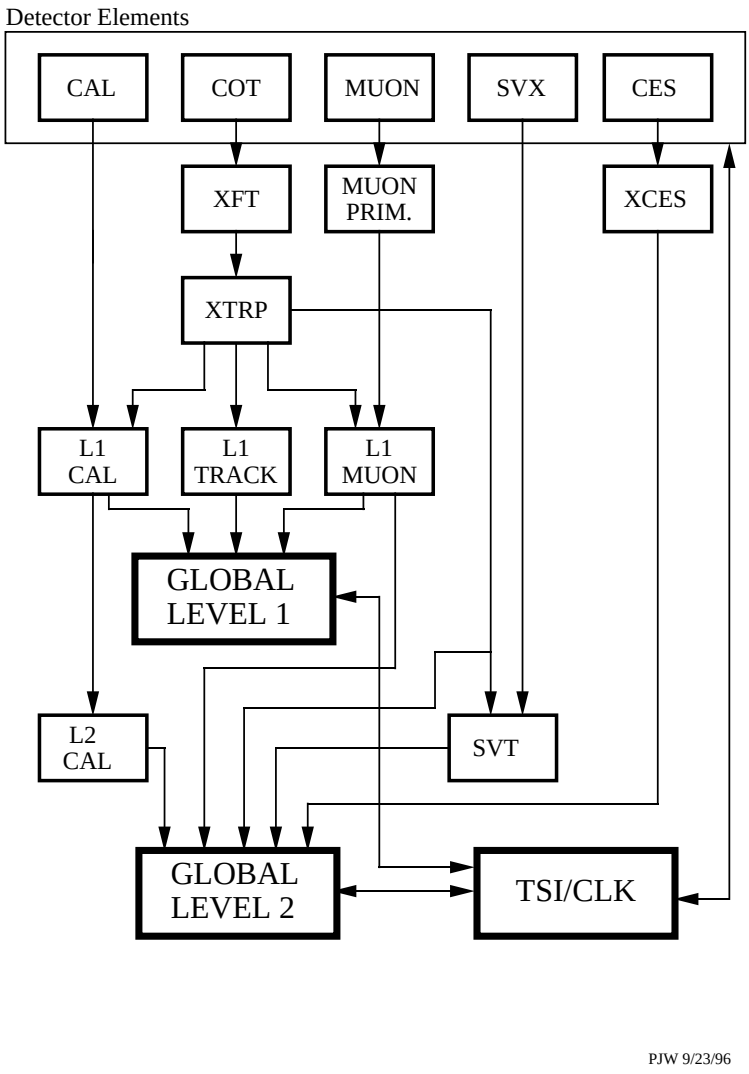

Figure 2.9: Various trigger paths for output from the major detector components in the CDF Level 1 and Level 2 trigger systems.

Chapter 3

Track Trigger Upgrade

This chapter provides a technical description of an upgrade to the CDF trigger system. The track-only based trigger selection is enhanced by the replacement of the dedicated track trigger circuit board. The track trigger provides important data particularly from hadronic decays of heavy flavored mesons contributing, for example, to the observation of B_s oscillations [20], the discovery of new B baryon states [47], and the observation of new B_s decay modes [48]. The following information is not essential to the CP asymmetry result, but it is included for completeness, and is intended primarily for trigger experts.

3.1 Motivation

The track trigger upgrade was designed to incorporate additional information at Level 1(L1) for track-only trigger decisions. Additionally, the new trigger board was designed to accept up to nine eligible tracks per event rather than the previous maximum of six tracks. These changes were significant because the L1 track triggers become the basis for SVT triggers at Level 2, and these triggers are essential to hadronic B analysis including B_s mixing. Also, the increased maximum number of tracks addressed the concern that as the luminosity increased over the course of Run II the events with 7 or more tracks would increase to a point were the two triggers would cause unacceptable deadtime in the trigger.

3.2 XTRP

The XTRP Data Boards operate synchronously as part of the Level 1 trigger system [37, 43]. Each Data Board accepts COT tracks from two XFT linkers [44] and extrapolates the tracks to the muon, time-of-flight and calorimetry systems. Additionally, the Level 1 Track Trigger board within the XTRP generates trigger decisions based upon XFT tracks. The Track Trigger passes the trigger decisions directly to Level 1 trigger decision crate. The track trigger upgrade project was intended to reduce the rate of automatic Level 1 track triggers and to increase the information available for track triggers.

3.3 Run 2A Two Track Trigger

The XTRP system receives XFT tracks for each bunch crossing. Each XTRP Data Board receives information from two adjacent XFT linkers (with one linker per 15° wedge). The Data Boards perform calorimetry and muon extrapolation, in addition to passing a subset of XFT tracks across the VME backplane to the Two Track Board. For a track to be passed to the Two Track Board, it must pass a predefined threshold (typically 2.04 GeV) and be a four-layer XFT track.

The Two Track Board can receive at most two tracks from a single 15° wedge. If more than two tracks are eligible, then the two "outer" tracks ($\phi_{\min}$ and $\phi_{\max}$) are sent to the Two Track Board. This selection occurs regardless of track momentum. An example of this is shown in Figure 3.1.

The Two Track Board has onboard logic to evaluate up to 6 tracks. If more than 6 tracks are eligible for consideration, then the Two Track board generates an "auto-accept" for all triggers. This indicates that the event should be accepted, and also indicates that the Two Track Board did not evaluate all possible track combinations. This trigger is referred to as the "L1_SEVEN" trigger, indicating that there were at least seven tracks eligible to be evaluated by the Two Track Board. The L1_SEVEN trigger table p_T option sets the predefined threshold for tracks eligible to be passed to the Track Trigger Board. In the case where there are three tracks in one wedge, only two of those tracks count toward the total, since only two tracks are sent to the Two Track Board.

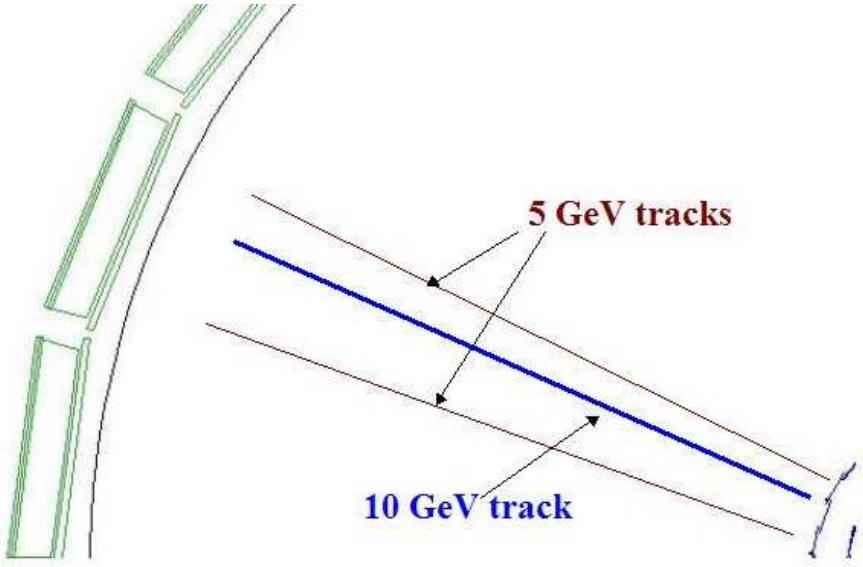

Figure 3.1: An example of the "two tracks per wedge" limitation in going from the XTRP Databoards to the Two/Three Track board. In this case, there are three XFT tracks in a single 15° wedge. Although the middle track of the three has higher p_T, only the outer two tracks (the two 5 GeV tracks) are sent to the track trigger board. Only four-layer XFT tracks above 2 GeV are used in this algorithm.

The tracking information available in the Two Track Board is

- XFT p_T (7-bits)
- short track bit (1-bit) unused
- "global ϕ" (9 bits).

The transverse momentum information is identical to binning provided by the XFT. Although the Two Track Board is able to handle tracks with hits in only 3 of the 4 COT axial superlayers, operationally this was never utilized. The azimuthal information utilized in the Two Track Board is the XFT ϕ_{SL6} which is the azimuthal angle of the track at COT superlayer 6 as measured by the XFT. In the Two Track Board, the ϕ granularity is 1.25°.

The Two Track Trigger Board performs trigger lookups for each possible track pair. The lookups for p_T and ϕ are performed separately, so it is not possible to implement algorithms based upon $p_T/\delta\phi$ correlations.

The Two Track Trigger outputs 16 distinct trigger bits. One bit is predefined as the auto-accept bit, leaving 15 other programmable one or two-track triggers.

The Two Track Trigger Board (2TT) was used as the L1 tracking trigger from the beginning of Run II until December 2004 when the Track Trigger Upgrade had been fully commissioned for physics data and was installed for operation.

3.4 Three Track Trigger Board

The Three Track Trigger Board (3TT) was originally motivated as a device that would retain the two track functionality but allow triggers involving track triplets. The Three Track Board also allows for more track combinations, so up to 9 tracks can be evaluated within a single event. Events with more than 9 tracks are auto-accepted on what is referred to as the "L1_TEN" trigger. The ability to handle events with higher track multiplicity was motivated by the anticipated increase in instantaneous luminosity from the Tevatron.

After the initial testing of the prototype 3TT board, a test with data from $p\overline{p}$ collisions was attempted at low luminosity. In analyzing the beam test data a logic flaw was discovered which was preventing the upgrade from replicating the 2TT. In analyzing potential solutions we determined that the two track functionality could be replicated only by abandoning the track triplet triggers or undertaking a massive rewiring of the boards. Additionally, we determined that by implementing a two-track board design the additional processing power could be used to make triggers with transverse mass capabilities. The availability of transverse mass information at L1 was deemed more important than triggering on three-track combinations. The decision was made to modify the prototype board to be an enhanced two track trigger board.

The basic operation of the Three Track Board is identical to the Two Track Board. It accepts XFT tracks from the XTRP Data Boards and generates up to 16 Level 1 track trigger decisions.

The primary differences between the 2TT and 3TT are summarized in Table 3.1. As mentioned above, the number of tracks which fire the auto-accept has increased. In addition, the binning of p_T and $\delta\phi$ information has changed.

	2TT	3TT_v0	3TT_v1
auto-accept(# tracks)	> 6	> 9	> 9
p_T bins	96	62	62
$\delta\phi$	$\delta\phi_{\rm SL6}$	$\delta\phi_{\rm SL6}$	$\delta\phi_0$
$\delta\phi$ bins	288	63	63
transverse mass	no	no	yes

Table 3.1: Differences between the Two Track Board (2TT), the Three Track Board run in two track emulation mode (3TT_v0) and the Three Track board run in transverse mass mode (3TT_v1). These differences are described in detail in the text.

Following the necessary board and firmware modifications the new Three Track Board was retested. After several successful runs with collisions produced usable data, the 3TT was commissioned in December of 2004. The Three Track Board has been run in two different configurations. From the completion of its commissioning in December 2004 through May 2005, the Three Track board was run in a "two track emulation" mode, where all of the existing single and two-track triggers were replicated in the Three Track board. The only difference in operation is the auto-accept threshold. Note that all of the two-track p_T and $\delta\phi_{\rm SL6}$ cuts are along bin boundaries, so the p_T and $\delta\phi$ binning differences did not modify any of the two track trigger cuts. We refer to this period of running as 3TT_v0. Once the additional firmware modifications had been tested and implemented, transverse mass capability became available in the 3TT. This period of running is referred to as 3TT_v1, and it spans physics runs from June 2005 through current running.

3.4.1 Three Track p_T Mapping

In order to perform trigger decisions on as many as 36 track combinations, it is necessary to compress the p_T and ϕ binning. In the 3TT, we take the 7-bit XFT p_T information and compress it to 6 bits. This compression is performed by dropping the p_T bins for $p_T < 2\,\text{GeV}$ and compressing the high p_T bins into a single $p_T > 10\,\text{GeV}$ bin. This allows us to retain the existing XFT p_T granularity in 2-9 GeV range, where it is most important. This mapping is shown in Table 3.2.

The Three Track p_T binning described here is used in both 3TT_v0 and 3TT_v1 running.

3.4.2 Three Track ϕ Mapping

The track ϕ information passed from the XTRP Databoards to the Three Track Board has the same 9-bit resolution (1.25°) that was utilized in the Two Track Board.

In the Three Track Board, for each track pair, we calculate a $\delta\phi = \phi_2 - \phi_1$. We insure that $0° < \delta\phi < 180°$. We then drop the least significant $\delta\phi$ bit. This changes the $\delta\phi$ granularity from 1.25° to 2.5°.

Since all existing two-track triggers fall on 2.5° boundaries, this change had no affect on existing triggers. All opening angles greater than 155° are mapped into the 155° bin. This is acceptable because all two-track triggers either have no opening angle cut or else they require an

p_T bin	XFT p_T	3TT p_T
0	-1.52	0
1	-1.57	0
2	-1.63	0
3	-1.68	0
4	-1.75	0
5	-1.81	0
6	-1.88	0
7	-1.96	0
8	-2.04	-2.04
9	-2.13	-2.13
10	-2.23	-2.23
11	-2.34	-2.34
12	-2.46	-2.46
13	-2.59	-2.59
14	-2.74	-2.74
15	-2.91	-2.91
16	-3.05	-3.05
17	-3.15	-3.15
18	-3.25	-3.25
19	-3.37	-3.37
20	-3.49	-3.49
21	-3.62	-3.62
22	-3.76	-3.76
23	-3.92	-3.92

p_T bin	XFT p_T	3TT p_T
24	-4.09	-4.09
25	-4.27	-4.27
26	-4.47	-4.47
27	-4.68	-4.68
28	-4.92	-4.92
29	-5.19	-5.19
30	-5.49	-5.49
31	-5.82	-5.82
32	-6.19	-6.19
33	-6.62	-6.62
34	-7.11	-7.11
35	-7.68	-7.68
36	-8.35	-8.35
37	-9.14	-9.14
38	-10.11	-10.11
39	-11.29	-10.11
40	-12.80	-10.11
41	-14.77	-10.11
42	-17.45	-10.11
43	-21.33	-10.11
44	-27.43	-10.11
45	-38.40	-10.11
46	-64.00	-10.11
47	-99999	-10.11

Table 3.2: p_T mapping from XFT to the Three Track Board. The table shows the p_T values for XFT p_T bins 0-47, which correspond to negatively charged tracks. Positively charged tracks are quantified in bins 48-95, with 48 being high p_T and 95 being the lowest p_T (*i.e.*The 0-47 p_T ordering is flipped for 48-95.) [46] The Two Track Board used the p_T binning provided by the XFT with no translation.

XFT p_T bin range	ϕ bin correction
$0-3$	$+6$
$4-8$	$+5$
$9-12$	$+4$
$13-19$	$+3$
$20-28$	$+2$
$29-38$	$+1$
$39-56$	0
$57-66$	-1
$67-75$	-2
$76-82$	-3
$83-86$	-4
$87-91$	-5
$92-95$	-6

Table 3.3: Correction in going from $\phi_{\rm SL6}$ to ϕ_0. For each range of XFT p_T bins, we correct for track curvature in going from $\phi_{\rm SL6}$ provided by the XFT to ϕ_0 used in the trigger lookups for 3TT_v1. The bin correction listed here is using the 9-bit ϕ resolution ($= 1.25°$).

opening angle less than 135°.

$\delta\phi$ in 3TT_v0

In two-track emulation phase of the 3TT, the $\delta\phi$ values utilized were all based upon XFT $\phi_{\rm SL6}$.

$\delta\phi$ in 3TT_v1

To utilize $\delta\phi$ information to calculate transverse mass, we need $\delta\phi_0$. In the 3TT_v1 implementation, all $\delta\phi$ values used for two-track triggers are $\delta\phi_0$.

The $\delta\phi_0$ calculation is performed on the tracks before the p_T and ϕ compression. As it comes onto the Three Track Board, a ϕ_0 for each track is calculated based upon $\phi_{\rm SL6}$ and p_T. The translation used is summarized in Table 3.3. Once we have ϕ_0 for each track, we then calculate $\delta\phi_0$ for each track pair, and then drop the least significant $\delta\phi_0$ bit.

Therefore, in 3TT_v1, the $\delta\phi_0$ granularity is in 2.5° steps. We again use the $\delta\phi_0 = 155°$ bin to signify $155° < \delta\phi_0 < 180°$.

Tracks originating from adjacent XFT linkers ($\delta\phi_{\rm SL6} = 1.25°$ ignoring mini-ϕ) are assigned a dedicated $\delta\phi_0({\rm bin}) = 63$, which is then used to veto the track-pair. This implements the "adjacent linker cut" in the Three Track Board that vetoes trigger pairs from adjacent XFT linkers. Note that this implementation does not affect tracks from non-adjacent linkers that have small values of $\delta\phi_0$. This implementation was specifically chosen to preserve the ability to have an efficient $\phi \to K^+K^-$ trigger.

3.5 Transverse Mass

With $\delta\phi_0$ available in the same lookup RAM as the p_T of the two tracks, we are now able to implement a transverse mass trigger at Level 1. The transverse mass formula used assumes the

tracks are massless:

$$m_T = \sqrt{2p_T(1)p_T(2)[1-\cos(\delta\phi_0)]},$$

where $p_T(1)$ and $p_T(2)$ are the p_T values of the two tracks.

With the p_T and $\delta\phi_0$ binning used in the Three Track Board, the calculated transverse mass has the following limits:

- $m_T(\text{min}) = 0\,\text{GeV}$ when $\delta\phi_0 = 0$ (which means $\delta\phi_0 < 2.5°$)
- $m_T(\text{max}) = 19.7\,\text{GeV}$ when $\delta\phi_0 = 155°$ and $p_T(1) = p_T(2) = 10.11\,\text{GeV}$.

Obviously the high end has very poor resolution, but it is not the region of interest for m_T triggers. This trigger is designed for $B \to h^+h^{-\prime}$ ($m_T \sim 5\,\text{GeV}$) and $\phi \to K^+K^-$ ($m_T \sim 1\,\text{GeV}$).

3.6 Summary

The Track Trigger Upgrade has been a valuable contribution to the increased trigger capabilities of Run IIb. It has increased not only the multiplicity of tracks which can be handled by the CDF two track triggers, but has made available transverse mass information previously unavailable at the lowest level triggers.

Chapter 4

Analysis Strategy and Data Selection

4.1 Introduction

To date, CP violation in the B system has only been observed in fully reconstructed modes at the e^+e^- B factories. Although the fully reconstructed final states are quite clean, they suffer from low yields due to branching ratios and detector acceptance. A complementary technique for searching for CP violation at the Tevatron is to perform an inclusive analysis. This inclusive technique has the benefit of high statistical precision thanks to large semileptonic B branching ratios. In addition, the sample is integrated over all weakly decaying B species produced at the Tevatron. The challenge in this technique is that any CP violating effects are diluted by large contributions from known CP conserving processes.

Our goal is to measure the CP asymmetry:

$$A_{CP} = \frac{N(\mu^+\mu^+) - N(\mu^-\mu^-)}{N(\mu^+\mu^+) + N(\mu^-\mu^-)} \tag{4.1}$$

where $N(\mu^+\mu^+)$ is the number of events with $b \to \mu^+ X$ and $\overline{b} \to \mu^+ X$, and $N(\mu^-\mu^-)$ is the number of events with $b \to \mu^- X$ and $\overline{b} \to \mu^- X$.

In the Standard Model, b quarks will hadronize with other quarks to form the following mesons which have a branching ratio to $\mu^-\nu_\mu X$ of about 11%: $\overline{B}, B^-, \overline{B}^s$. Additionally, 10% of b quarks will form b-baryons which have a branching ratio to $\mu^-\nu_\mu X$ of about 9%. In addition to these direct semimuonic decays, all these hadrons can produce μ^+ by way of charm hadrons which decay semimuonically. Neutral B mesons can produce μ^+ by oscillating before undergoing a semimuonic decay.

- Direct, $b \to \overline{B}, \to \mu^- X$
- Mixed, $b \to \overline{B} \to B \to \mu^+ X \quad (B^0 \leftrightarrow \overline{B^0}, B_s^0 \leftrightarrow \overline{B_s^0})$
- Sequential, $b \to \overline{B} \to DX \to \mu^+ X$
- Mixed sequential, $b \to \overline{B} \to B \to \overline{D}X \to \mu^- X$

Dimuon pairs come about when both the b and $\overline{b}$ quarks decay in one of the ways listed above. Same-sign muon pairs arise in $b\overline{b}$ events through neutral B meson mixing or through sequential

decays of B hadrons ($b \to c \to \ell$). The CP asymmetry described above specifically excludes sequential decays; it is the CP asymmetry arising from neutral B meson mixing. The Standard Model prediction for A_{CP} is of order 10^{-3}, so an observation of a large asymmetry would be indicative of new physics. The CP asymmetry in B^0-$\overline{B^0}$ mixing has been measured to be quite small [49, 50], so a measurement of A_{CP} at the Tevatron can be interpreted as a search for CP violation in the mixing of B_s mesons.

Previous measurements were performed at CDF in Run Ia [51] and LEP [52] with a precision of about 1%. In 2006 D0 performed a measurement [54] that was consistent with zero with an uncertainty of ~0.1%. Our analysis technique is significantly different from the D0 measurement.

4.2 Target Physics Process

In this dissertation, we utilize a sample of same-sign dimuon candidate events originating from $b\overline{b}$ production, where each muon originates from the decay of a unique B hadron. Our sample of same-sign dimuon events includes contributions from other real sources of muons and from fake muon candidates. We must account for these contributions in order to accurately extract the CP asymmetry arising from B decays. To carry out this work, we follow the technique of Refs. [51, 55, 56] and fit the two-dimensional impact parameter distribution of the two muon candidates. This takes advantage of CDF's superior impact parameter resolution to unfold contributions from prompt[1], charm and B sources.

Same-sign muon candidate pairs may originate from several different types of events:

- prompt sources(PP)
  - one real prompt muon, and one K or π reconstructed as a muon (a fake muon candidate)
  - two fake muon candidates
- $B\overline{B}$ hadron pairs where each meson decays semileptonically to a muon (BB)
  - one B meson decays after mixing (*e.g.* $b \to \overline{B} \to B \to \mu^+ X$)
  - one B meson decays sequentially, $b \to c \to \mu X$
- one muon candidate from a semileptonic B or C decay is present and a prompt muon candidate of the same charge is found(PB and PC).

It is interesting to note that there are no significant prompt sources of same-sign dimuon events. In addition, since charm mixing is known to be quite small, $c\overline{c}$ events cannot contribute real same-sign dimuons. Both PP and CC can contribute to the same-sign dimuon data when at least one reconstructed muon candidate is a hadron from prompt or charm sources respectively which fakes a muon.

[1] A prompt track object is a track which extrapolates back to the primary interaction point within the resolution of track reconstruction. Prompt tracks are contrasted with tracks coming from heavy flavor decays (charm and B) which have a significant lifetime. Tracks from these decays extrapolate back to the point of the decay which is displaced from the primary interaction point.

Using a sample of data enriched in muons from semileptonic B decays, a template fitting method based on impact parameter significance ($d_0/\sigma(d_0)$) is used to identify the fraction of BB in same-sign pairs. This method takes advantage of the longer lifetime of B hadrons compared to other sources of real muons. The fitting is performed separately for the $\mu^+\mu^+$ and $\mu^-\mu^-$ case in order to correct for asymmetries introduced by varying muon fake rates and any detector or trigger asymmetries. Any residual difference in the number of $\mu^+\mu^+$ and $\mu^-\mu^-$ pairs is the measured CP asymmetry. This is complimentary to measurements of CP violation in exclusive decay modes. Assuming the standard model, CP violation expected in $B\overline{B}$ mixing may be observed, while a large observation of A_{CP} would indicate physics beyond the standard model.

4.3 Strategy Overview

The selected trigger provides a large dimuon event collection enriched in muons from B decays. Initial data selection allows the elimination of obvious backgrounds such as cosmic rays and sequential dimuons where both muons come from a single b quark via two sequential semileptonic decays. The trigger path and initial analysis cuts are described in Section 4.4 and following. These signal dimuon events still contain prompt and charm contributions. Chapter 5 describes the dimuon $d_0/\sigma(d_0)$ fitting method used to extract the fraction of $\mu^+\mu^+$ and $\mu^-\mu^-$ events that are from b events. The additional analysis components are corrections to the raw asymmetry of the fitted $\mu^+\mu^+$ and $\mu^-\mu^-$ numbers. Some of the dimuon events fitted to be of B origin in fact contain a kaon or pion from a B decay which fakes a muon in the detector. The significant asymmetry introduced by these events must be measured as a correction and is discussed in Chapter 6. Finally, the detector or event trigger may introduce a $+/-$ asymmetry which must also be applied as a correction. This evaluation is also described in Section 6.

4.4 Triggered Data Sample

The dimuon data used for this dissertation was collected between March 1, 2002 and January 30, 2007 and it corresponds to an integrated luminosity of 1.65 fb^{-1}. Events are preselected from CDF stored data according to the trigger path. The selection criteria for the trigger used are:

- At Level 1: Two muons with hits in the CMU chambers are required. These stubs must extrapolate to tracks with at least 1.5 GeV of transverse momentum.
- At Level 2: At least one of the Level 1 muons must have a corresponding CMP stub and at least 3.0 GeV of transverse momentum.
- At Level 3: Both muons are required to have CMP stubs and be of $P_T \geq 3.0$ GeV. Additionally
  - The ΔX between each CMP stub and its corresponding COT track, ΔX_{cmp}, must be < 40 cm
  - $\Delta X_{cmu} < 20$ cm

– The invariant mass of the two muon tracks ≥ 5.0 GeV

There are several advantages of this trigger. First, it is inclusive in that it imposes no opposite charge requirement in contrast to other dimuon triggers used for targeting various resonances. Second, the invariant mass cut prevents both muons coming from the same b, since the b hadron mass is < 5 GeV. In addition to selection based on the event trigger only events which come from data classified as *good for physics*[2] for the CMU, CMP, SVX, and COT detectors is used.

4.5 Cosmic Ray Finding

Inherent in the triggering process, the bunch structure of beams creates timing structure for collisions. This timing can be exploited to reject most cosmic rays not coincident with beam collisions. The detector's front-end electronics are synchronized with the Tevatron clock cycles to accomplish this cosmic rejection. There are still cosmic events coincident or nearly coincident with collisions that must be removed from the data passing the trigger. A muon from a cosmic ray interaction passing through the detector will look very like a displaced opposite-sign dimuon event. We examined further timing-related cosmic rejection tools which are available in CDF analysis software [57], but found that not all the cosmics were eliminated by applying these cuts. We were also concerned about potentially higher rejection of OS events.

A simple rejection cut based on the angle between the trigger muons, $\delta\phi$, was actually found to be efficient by another CDF analysis group using dimuon data [56]. Therefore, we tag cosmic rays by a selection of muon pairs where $\delta\phi \leq 3.135$ radians. The $\delta\phi$ method removes the remaining cosmic rays from the opposite-sign sample while retaining over 99% of the signal events. Every event with a cosmic tag is vetoed both from the analysis data and the $\Upsilon \to \mu^+\mu^-$ data used in the prompt (PP) template. Figure 4.1 shows the removal of cosmic rays in the OS dimuon dataset.

4.6 Events Selection

Most events in the selected dataset have two and only two 3 GeV CMUP muon candidates, however in cases where there are more, every pair is evaluated against the following cuts. Both trigger muon tracks were required to have at least 3 COT segments with ≥ 5 hits per segment for both axial and stereo superlayers(SL). In addition the muon candidates were required to have at least 3 $r-\phi$ SVX hits, and no L00 hits are used. The absolute Z_0 value of each muon track were required to be less than 60 cm and the absolute value of the difference between the tracks was required to be less than 5 cm. The impact parameter of each track, d_0 is required to be at most 3 mm, and the significance, $d_0/\sigma(d_0)$ at most 62[3]. These Z_0 and d_0 selection cuts help to

[2] The *good for physics* classification is made on subsets of each data store which are taken continually by the trigger system. The crew on shift in the control room verify that all of the trigger system is functioning properly and the sub detectors are calibrated and active. A sampling of the data is processed immediately and monitored to verify standard distributions.

[3] As will be seen later, the significance distribution drops extremely rapidly for the data, so evenly increasing uneven bin sizes are used for the fitting to maximize the precision at low significance and statistics at high

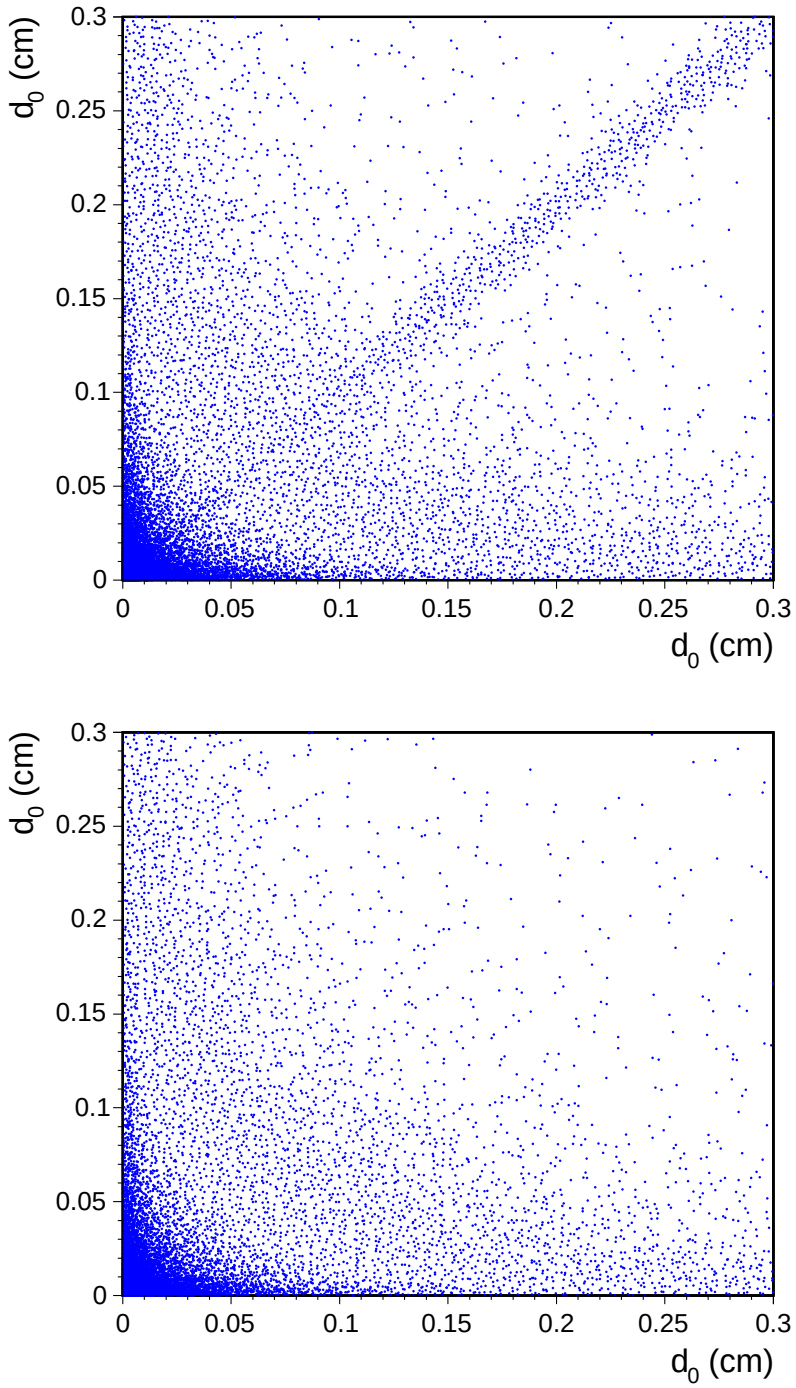

Figure 4.1: Triggered events meeting the selection requirements are included in these plots with the d_0 of each muon along one axis. The top plot does not include the $\delta\phi$ cosmic rejection, and cosmic ray events are visible along the $d_0^1 = d_0^2$ diagonal. The bottom plot shows the same data after the cosmic rejection.

eliminate tracks not coming form the primary interaction region and pairs not coming from the same primary vertex. Finally, only pairs for which the invariant mass of the trigger tracks was $\geq$ 5 GeV/c^2 were selected to eliminate contributions where both muons come from a single b quark in a sequential decay chain. Additionally, for opposite-sign pairs, the mass region which includes the upsilon resonances is excluded. These event selection criteria are summarized in Table 4.1. More than one muon candidate pair meeting these criteria can be found in some events. In this case all pairs are analyzed.

Axial hits	$\geq$ 3 SL with $\geq$ 5 hits
Stereo hits	$\geq$ 3 SL with $\geq$ 5 hits
Silicon $r-\phi$ hits	≥ 3
$\lvert Z_0 \rvert$	$\leq$ 60 cm
$\lvert \delta Z_0 \rvert$	$\leq$ 5 cm
$M_{\mu\mu}$	$\geq$ 5 GeV
d_0	$\leq$ 0.3 cm
$d_0/\sigma(d_0)$	≤ 62
excluded M_Υ (OS only)	9.12 GeV $\geq M_{\mu\mu} \geq$ 10.5 GeV

Table 4.1: Event selection for pairs of muon tracks and stubs

After applying these cuts about 1.1 million pairs remain:

- 655,669 $\mu^+\mu^-$ pairs
- 235,085 $\mu^+\mu^+$ pairs
- 205,158 $\mu^-\mu^-$ pairs

These cuts are also used for the $\Upsilon \rightarrow \mu^+\mu^-$ sample utilized for the (PP) template with the exception of the invariant mass cuts. The PP data selection is described in section 5.2.2.

4.6.1 Trigger Object Confirmation

Each muon candidate pair selected for the analysis is initially subjected to the prerequisite of being in an event meeting all the CDF trigger requirements described in Section 4.4. Additionally, an examination is made of all L1 track information and L1 hit information in the muon chambers associated with muon candidate pairs passing the analysis cuts. This confirmation is meant to verify that each selected muon candidate pair meets the L1 trigger requirements. There were found to be about 3% of the selected muon candidate pairs not meeting the L1 trigger selection, meaning that while two muon candidates in the event do pass the trigger, they are not the same muon candidates passing the analysis selection cuts. All these pairs are discarded since we correct for the measured trigger efficiency asymmetry as described in Section 6.2.4.

significance. Significance being a number of standard deviations, 62 was the integer value nearest to the point where the the statistics in the 2-dimensional bins were too small to use. Of the data passing the other analysis selection requirements only around 1.5% of the muon candidate pairs fall outside of 62 sigma.

4.6.2 Signal $\mu\mu$ Kinematic Distributions

Figures 4.2 - 4.4 shows some indicative distributions of kinematic variables in the sample of selected signal dimuon data. In addition to looking for normal distributions of individual muon candidates such as P_T, correlated dimuon quantities are examined, particularly variables on which analysis cuts are made such as invariant mass, and $\delta(Z_0)$. Also, profiles of some kinematic variables over a range of impact parameter are examined since the impact parameter distribution is used to separate BB contributions from other dimuon sources.

One of the most significant data histograms is the 2D impact parameter which is used to determine the fractions of the sources producing muon candidate pairs as described in the next section. Figures 4.6 and 4.5 show the 2D impact parameter histogram for all the pairs passing the analysis cuts, the x-projection of the impact parameter histogram, and the distribution of impact parameter errors for each pair. The muon order has been randomized.

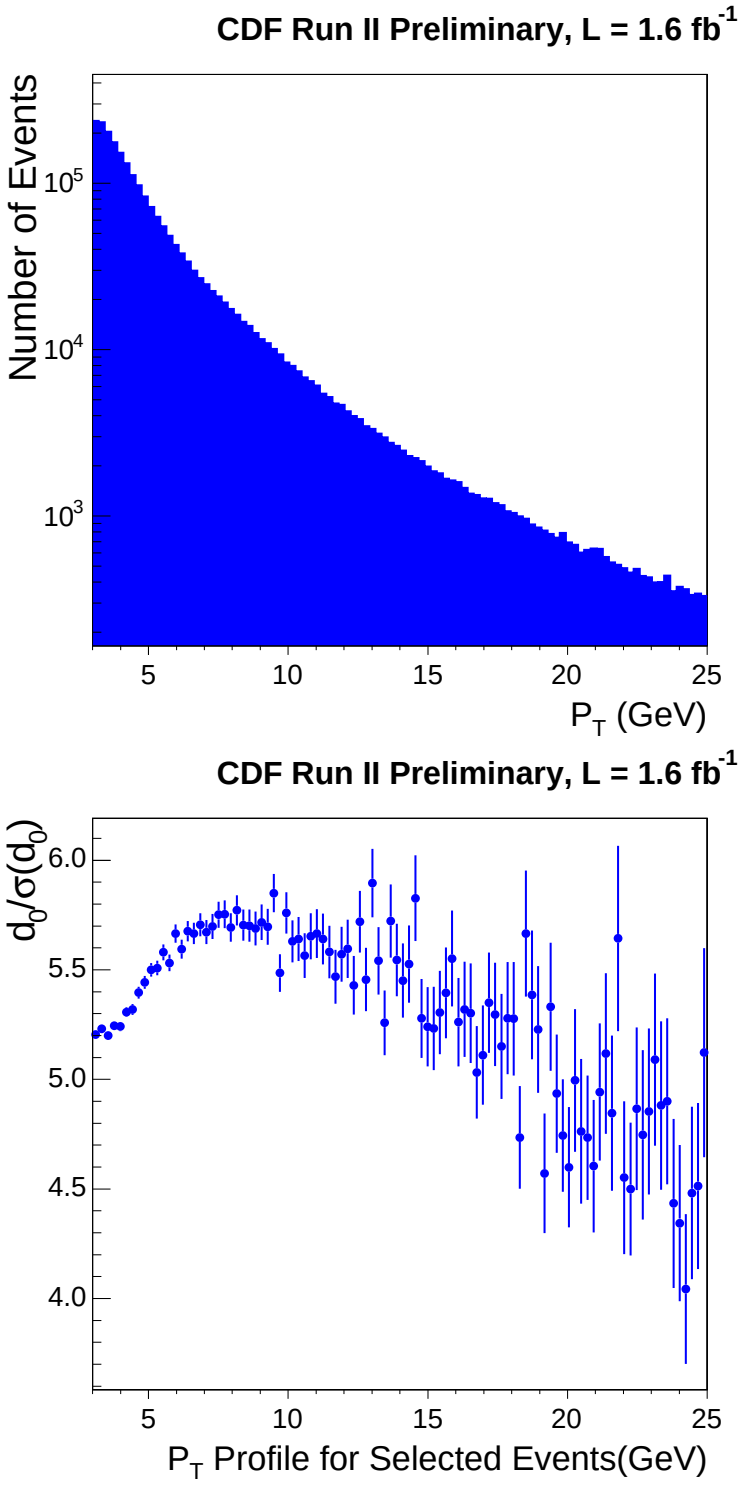

Figure 4.2: Signal dimuon candidate kinematic distributions for all muon candidate pairs passing analysis cuts: (top) P_T of both muons, and (bottom) P_T profile over d_0 range. (The profile is the average d_0 for all pairs in a particular P_T bin.)

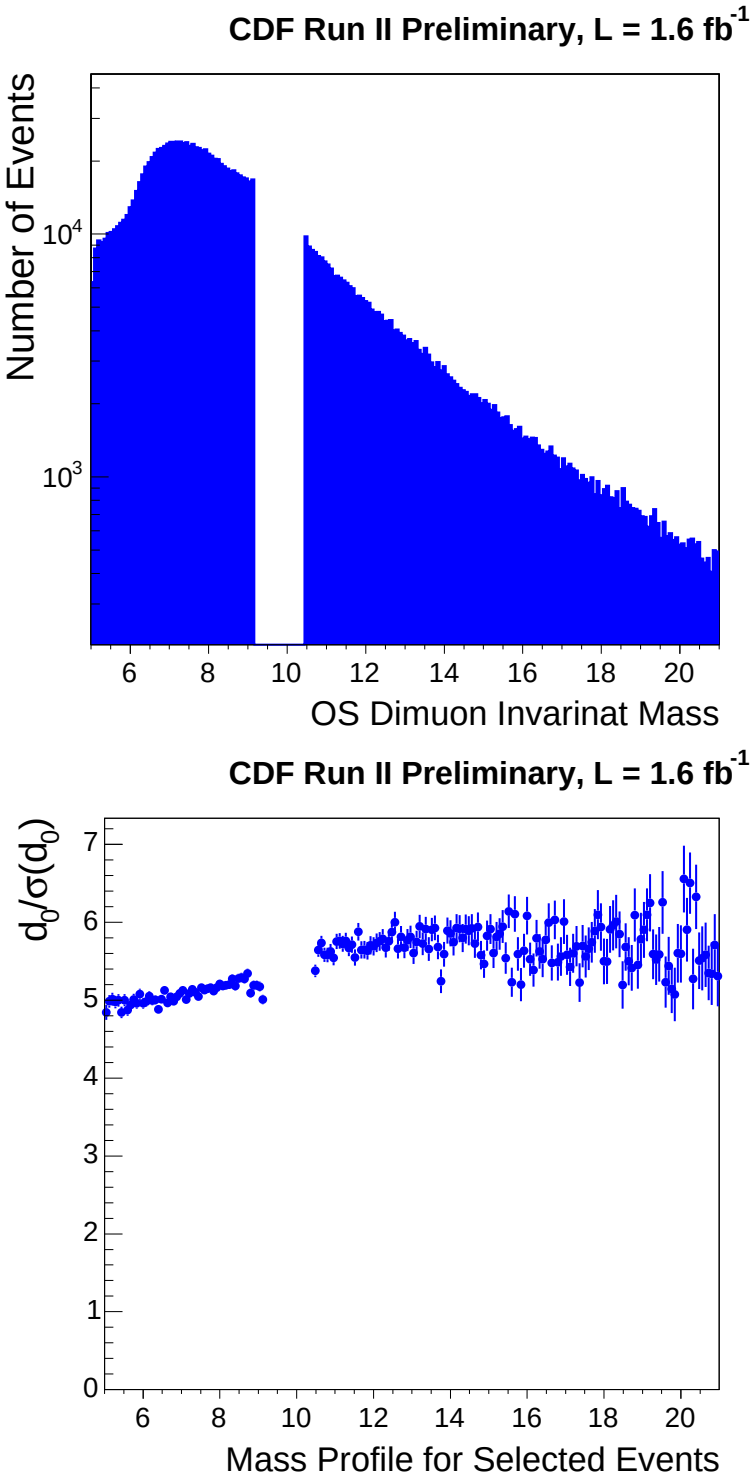

Figure 4.3: Signal dimuon candidate kinematic distributions for all muon candidate pairs passing analysis cuts (does not include same-sign pairs in the Υ mass region): (top) Invariant mass, and (bottom) Invariant mass profile over d_0 range. (The profile is the average d_0 for all pairs in a particular mass bin.)

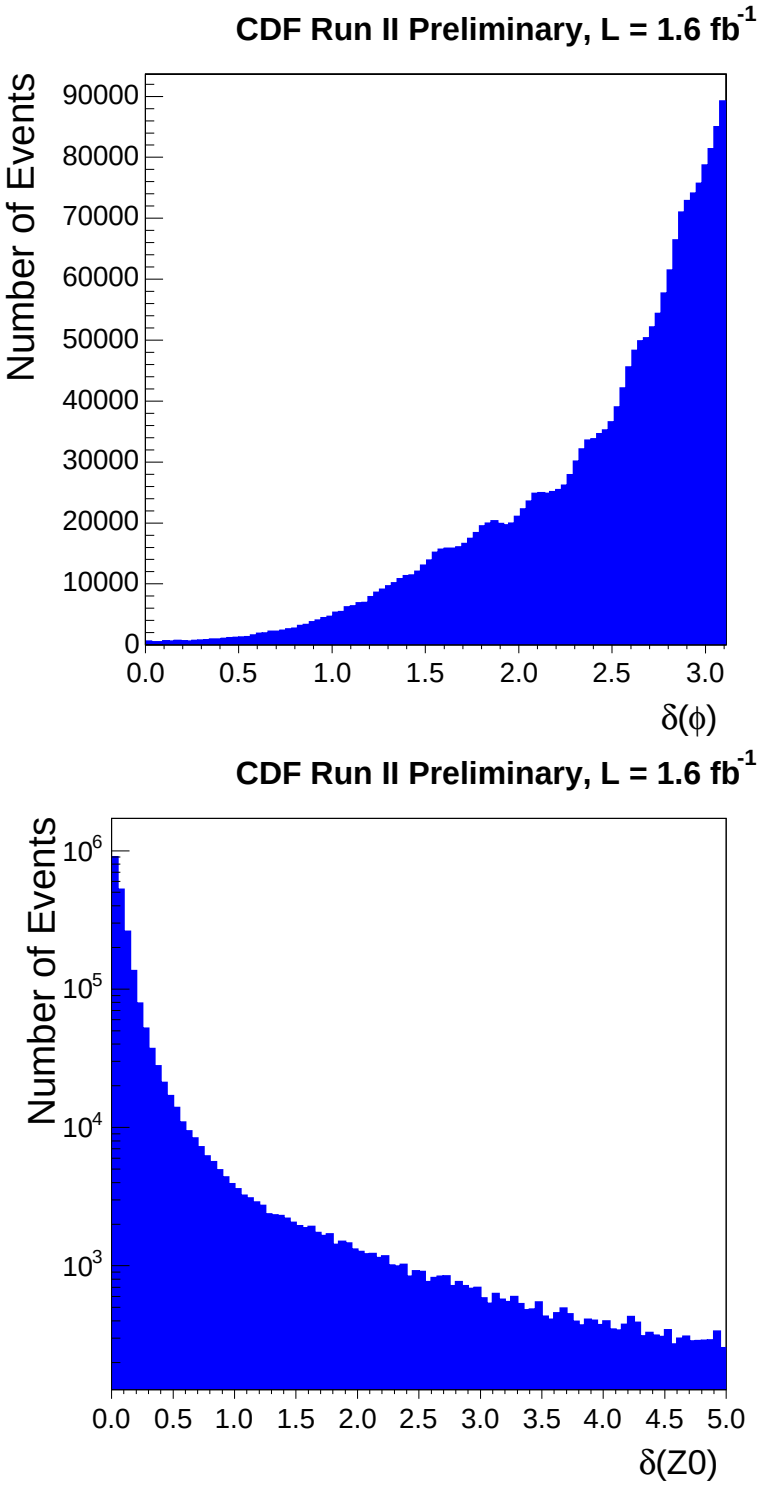

Figure 4.4: Signal dimuon candidate kinematic distributions for all muon candidate pairs passing analysis cuts: (top)$\delta(\phi)$ and (bottom) $\delta(Z_0)$ between the pair.

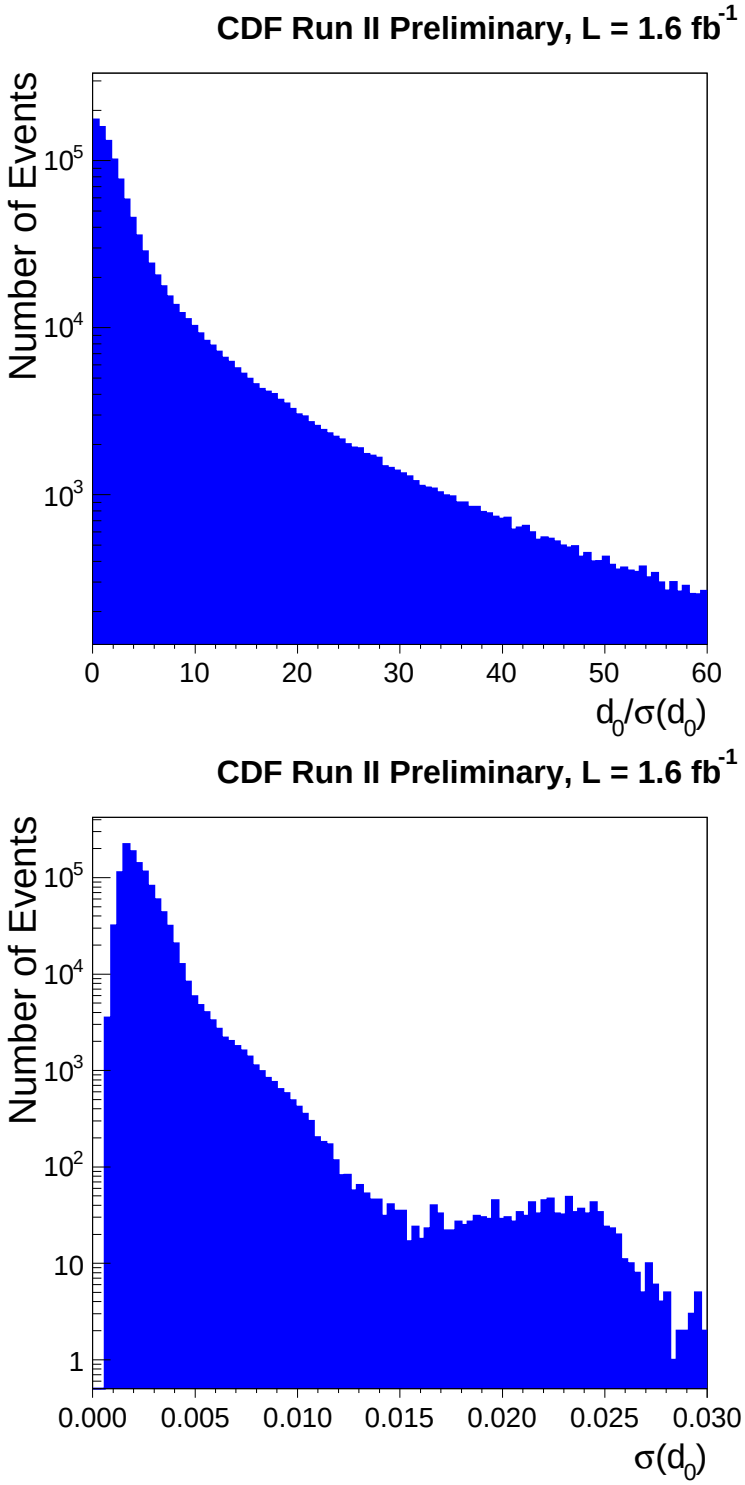

Figure 4.5: (top) Projection of impact parameter distribution, and (bottom) Distribution of impact parameter error for all muon candidate pairs passing analysis cuts.

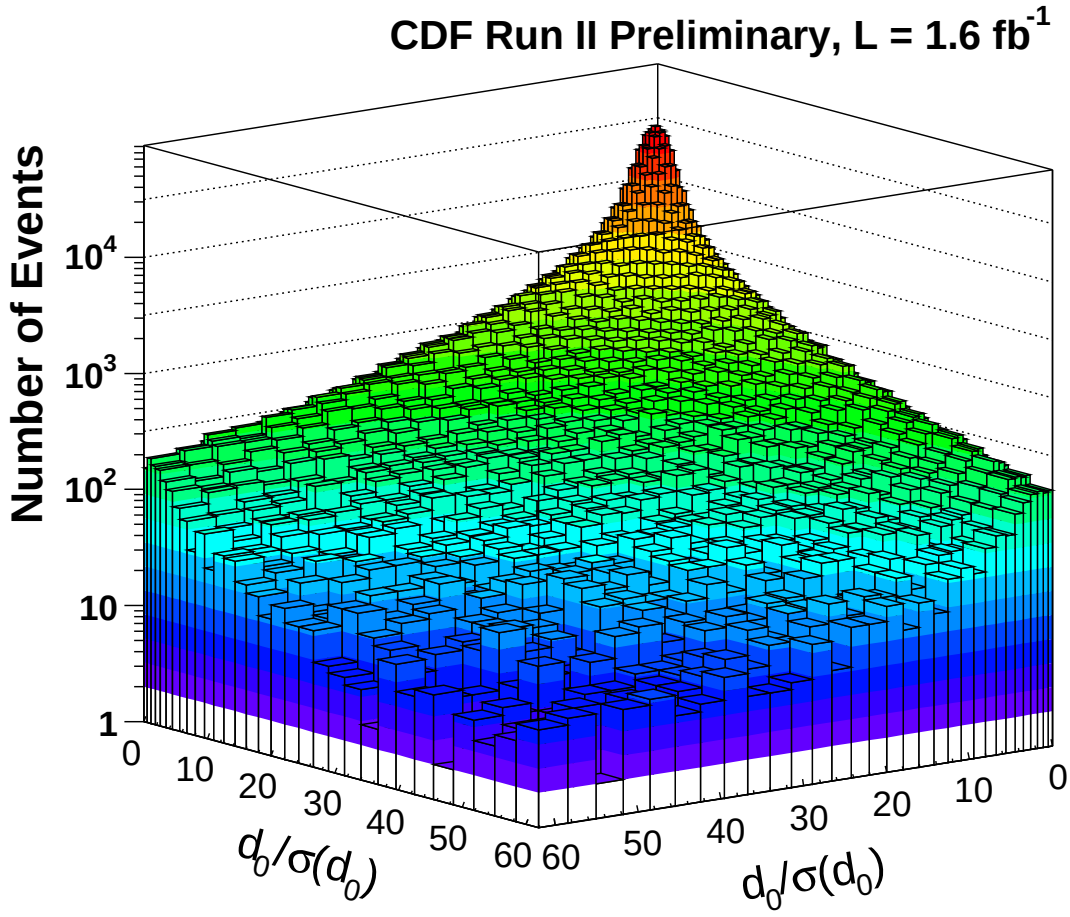

Figure 4.6: Dimuon candidate impact parameter significance distribution for all same-sign and opposite-sign pairs passing analysis cuts. One muon candidate is plotted along each axis.

Chapter 5

Impact Parameter Fitting

This chapter describes the method by which dimuon candidate pairs coming from $b\overline{b}$ production can be isolated. The fraction of these signal pairs is measured with respect to the whole dimuon dataset.

5.1 Impact Parameter Significance

The impact parameter, the distance of closest approach to the collision point, of a muon provides a good way to identify muons originating from heavy flavor. Prompt tracks in the absence of a measurement resolution and failed pattern recognition would have impact parameters of 0, but these effects cause a Gaussian smearing and some small non-Gaussian tails respectively. Additionally, tracks from B hadrons will on average have a much longer impact parameter than prompt tracks due to their longer lifetime. Figure 5.1 shows a depiction of a typical track impact parameter from a B decay.

Since a large fraction of events with muons from B decays would be lost separating prompt and charm muons from B muons by cutting on impact parameter, a binned negative log likelihood fit is performed using two-dimensional impact parameter significance templates with one muon plotted along each dimension to determine the B content. The 2D method allows the identification of PB and PC fractions where only one muon comes from longer lived heavy flavor. While there is no contribution expected from $c\overline{c}$ to the same-sign real dimuon sample, a CC component is included in the same-sign fits for cases where a hadron from a c decay fakes a muon. The 2D templates are constructed by randomly selecting values from the appropriate $d_0/\sigma(d_0)$ distributions. The BB template uses the 1-dimensional distributions for muons coming from B for each axis, and PB template selects one axis from the B distribution and one from the P distribution. The Minuit function minimization and error analysis program as implemented in the ROOT framework is used to perform the fitting [61].

Because of poor fit quality in the tail of the impact parameter distribution (see Figure C.1 in Appendix A) the template fitting method was modified to incorporate the different uncertainty in the impact parameter measurement on a track by track basis. The impact parameter significance, $d_0/\sigma(d_0)$, is essentially a measure of how significantly different each track's impact parameter is from zero. Again, the longer lived heavy flavor has high impact parameter significance, but without the smearing effect of differences in impact parameter measurement error. Each $d_0/\sigma(d_0)$ template has variable binning to maximize the resolution in the low significance region with high

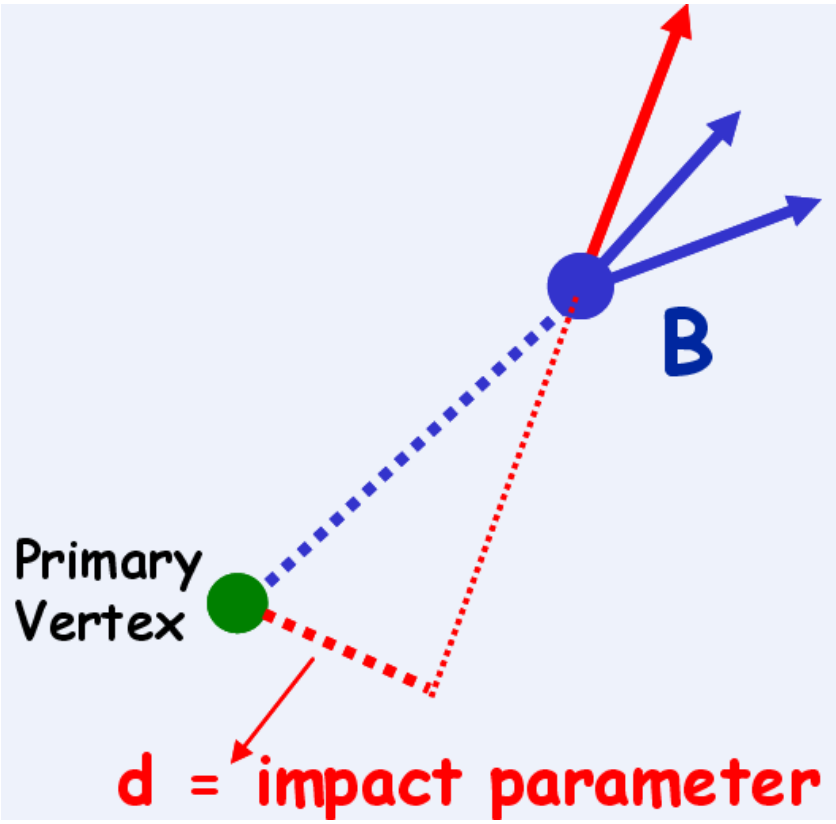

Figure 5.1: Example of a typical track impact parameter from B decay.

statistics. Thirty-one bins on each axis run from a significance of 0-62σ. As discussed in Section 4.6, only 1.5% of the total data passing the other selection cuts are beyond 62σ in significance, and the statistics population of the distribution in that range is insufficient for fitting.

5.2 Templates Modeling $\mu\mu$ Sources

Two dimensional templates were constructed to model the signal dimuon candidate pairs coming from BB and candidate pairs coming from each background process.

5.2.1 Monte Carlo Distributions

Impact parameter significance templates were built from 1-dimensional distributions for muons coming from B, C, and P sources. The B distribution is created using PYTHIA Monte Carlo(MC) (see Appendix D for description of MC samples). In EVTGEN[1] we are forcing the b quark in $b\overline{b}$ events to decay to a muon while the $\overline{b}$ quark decays freely. Nearly 90% of hadrons containg b quarks decay to a final state without a muon. Both decays need to contain a muon for an

[1] EVTGEN is a special event generator for more accurately handling B decays. See also Appendix D.

accurate template which models signal events. So, forcing one muon decay boosts the event statistics by reducing the necessary processing time. We investigated whether any bias might be introduced by forcing the muon decays for $b\overline{b}$ events and found no evidence that the impact parameter significance was affected in this way. Only events containing a muon with $P_T \geq 2.8$ and $|\eta| \leq 0.8$ were used. The detector and trigger response is then simulated for these events.

Using the simulated MC events like the selected data, pairs of two trigger CMUP muons meeting the same analysis cuts used for muons in the data are required. $B\overline{B}$ mixing is turned off in Monte Carlo. MC events which contain $c\overline{c}$ quark production are also analyzed in nearly the same manner to create the C impact parameter significance distribution. The two differences for the $c\overline{c}$ distribution are that any events containing any b quark production are excluded from the charm templates and there were no forced muon decays.

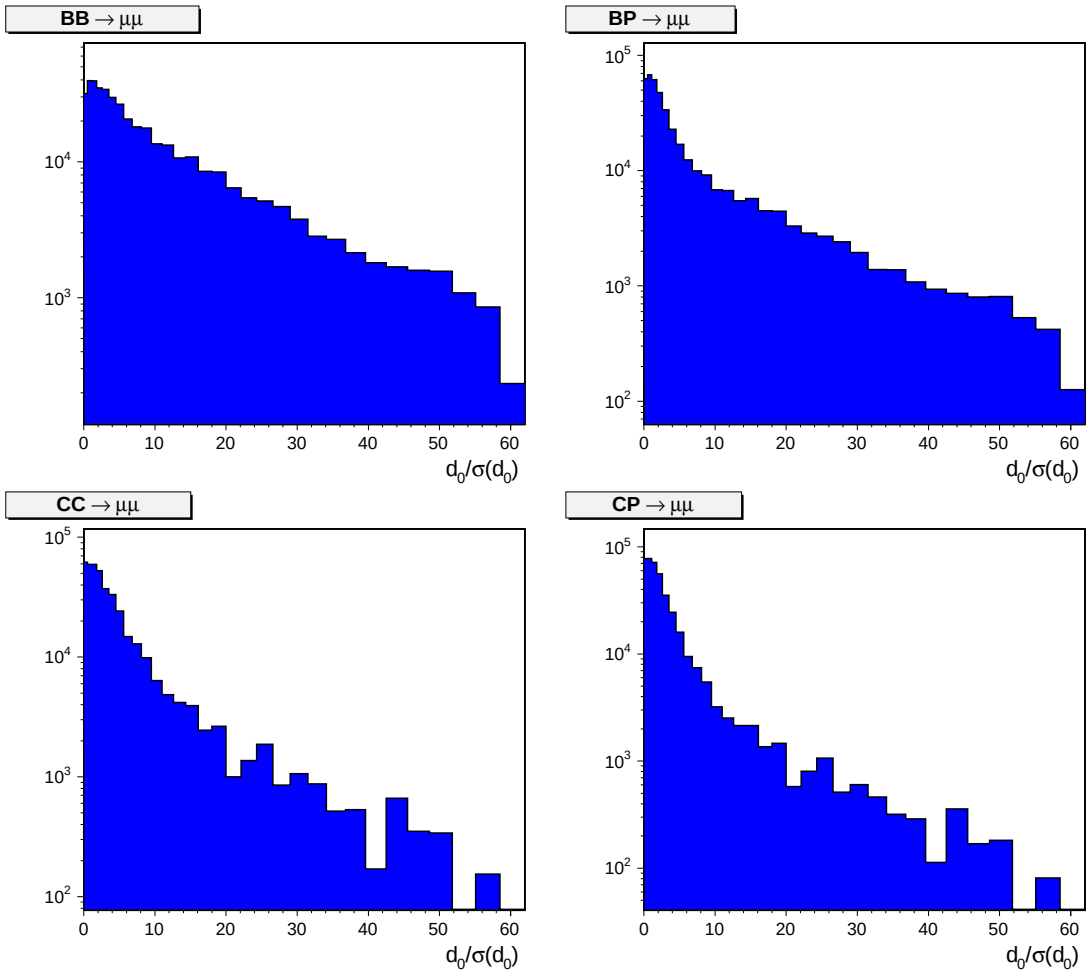

Figure 5.2: 1D Projections of the dimuon $d_0/\sigma(d_0)$ templates for each of the following templates: (a)both muons originate from a B hadron, (b)one muon is from B and one is a prompt track, (b)both muons originate from a C hadron, and where (d)one muon is from C and one is a prompt track.

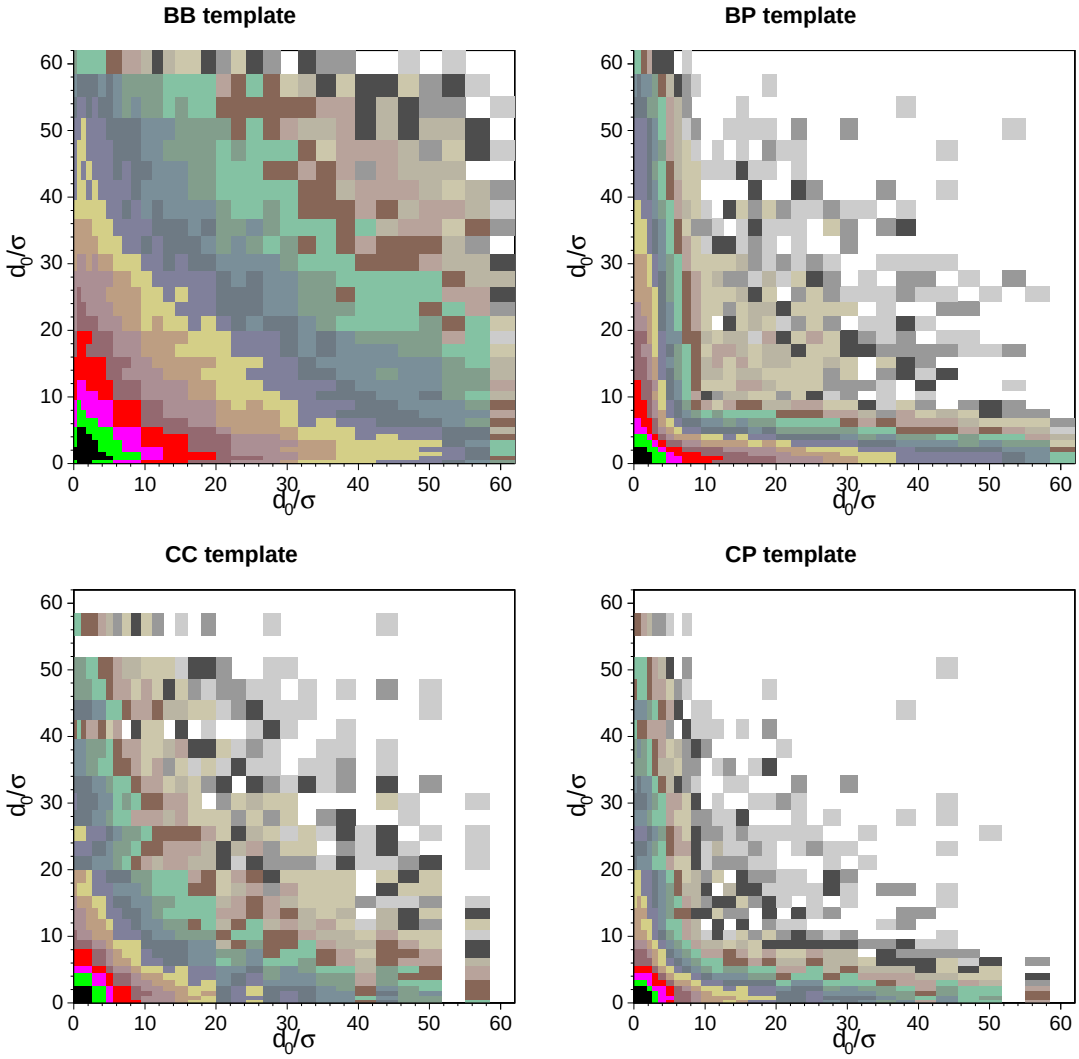

Figure 5.3: Dimuon $d_0/\sigma(d_0)$ templates for each of the following templates: (a)both muons originate from a B hadron, (b)one muon is from B and one is a prompt track, (b)both muons originate from a C hadron, and where (d)one muon is from C and one is a prompt track.

5.2.2 Prompt Distribution

It is difficult to properly model a prompt impact parameter distribution where detector response and resolution play so significant a role. Therefore, the $d_0/\sigma(d_0)$ template accounting for cases where muons originate from prompt sources is constructed from data in the mass range which is excluded from the main analysis. Figure 5.4 shows the upsilon mass region used to construct the distribution of prompt muons. Events for the PP template meet all the same analysis cuts as normal data events except they are required to have 9.12 GeV $< M_{\mu\mu} <$ 10.5 GeV. Dimuon impact parameters for events in the $\Upsilon(1S)$ and $\Upsilon(2S)$ narrow mass ranges, $9.31 < M_{\mu\mu} < 9.61$ GeV and $9.91 < M_{\mu\mu} < 10.13$ GeV respectively, are saved for the PP template. Events meeting the identical cuts are used for background subtraction in the following mass regions:

- $9.12 < M_{\mu\mu} < 9.27$ GeV
- $9.65 < M_{\mu\mu} < 9.91$ GeV
- $10.13 < M_{\mu\mu} < 10.24$ GeV

The 2D $d_0/\sigma(d_0)$ plot resulting for this background subtraction is a very pure sample of real prompt dimuons. A 1D projection of the final template used for fitting the prompt fraction is shown in Figure 5.5; the long tail models mis-measured prompt tracks.

5.2.3 Data and Monte Carlo Comparisons

A number of comparisons were made between various kinematic aspects of the Monte Carlo samples used to build impact parameter significance templates and muon pairs from the data. The MC templates used in the analyses were determined to model dimuon pairs correctly; two of the cross checks are briefly described below.

Upsilon d_0 Distributions

A set of $\Upsilon(1s)$ events was produced in Monte Carlo for the purpose of cross-checking the PP template since it is produced differently than the other templates and for the purpose of examining how well the MC simulates the d_0 error distribution. The $\sigma(d_0)$ has a slightly longer tail in the data - a mean of 0.0227 μm versus 0.0219 μm from the Monte Carlo - but the distributions are satisfactorily consistent. Of more interest is the $(d_0)/\sigma(d_0)$ which is also longer in the data (a mean of 2.01 versus 1.46 in MC). This effect is possibly due to pattern recognition failures not modeled in the MC or background subtraction in the data. However, substituting the MC template as the PP input in the fitter as a cross-check (see Section 5.6.1) affected only the PP and PC balance by a few percent and left the BB contribution unchanged.

Muon P_T Distributions

Additionally, a comparison is made between the P_T distributions of single muons used in the BB MC template and data. Muons from same sign pairs in data with $d_0 > 0.09$ cm are used to insure

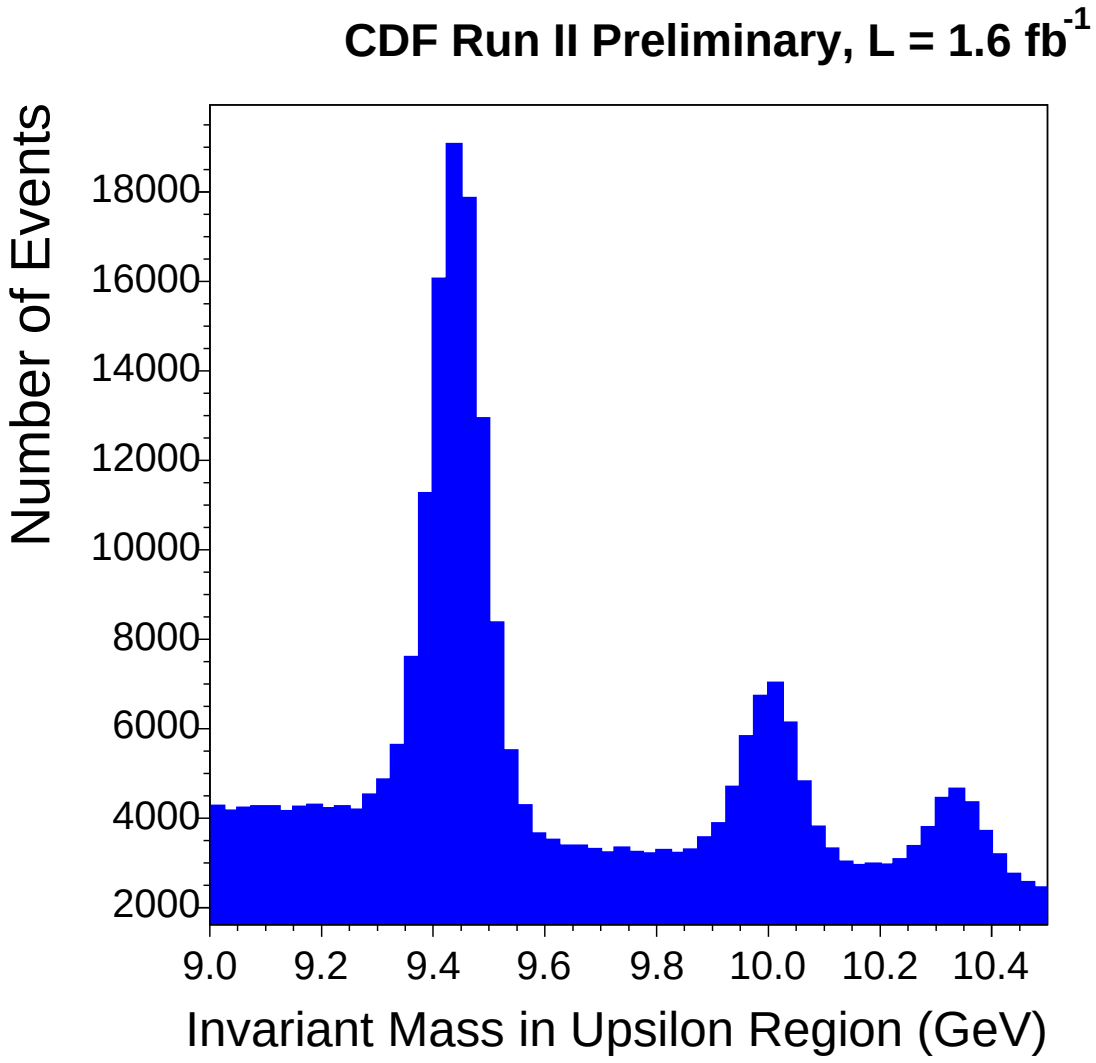

Figure 5.4: $\Upsilon \to \mu^+\mu^-$ invariant mass region. Events shown meet the same kinematic selection as the dimuon events in the asymmetry measurement, but are used instead to model muons from prompt sources.

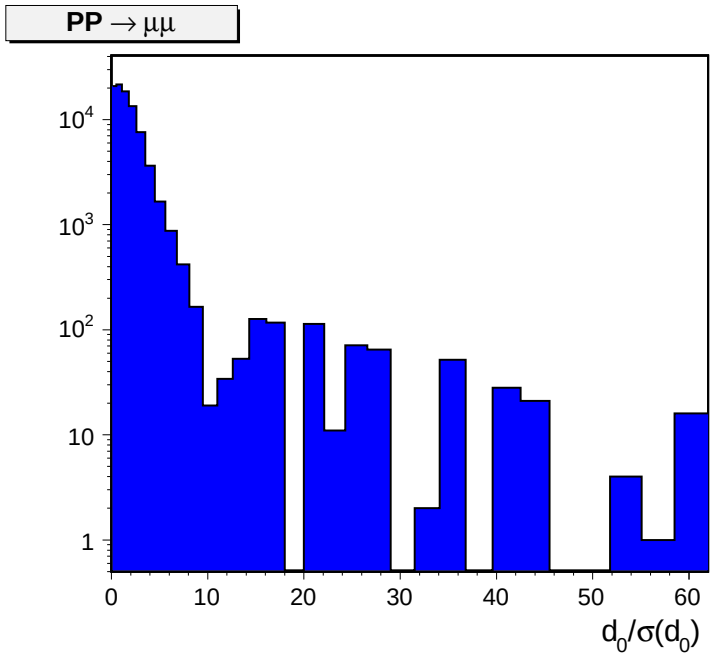

Figure 5.5: 1D Projection of the dimuon d_0 template where both muons are prompt (derived from $\Upsilon \to \mu\mu$ data)

a high purity of muons from B decays for this comparison. Figure 5.7 shows the comparison of the distributions are in good kinematic agreement.

5.3 Likelihood Fitter

While the $\mu^+\mu^-$ component fractions are not needed for the A_{CP} measurement, it is desirable to fit all three datasets together in order to examine their relative contributions. For instance, in pairs with one real muon from heavy flavor and a second fake muon from a prompt source, the probability that the combination is same-sign should be the same as the probability that the combination is opposite sign. This requires the assumption that the two reconstructed muons are uncorrelated, it makes no statement about the relationship between $\mu^+\mu^+$ and $\mu^-\mu^-$ sources. We also expect the ratio of all same-sign to all opposite-sign BB dimuons to give a reasonable value for the time-integrated mixing parameter, and the same-sign CC to be significantly smaller than the opposite-sign CC.

There are nine free parameters in the fit. The $\mu^+\mu^-$, $\mu^+\mu^+$, and $\mu^-\mu^-$ fractions of PP, BB,and PB. The fraction of pairs from CC for each dataset is defined to be $1 - f_{BB} - f_{PP} - f_{PB}$ where f_{XY} is the fraction for each free parameter component. The PC components are set to zero in the default fit. If the PC components were allowed to float freely in the fit they would return negative values. We include two cross-checks which hold PC components proportional to their respective PB fractions.

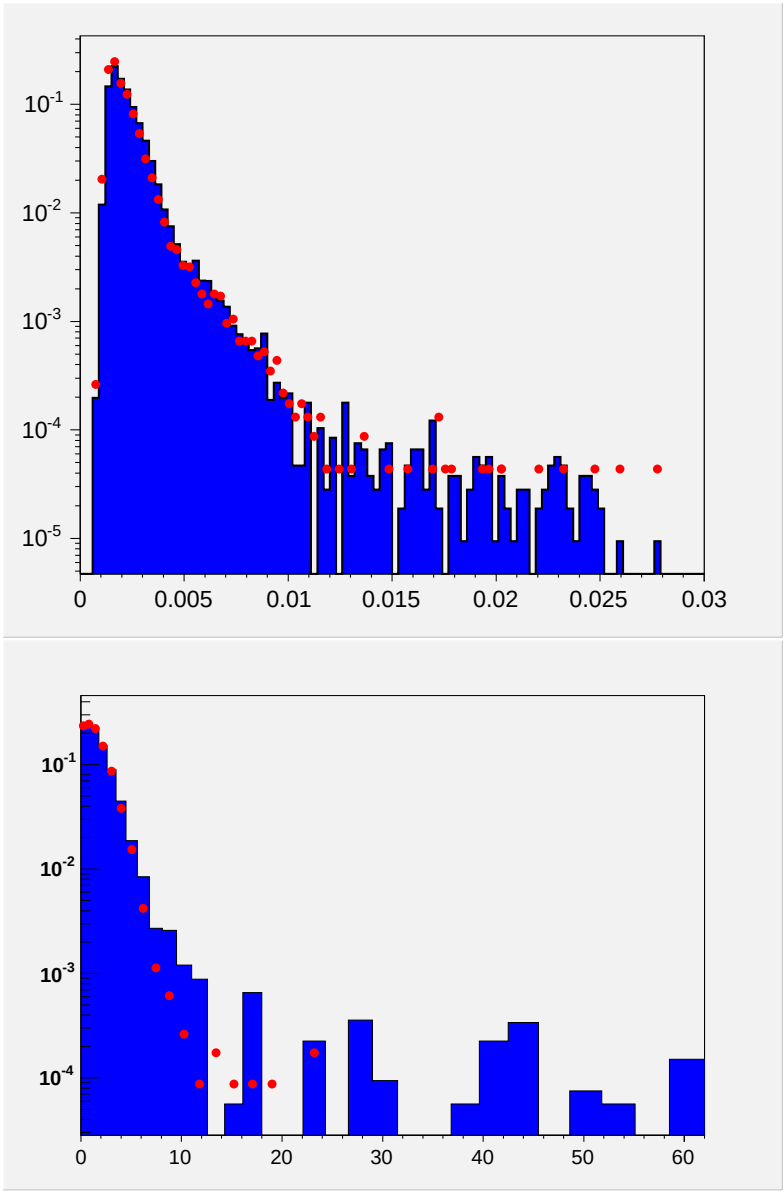

Figure 5.6: Comparison of (a)d_0 errors and (b)$d_0/\sigma(d_0)$ for data (blue) and MC (red) upsilons. All distributions are normalized to unit area.

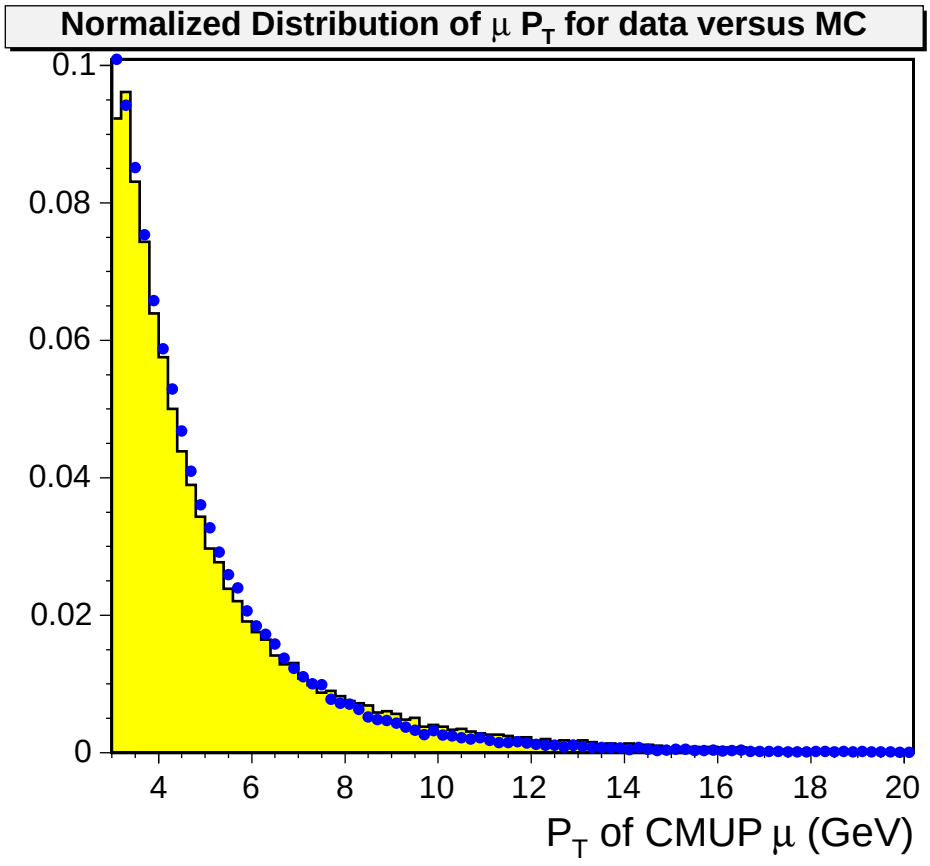

Figure 5.7: Comparison of P_T distributions for muons from B hadron decays in MC (points) and data (histogram).

The quantity minimized for each set of data is of the form given by equation 5.1 where the indices i, j run over all 2-D impact parameter significance bins. The number of pairs in a bin is given by $N_{\mu^+\mu^-}(ij)$ for the data and $N_{BB}(ij)$ for each component distribution. The fraction of the BB component is represented by f_{BB}, etc. The likelihood function is the same for the $\mu^+\mu^+$ and $\mu^-\mu^-$ cases as well:

$$\sum_i \sum_j N_{\mu^+\mu^-}(ij) * \log(f_{ij}) - f_{ij}$$
$$f_{ij} = N_{BB}(ij) * f_{BB} + N_{PB}(ij) * f_{PB} + N_{PP}(ij) * f_{PP} + N_{CC}(ij) * f_{CC}. \quad (5.1)$$

There are no bounds placed on the parameters. The constraint that fractions total 100%, built into the definition of f_{CC} is to facilitate a physical output, but we used no other constraints in the default fit. Where constraints are used in the cross-checks, a χ^2 penalty term is added to the negative log likelihood for the other constraints listed above. For example, when the number of PB same sign pairs should be equal to the number of PB opposite sign pairs within statistics, the penalty term is $\frac{(PB_{OS}-PB_{SS})^2}{|PB_{OS}+PB_{SS}|}$.

5.4 Fit Quality

Since the negative log likelihood is the quantity being minimized for this fit, there is no exact measure of fit quality [62]. One check of fit quality is to use the fitted fractions to scale each component template and compare the sum of the resulting template histograms to the data plot. The poor fit quality found at high d_0 when this check was performed led to changing the fitted quantity from d_0 to d_0 significance (see Appendix C). After the data was fitted by impact parameter significance the quality of fit defined by the comparison of projections of the components times fitted fractions to the data improves markedly for the combined same-sign sample though still not quite as good as the opposite-sign sample, see Figure 5.10.

Another measure used to quantify the fit quality is a χ^2 variable constructed from the bin-by-bin comparison of the fit parameters to the data in each bin. In this case the $\mu^+\mu^+$ and $\mu^-\mu^-$ contributions are smaller than the $\mu^+\mu^-$, but the combined fit quality is $\chi^2/DOF^2 = 4.20$. This χ^2/DOF is large due to the fact that it considers only simple Gaussian errors on the data, and no uncertainty for template statistics or fit parameter error. It is used to quantify the relative fit quality of the various cross-checks.

Finally we performed a scan of $\pm 3\sigma$ around the minimum of each parameter after the optimization. This check demonstrates that the parameter minimization is well behaved. The results can be found in Figures 5.11 to 5.13.

[2] degrees of freedom

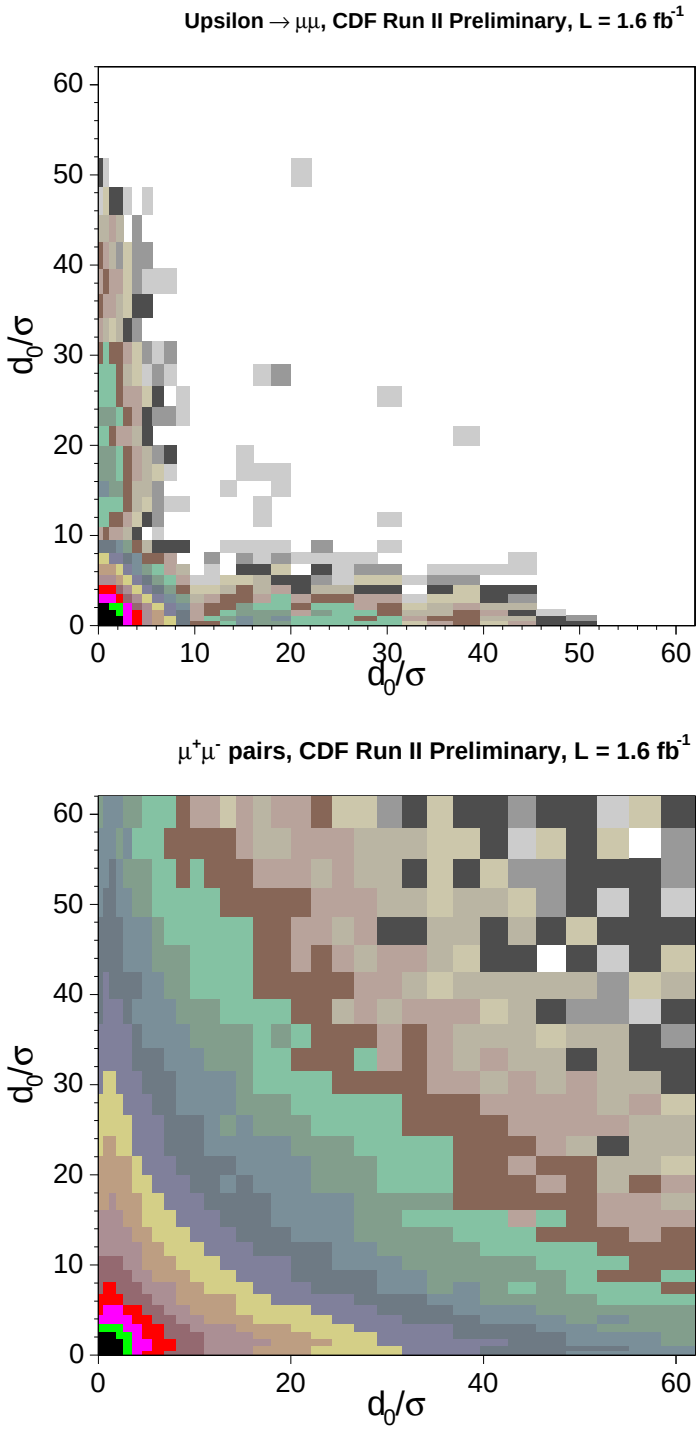

Figure 5.8: Two-dimensional impact parameter significance distributions for PP (top) and $\mu^+\mu^-$ (bottom) dimuon pair data.

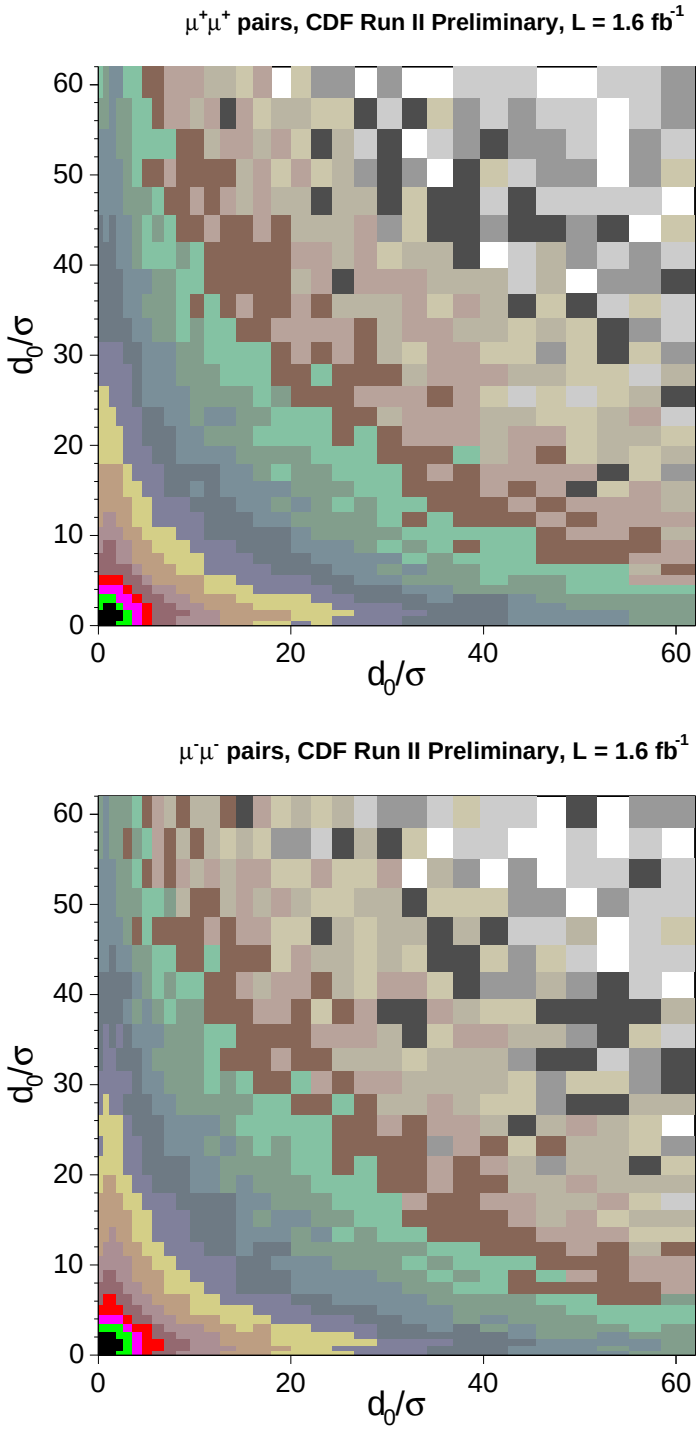

Figure 5.9: Two-dimensional impact parameter significance distributions for $\mu^+\mu^+$ (top) and $\mu^-\mu^-$ (bottom) dimuon pair data.

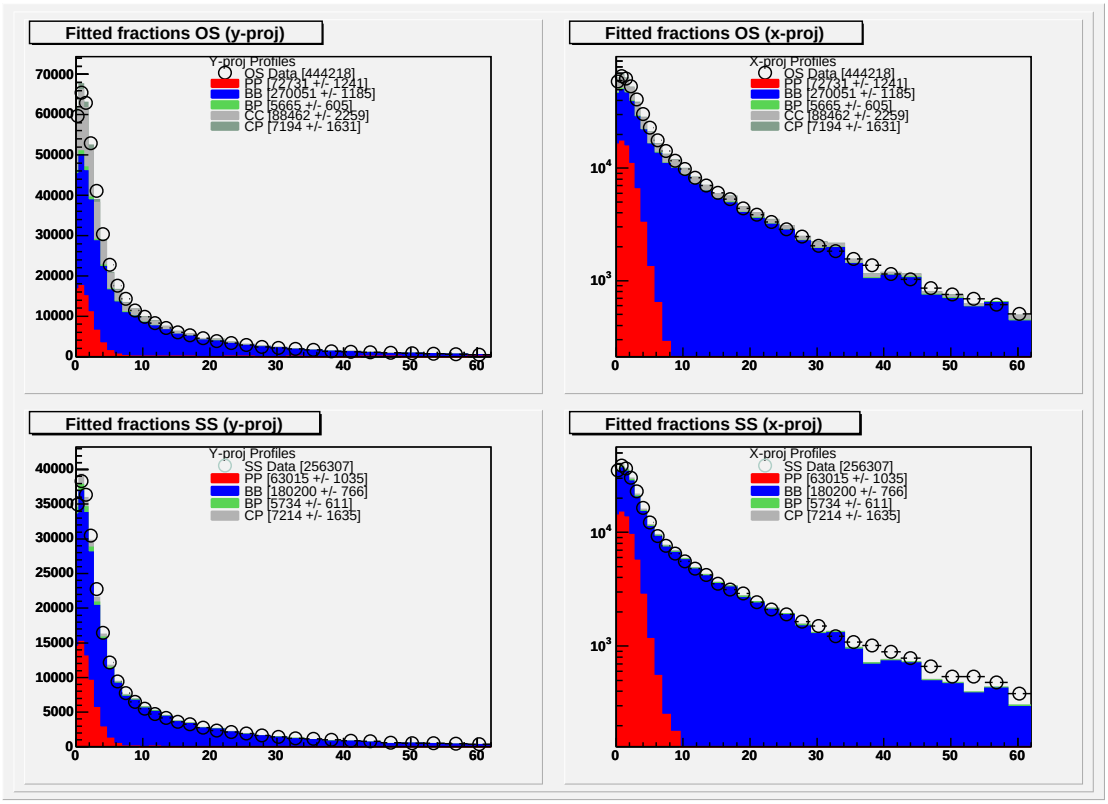

Figure 5.10: Opposite-sign (top) and combined same-sign (bottom) fitted projections of output fractions compared to data on log and linear scale

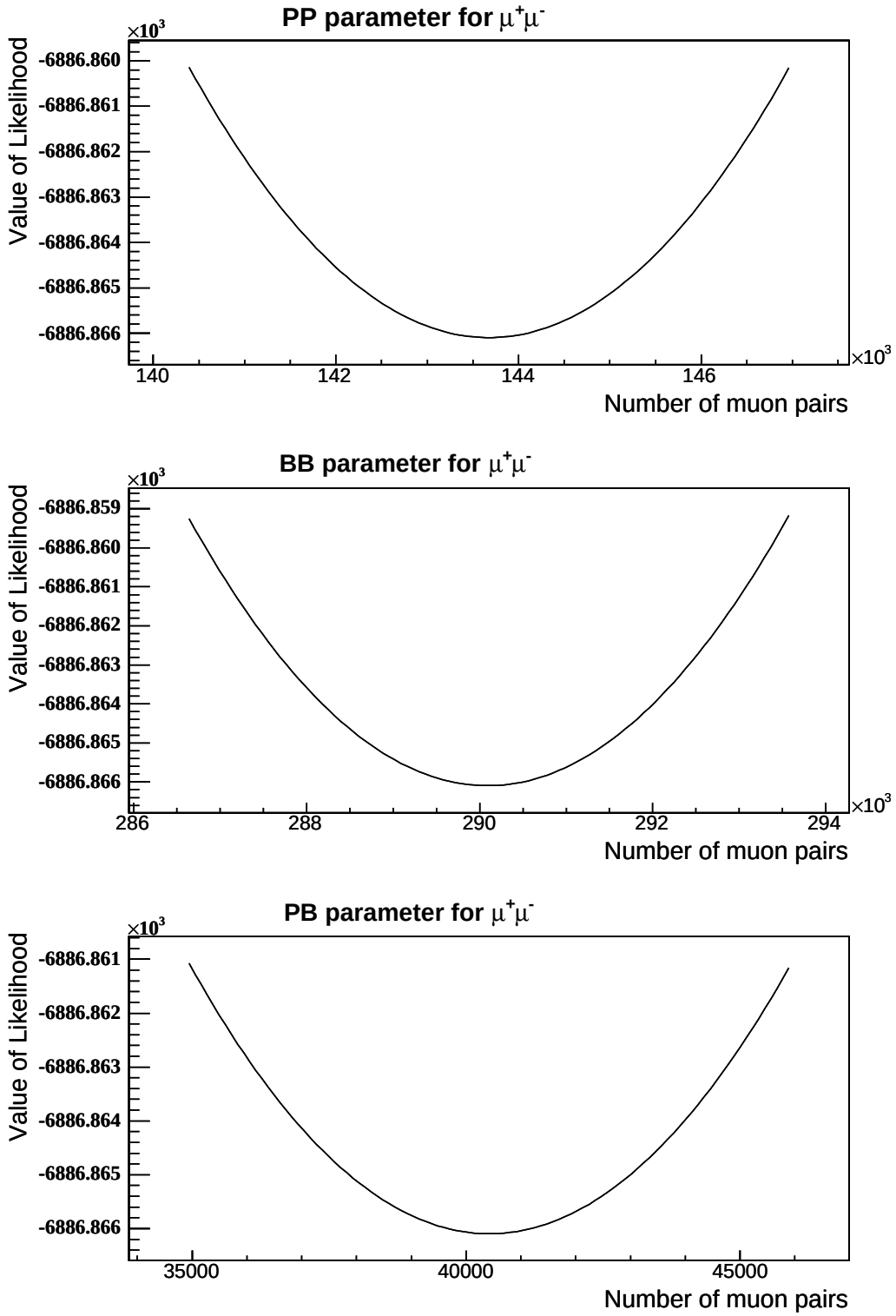

Figure 5.11: Each graph represents the $\pm 3\sigma$ scan of the free parameters after minimization for opposite sign: PP,BB, and PB. All show good parabolic minimums.

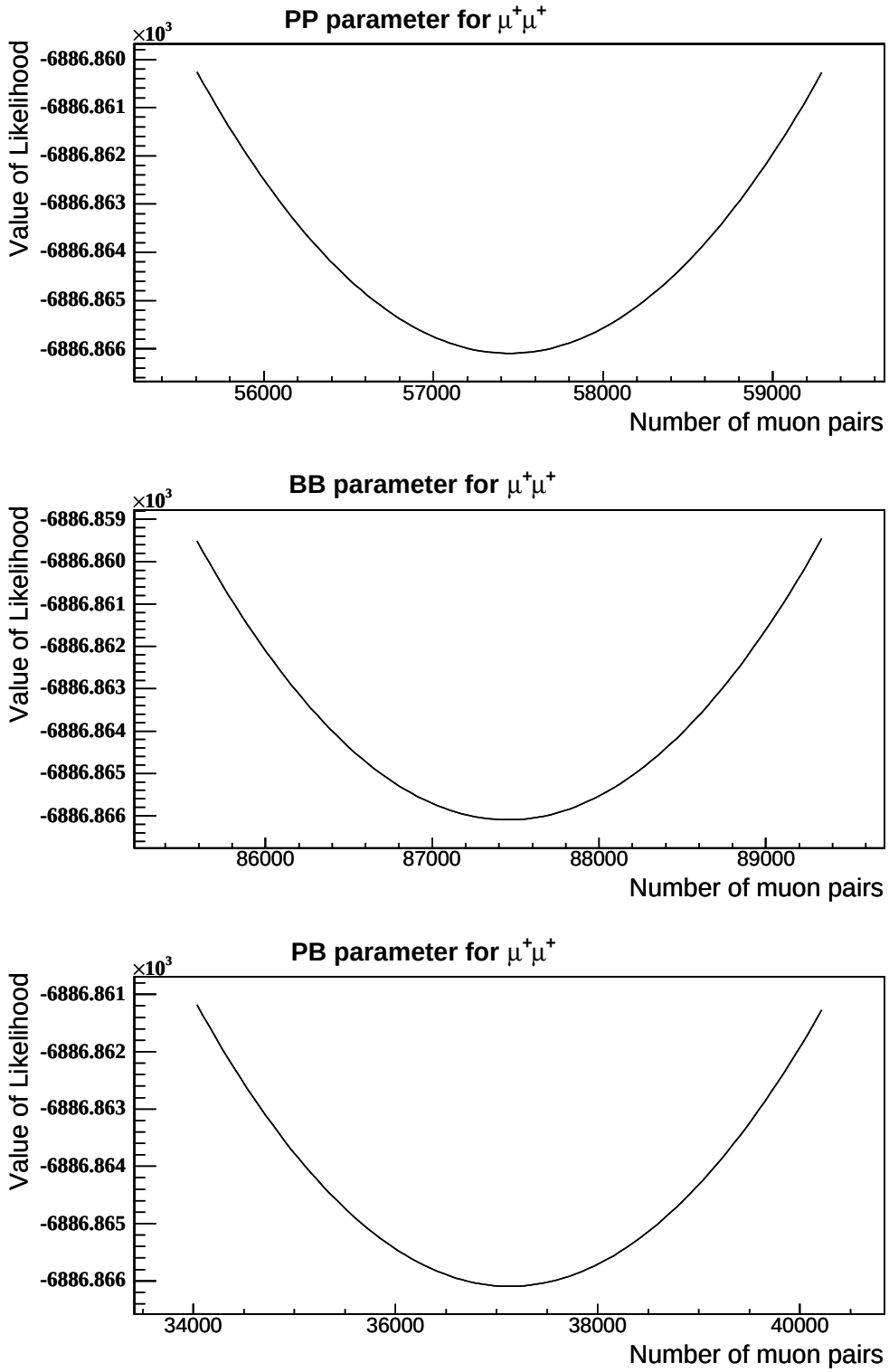

Figure 5.12: Each graph represents the $\pm 3\sigma$ scan of the free parameters after minimization for $\mu^+\mu^+$: PP,BB, and PB. All show good parabolic minimums.

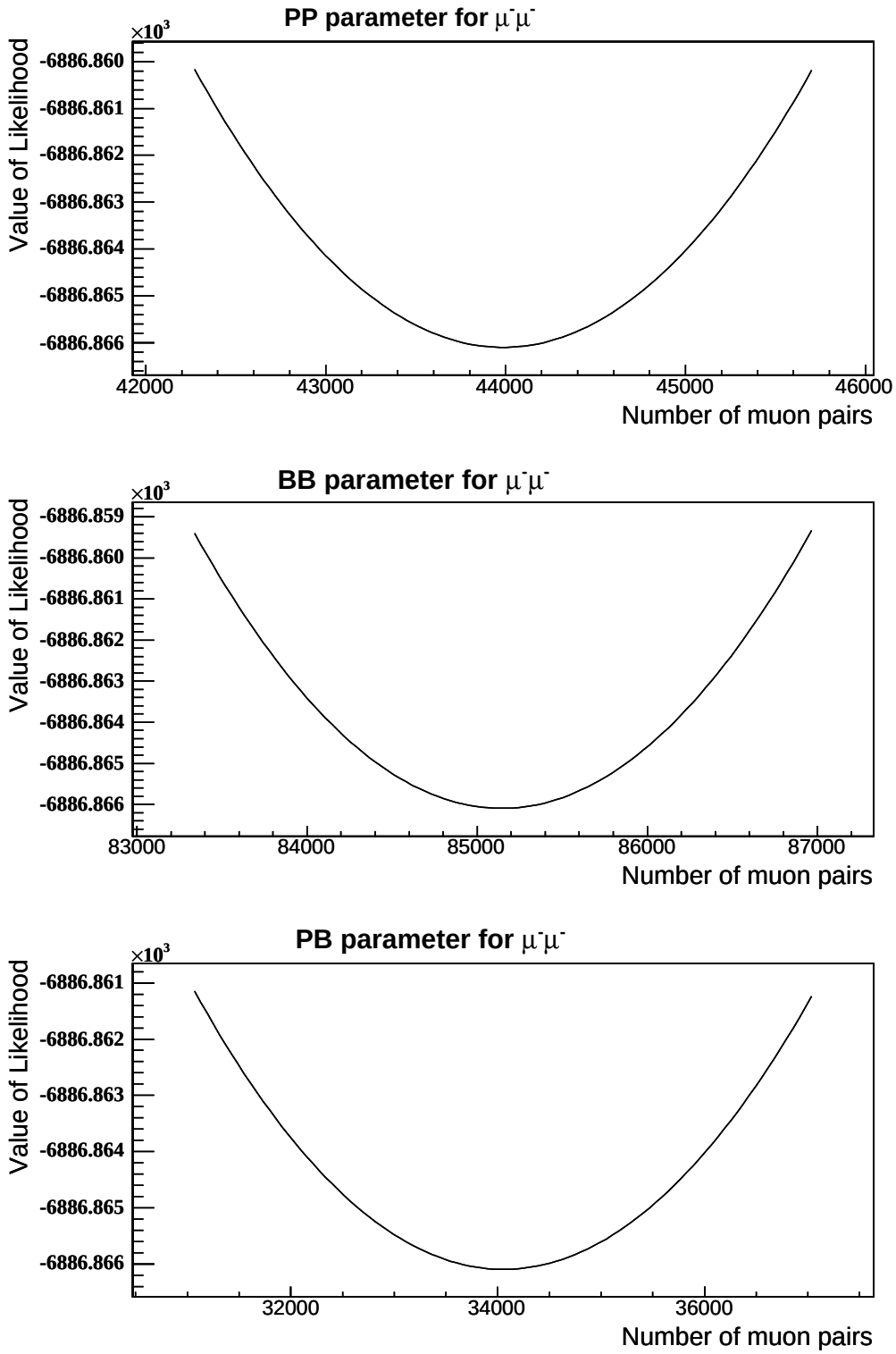

Figure 5.13: Each graph represents the $\pm 3\sigma$ scan of the free parameters after minimization for $\mu^-\mu^-$: PP,BB, and PB. All show good parabolic minimums.

5.5 Fit Results

Table 5.1 lists the percentages and errors that are the returned values of each parameter. These correspond to the templates described above as components of the $\mu^+\mu^-$, $\mu^+\mu^+$, and $\mu^-\mu^-$ signal data. All three fits are performed simultaneously. PC components are set to zero since they would otherwise return large negative values. This effect is primarily due to the overlap between CC and PC templates, and the inclusion of CC templates to the same-sign fitting.

component	opposite-sign ($\mu^+\mu^-$)	same-sign ($\mu^+\mu^+$)	same-sign ($\mu^-\mu^-$)
PP	21.29 ± 0.17	28.58 ± 0.28	25.21 ± 0.30
BB	42.90 ± 0.19	45.31 ± 0.32	50.42 ± 0.35
PB	6.78 ± 0.28	16.95 ± 0.48	17.66 ± 0.53
CC	29.03 ± 0.38	9.16 ± 0.64	6.71 ± 0.70
# BB	281,252	106,519	103,143

Table 5.1: Fit results. All numbers listed in percent. Given errors reflect statistical uncertainty only.

The total same-sign sample is around 50% $b\bar{b}$, with the majority of the remainder of the sample coming from PP sources in agreement with previous measurements of this type. The larger opposite-sign sample shows a lower $b\bar{b}$ purity, and has a more significant $c\bar{c}$ component.

From the $b\bar{b}$ fractions reported in Table 5.1, we find 106,519 ± 739 $\mu^+\mu^+$ dimuons and 103,449 ± 711 $\mu^-\mu^-$ dimuons of $b\bar{b}$ origin. These yields correspond to a raw asymmetry of

$$A_{raw} = 0.0146 \pm 0.0049 \tag{5.2}$$

Projections of the data compared to the projections of each template weighted by its fitted fraction are shown in Figures 5.14 and 5.15 for $\mu^+\mu^-$, Figures 5.16 and 5.17 for $\mu^+\mu^+$, and Figures 5.18 and 5.19 for $\mu^-\mu^-$ data. The correlation matrix is shown in Table 5.2.

5.6 Robustness of Results

Several groups of checks were performed to investigate the stability or robustness of the fitted results under variations of the template shapes and methods. Additionally, cross-checks on the asymmetry result for sub-samples of the data are examined, as is a cross-check which is independent of fitted fractions.

5.6.1 Fit Variations

Table 5.3 summarizes the BB fractions, measured asymmetry and uncertainty for the default fit and a number of variations. Also shown is a goodness-of-fit relative to the default fit. The χ^2 used for goodness-of-fit comparison is constructed from the bin-by-bin comparison of the sum of components weighted by fit parameter to the data considering only simple Gaussian errors on the data. No uncertainty for template statistics or fit parameter error is included. The ratio is used

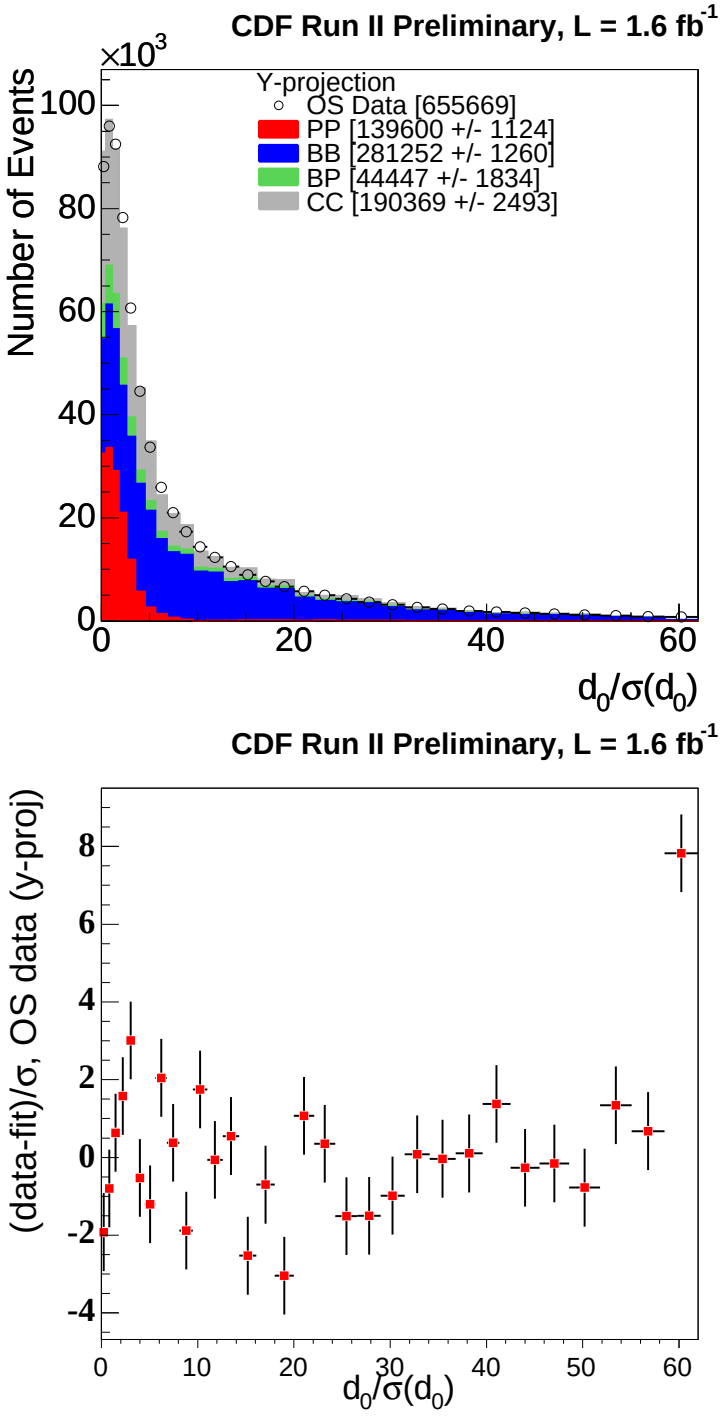

Figure 5.14: The top plot is a comparison of the total fitted component contribution compared to the data (y-projection) for $\mu^+\mu^-$ fit on a linear scale. The bottom plot is the $\mu^+\mu^-$ data minus the total fit in each projected bin divided by the uncertainty.

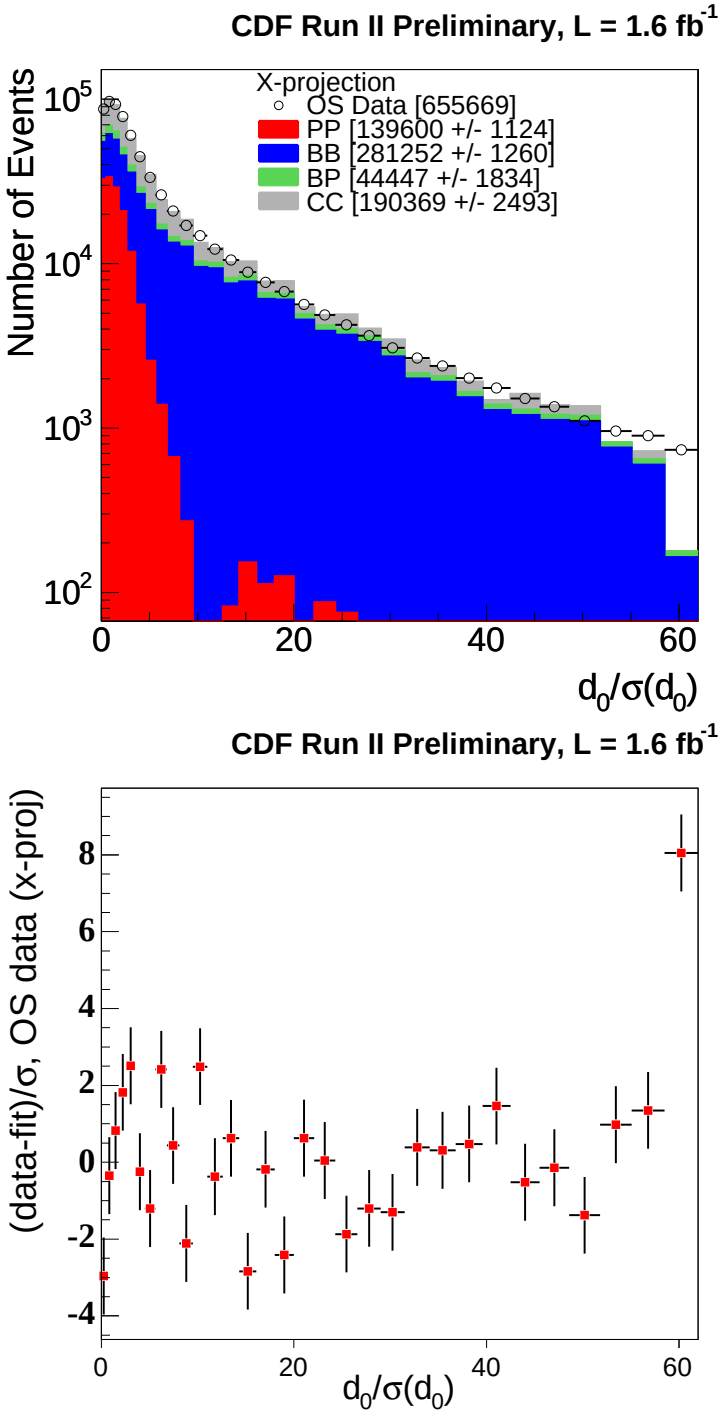

Figure 5.15: The top plot is a comparison of the total fitted component contribution compared to the data (x-projection) for $\mu^+\mu^-$ fit on a log scale. The bottom plot is the $\mu^+\mu^-$ data minus the total fit in each projected bin divided by the uncertainty.

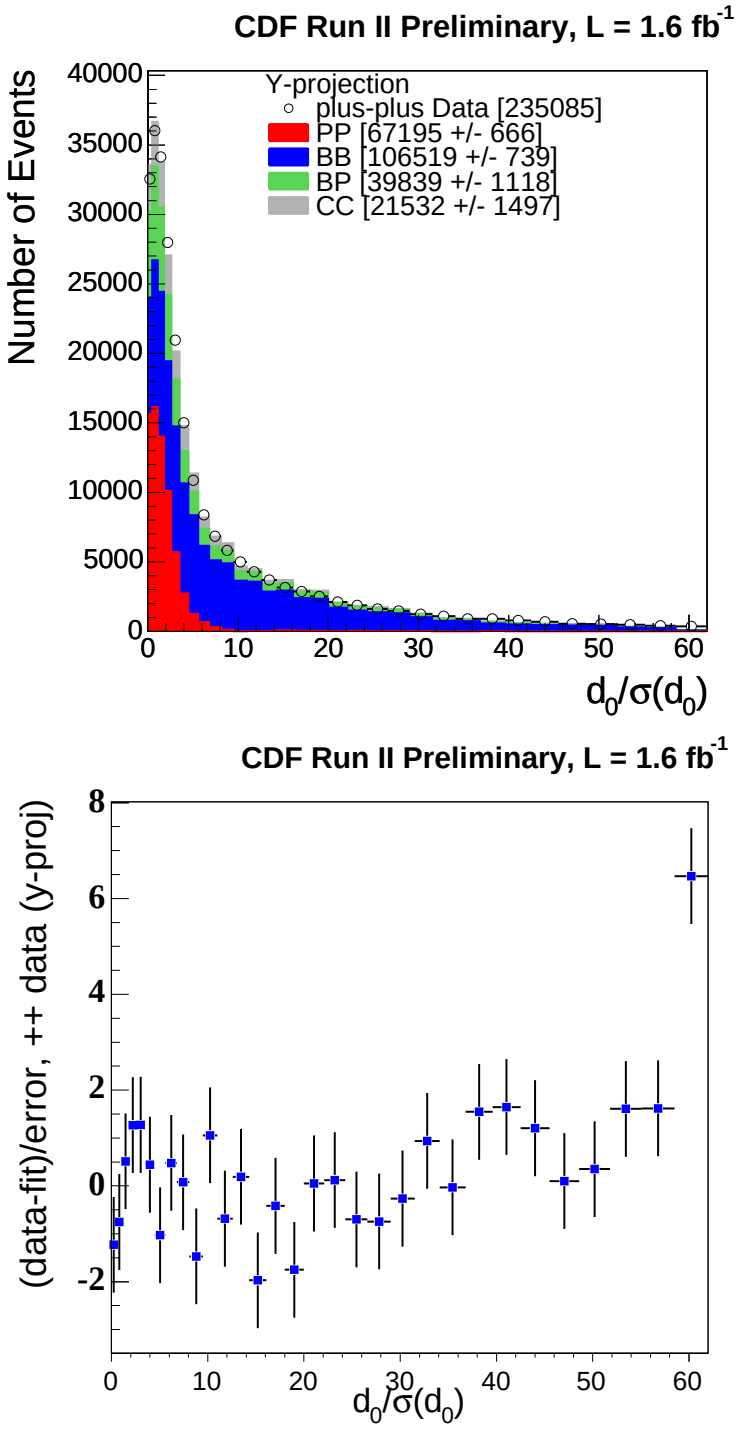

Figure 5.16: The top plot is a comparison of the total fitted component contribution compared to the data (y-projection) for $\mu^+\mu^+$ fit on a linear scale. The bottom plot is the $\mu^+\mu^+$ data minus the total fit in each projected bin divided by the uncertainty.

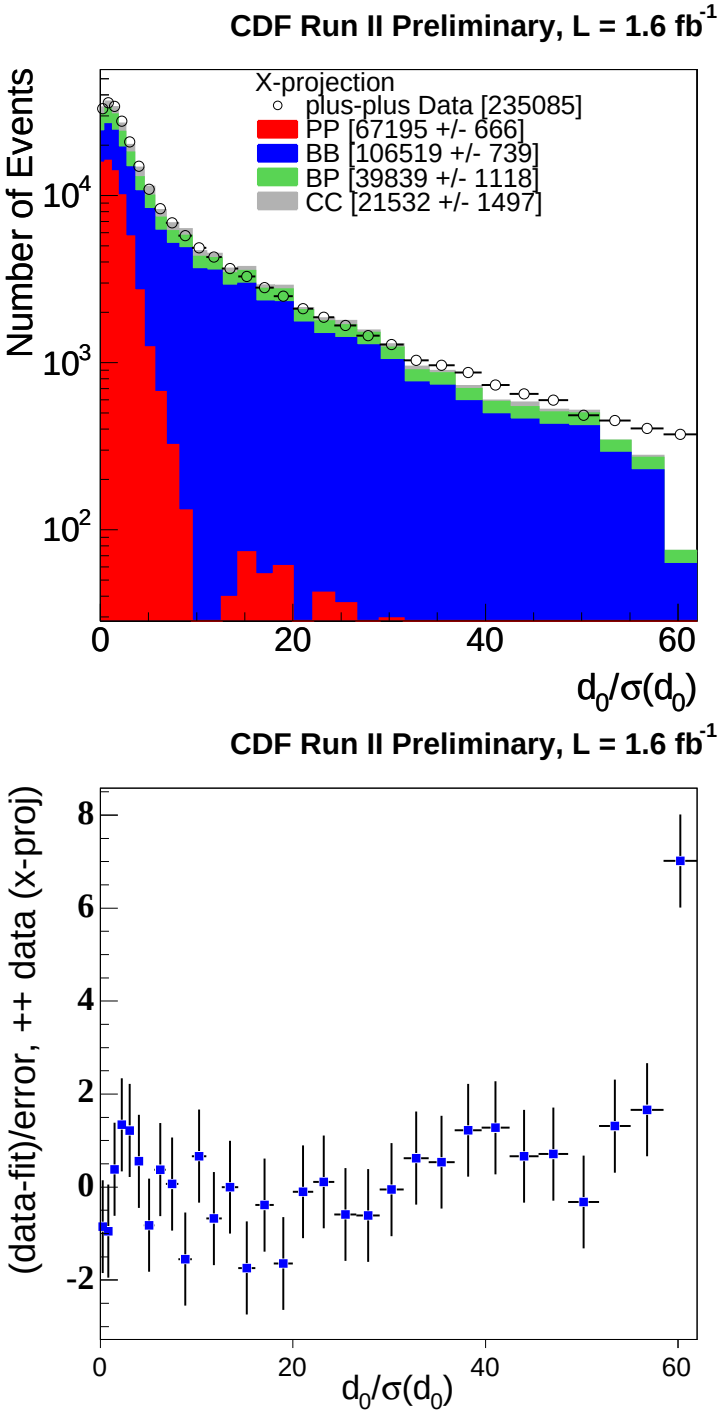

Figure 5.17: The top plot is a comparison of the total fitted component contribution compared to the data (x-projection) for $\mu^+\mu^+$ fit on a log scale. The bottom plot is the $\mu^+\mu^+$ data minus the total fit in each projected bin divided by the uncertainty.

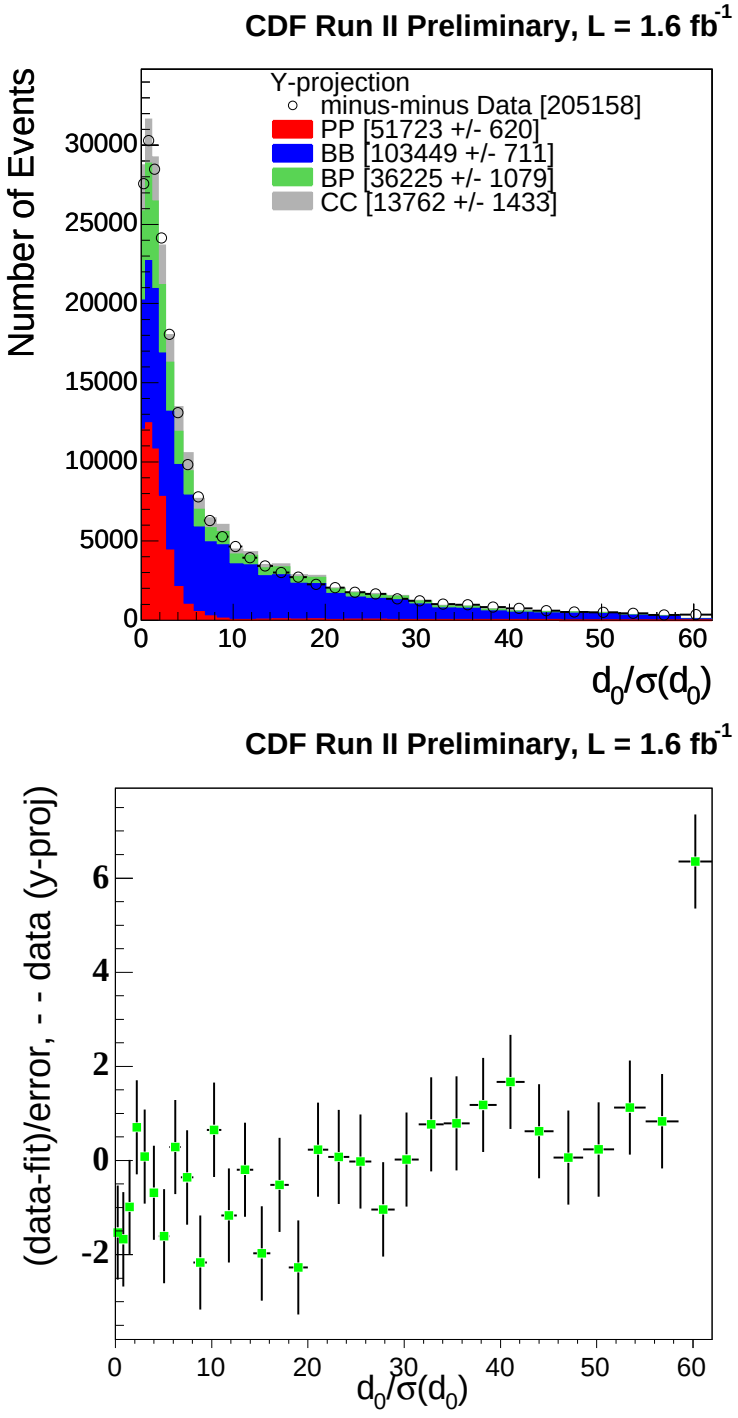

Figure 5.18: The top plot is a comparison of the total fitted component contribution compared to the data (y-projection) for $\mu^-\mu^-$ fit on a linear scale. The bottom plot is the $\mu^-\mu^-$ data minus the total fit in each projected bin divided by the uncertainty.

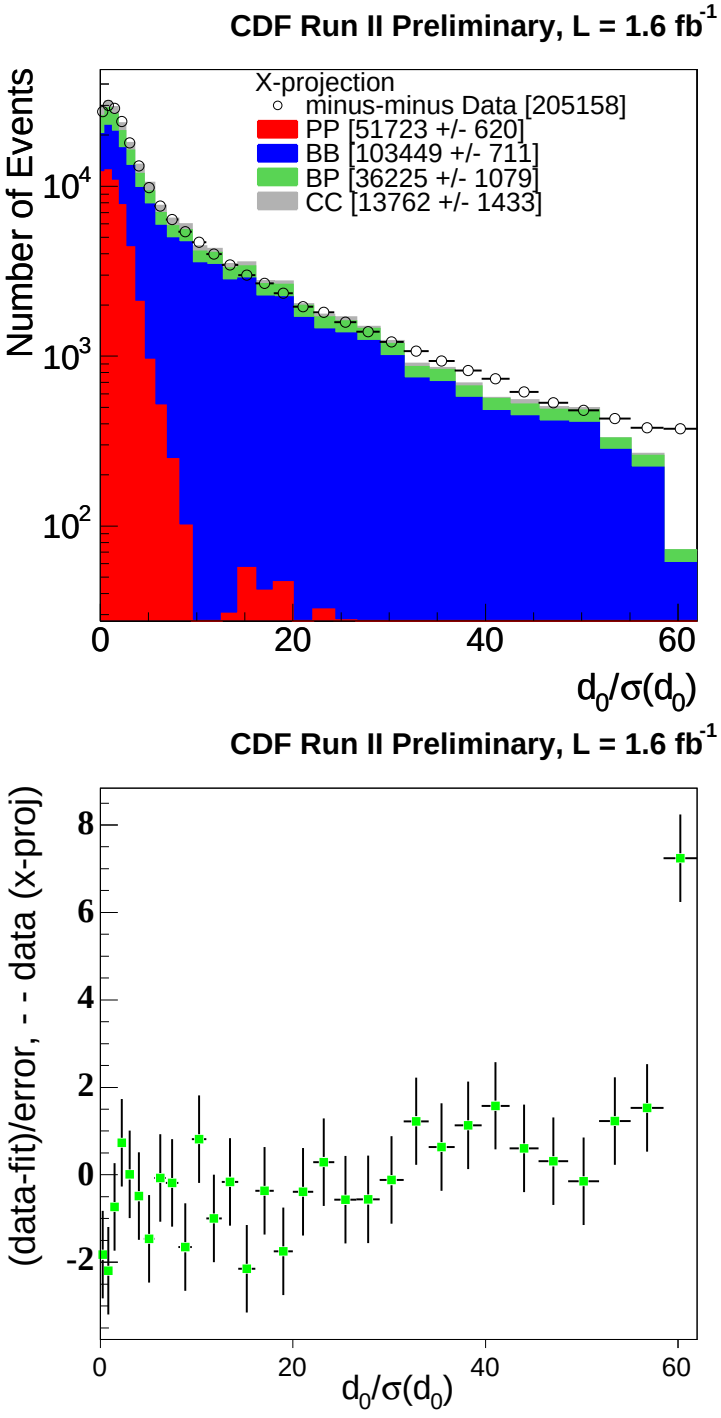

Figure 5.19: The top plot is a comparison of the total fitted component contribution compared to the data (x-projection) for $\mu^-\mu^-$ fit on a log scale. The bottom plot is the $\mu^-\mu^-$ data minus the total fit in each projected bin divided by the uncertainty.

	OS PP	OS BB	OS PB	$++PP$	$++BB$	$++PB$	$--PP$	$--BB$	$--PB$
OS BB	0.519	-	-	-	-	-	-	-	-
OS PB	-0.066	-0.311	-	-	-	-	-	-	-
OS CC	-0.678	-0.521	-0.559	-	-	-	-	-	-
$++BB$	0.000	0.000	0.000	0.500	-	-	-	-	-
$++PB$	0.000	0.000	0.000	-0.081	-0.302	-	-	-	-
$++CC$	0.000	0.000	0.000	-0.650	-0.506	-0.578	-	-	-
$--BB$	0.000	0.000	0.000	0.000	0.000	0.000	0.509	-	-
$--PB$	0.000	0.000	0.000	0.000	0.000	0.000	-0.084	-0.311	-
$--CC$	0.000	0.000	0.000	0.000	0.000	0.000	-0.645	-0.500	-0.582

Table 5.2: Correlation coefficients for each parameter in the minimization. Each data subsample is independent from the others.

to quantify the fit quality of the various cross-checks relative to the default fit and not absolute goodness of fit. The results demonstrate a consistency in the asymmetry and uncertainty even when BB fractions may be shifted.

The variations can be described as follows:

- 1-3, The PB and PC templates have a sizable overlap, so fit 1 examines them under the conditions where only PC is used instead of only the PB. In fits 2 and 3 they are constrained to be proportional to each other.
- 4-6, The dependence of the fit on the constraints described in Section 5.3 is probed, as well as the effect of discarding the last bins on each axis.
- 7,8, The PP template is the only one extracted from data. Here we examine two other prompt possibilities. MC upsilon templates in the place of data upsilons, and adding an additional prompt template comprised only of fake muons.
- 9-16, The MC generated templates are replaced with scaled templates making them longer or shorter impact parameter distributions.
- 17, All pairs in which a muon had large d_0 error are removed.
- 18, All pairs with a large $\sigma(Z_0)$ are removed.
- 19, Only pairs with 5 Silicon hits are considered.
- 20, Same-sign data from the Υ mass region is excluded from the fit.
- 21, All impact parameter errors for muons is the data are increased by 30%.
- 22, Used templates made from HERWIG Monte Carlo

These variations are treated as cross-checks, but their behavior contributes to our determination of the overall fitting systematic uncertainty.

5.6.2 Data Sub-samples

The data was divided into three cases: both muons in the forward η region, both muons in the backward η region, and one muon in each region. Another sub-sample cross-check was made to check for P_T dependence. One was also made by splitting the data into the most recent subset, and the earlier data. The asymmetries found are as follows:

- positive η region, $A = 0.00974 \pm 0.00975$
- negative η region, $A = 0.01325 \pm 0.00994$
- split η, $A = 0.01751 \pm 0.00663$
- both muons Pt < 4.2 GeV, $A = 0.00961 \pm 0.00816$
- both muons Pt > 4.2 GeV, $A = 0.01639 \pm 0.01098$

#	Fit Variation	BB fraction			A	$\delta A(stat.)$	$\frac{\chi^2}{\chi^2_{def.}}$
		OS	$\mu^+\mu^+$	$\mu^-\mu^-$			
	default	0.429	0.453	0.504	0.0146	0.0049	-
1.	$PB = 0$	0.457	0.516	0.572	0.0163	0.0045	1.20
2.	$PB = 1.5{*}PC$	0.435	0.466	0.518	0.0153	0.0047	1.02
3.	$PB = PC$	0.437	0.471	0.523	0.0154	0.0047	1.03
4.	PB SS=OS constr.	0.426	0.455	0.507	0.0147	0.0048	1.00
5.	Σ not constr. to 1	0.429	0.453	0.504	0.0146	0.0050	1.00
6.	cut last bin	0.422	0.445	0.495	0.0150	0.0050	0.89
7.	PP MC(Υ)	0.416	0.433	0.484	0.0118	0.0048	0.91
8.	PP and Fake kaons	0.395	0.385	0.429	0.0159	0.0070	1.05
9.	BB x1.10	0.365	0.389	0.435	0.0121	0.0049	0.97
10.	PB x1.10	0.420	0.442	0.493	0.0142	0.0050	0.91
11.	B x1.10	0.362	0.382	0.428	0.0115	0.0051	0.97
12.	BB x0.90	0.493	0.517	0.575	0.0150	0.0047	1.06
13.	PB x0.90	0.425	0.452	0.503	0.0152	0.0048	0.95
14.	B x0.90	0.499	0.524	0.583	0.0150	0.0048	1.09
15.	CC x1.10	0.414	0.444	0.494	0.0146	0.0051	0.90
16.	CC x0.90	0.440	0.447	0.496	0.0162	0.0047	0.97
17.	cut $\sigma(d_0) < 70\mu m$*	0.436	0.459	0.512	0.0140	0.0049	1.02
18.	cut $\delta(Z_0) < 1cm$*	0.429	0.456	0.509	0.0133	0.0050	0.96
19.	demand 5 Si hits*	0.442	0.459	0.515	0.0046	0.0067	0.67
20.	cut SS pairs in Υ region	0.429	0.448	0.498	0.0146	0.0053	0.96
21.	Assume $\sigma(d_0)$ 30% higher	0.268	0.316	0.349	0.0178	0.0062	1.79
22.	Herwig MC templates	0.457	0.478	0.530	0.0169	0.0049	1.51

* Variations 17-19 involve a change in the default selection of data. These changes are not carried into the construction of the component templates. The default templates are used in these fits.

Table 5.3: Effects of Template and Fitting Variations

- muons split in Pt, $A = 0.01812 \pm 0.00726$
- data before Sept. 2005, $A = 0.00751 \pm 0.00723$
- data after Sept. 2005, $A = 0.02039 \pm 0.00662$

5.6.3 Fit-less Asymmetry Estimate

In order to test whether the fitting technique might introduce any asymmetry, we examined the $\mu^+\mu^+$ and $\mu^-\mu^-$ data in a region that is mostly BB. The region chosen for consideration is the one where both muons have an impact parameter significance greater than 9.5σ. The BB template has 7.2% of its events in this region. While there are no prompt events, the PC, PB, CC templates have 0.1%, 0.2%, 0.8% of their events is this region respectively. This gives a rough estimate that around 88% of the events in this region are BB. Fitting the same-sign data

from 9.5σ to 62σ also returns a value $> 90\%$ BB. Counting $\mu^+\mu^+$ and $\mu^-\mu^-$ data in this region yields 16,350 pairs with an asymmetry of $A : 0.0142 \pm 0.0078$. Thus, there is in this same-sign subset which is approximately BB an asymmetry on the order of 1-2% which does not appear to be an artifact of the fitting technique.

5.6.4 Robustness Summary

Based on the fit variations, sub-samples, and fit-less asymmetry estimate, we find the fit to be stable and consistent under variation. The only fit variation which gives any significant deviation of the raw asymmetry is the one which demands two extra hits in the silicon detector. This does not raise a very great concern because of the consistency of the other checks and because this represents a significant change in selection criteria which is not modeled in the templates. The fit quality appears to be better than the default, but this effect is primarily from the loss of statistics. The higher statistical error helps to hide any underlying systematic uncertainty from the template shape. In actuality, the difference in selection criteria between the data and templates is a large source of uncertainty. The sub-samples with the largest variation are the early and later collected data. But both samples are consistent with the default fit within one standard deviation. From the asymmetry variation in Table 5.3 a systematic uncertainty of 0.002 is assessed for the template shape and fitting. This uncertainty is discussed further in Section 7.2.

Chapter 6

Asymmetry Corrections

Once the same-sign dimuon sample from BB sources is isolated, it must be corrected for any known asymmetric contributions to measure the CP asymmetry. Section 6.1 discusses an asymmetric contribution arising from hadrons in B decays which are reconstructed as muon candidates. Section 6.2 outlines the examination of any asymmetries which might be introduced by the detector systems or the CDF trigger in the process of data collection.

6.1 Fake Muons Within the BB Sample

There is a significant contribution of real $b\overline{b}$ decays where at least one of the CMUP muon candidates is not a real muon. A pion or kaon from a hadronic b decay has only a very small probability to punch-through the calorimeters and other material in front of the muon chambers. However, there are about five times more kaons and pions meeting the selection requirements produced in B decays than are muons. Thus, punch-though hadrons can be a significant background. Similarly, kaons and pions from B decays may decay in flight producing a muon with a trajectory indistinguishable from the original hadron. In both cases, these hadrons are actually of $b\overline{b}$ origin and largely irreducible as a background since their signature as a CMUP muon candidate is the same as the signature of real signal muons.

6.1.1 Hadron Charge Asymmetry

The nuclear cross section of K^+ hadrons is different than that of K^- hadrons[1]. As a result, about 50% more K^+ hadrons reach the CMP and are reconstructed as muon candidates. This asymmetric effect must be corrected for in the same-sign dimuon sample according to the probabilities that muon candidates in the fitted $\mu^+\mu^+$ and $\mu^-\mu^-$ totals are really hadrons instead of muons. The correction is made by assessing the relative probabilities that a π, μ, or K, would be produced in B meson decays, would meet the analysis kinematic requirements, and would be reconstructed as a CMUP muon candidate.

[1] The nuclear cross section of π^+ and π^- are also unequal, but this is a much smaller effect and in previous analyses has been neglected. Corrections are made for both pions and kaons in this analysis.

6.1.2 D^* Reconstruction

In order to assess an accurate value for the very low rate at which K^-, K^+, π^-, and π^+ particles are reconstructed as CMUP muon candidates, a large, very pure sample of each of the hadrons is needed. The process[2] $D^{*+} \to D^0\ \pi^+_{soft}$, $D^0 \to K^-\ \pi^+$ is collected by the CDF track trigger and can be used to identify each of the hadrons by the charge of the soft pion. About 4 million $D^{*+} \to D^0\ \pi^+_{soft}$, $D^0 \to K^-\ \pi^+$ candidate events are reconstructed from the two-track trigger data using the standard analysis selection found in [63]. Selected track pairs with an invariant mass around the D^0 mass are fitted to form a decay vertex where the fit quality is required to be $\chi^2 < 15$. Soft pion candidate tracks are then added to form a D^* vertex fit where the fit quality is required to be $\chi^2 < 40$. Events are selected with a mass difference $0.144\,\text{GeV} < m(D^*) - m(D^0) < 0.147\,\text{GeV}$, giving a fairly pure collection of $D^* \to D^0\ \pi^+_{soft}$. The mass difference distribution from the vertex fitting reconstruction before final event selection is shown in Figure 6.1.

Kaons and pions identified from the D^0 decays in this initial dataset are then required to meet selection criteria similar to the dimuon analysis selection. Tracks must have $P_T > 3.0$ GeV, at least 3 silicon $r-\phi$ hits, and the $|\eta| < 0.6$ to be considered as possible CMUP muon candidates. The candidate tracks are then examined for matching muon hits in the CMU and CMP. If these K^+, K^-, π^+, or π^- tracks are reconstructed as CMUP muon candidates then they have punched through the calorimeter into the muon chambers or have decayed in flight to a real muon and are called fakes. Figure 6.2 shows the transverse momentum distributions for each species of hadron meeting the selection requirements and Figure 6.3 shows the subsample of hadrons reconstructed as CMUP muon candidates. There are over 800,000 events in our data sample which meet these criteria for each of the hadrons.

6.1.3 Calculation of Fake Rates

In order to determine which hadrons definitely came from a D^0 decay and remove background which may alter the correct fake rates, the samples are fit for the D^0 mass between 1.80 and 1.92 GeV. A double Gaussian is used with one for the D^0 peak and one for the background in the mass region. The full sample of selected hadrons from D^* decays is fit first. Then the sample of hadrons which are reconstructed as muon candidates are fit applying the same signal shape in the full sample fit. The signal normalization and background shape and normalization are allowed to float in the second fit. Figures 6.4 - 6.7 show the D^0 fits for $D^{*+} \to D^0\ \pi^+_{soft}$, $D^0 \to K^-\ \pi^+$ events which pass the cuts and the D^0 peaks for tracks reconstructed as muon candidates for each of the four hadron species.

The fake rate is measured for each species as follows; the errors are computed using the statistical errors from the fit added in quadrature with a 5% background shape systematic:

- K^+ Fakes: 2660, Rate: 0.0061 ± 0.0003
- K^- Fakes: 1661, Rate: 0.0040 ± 0.0003
- π^+ Fakes: 946, Rate: 0.0024 ± 0.0002

[2] Both the process and its charge conjugate are meant throughout even though only one is written explicitly.

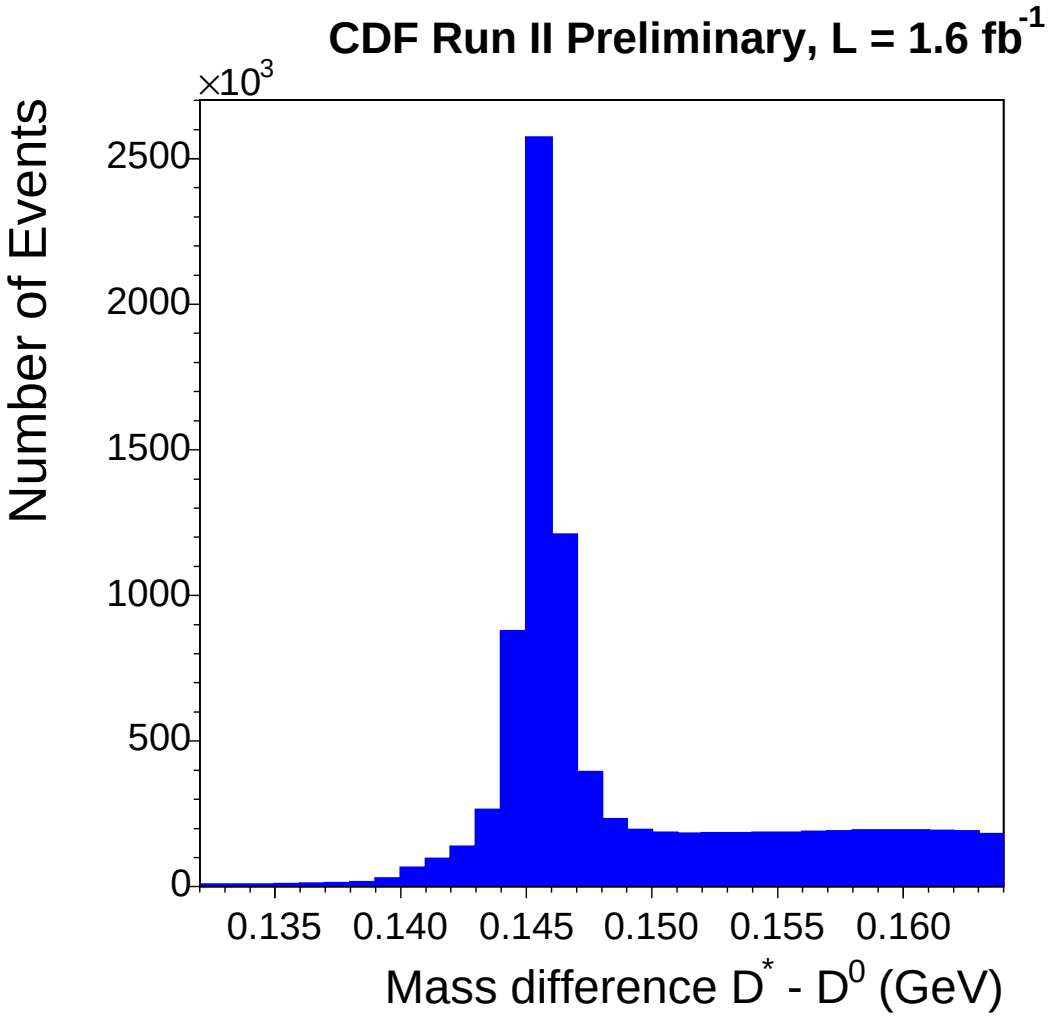

Figure 6.1: $D^* - D^0$ fitted mass difference before final event selection.

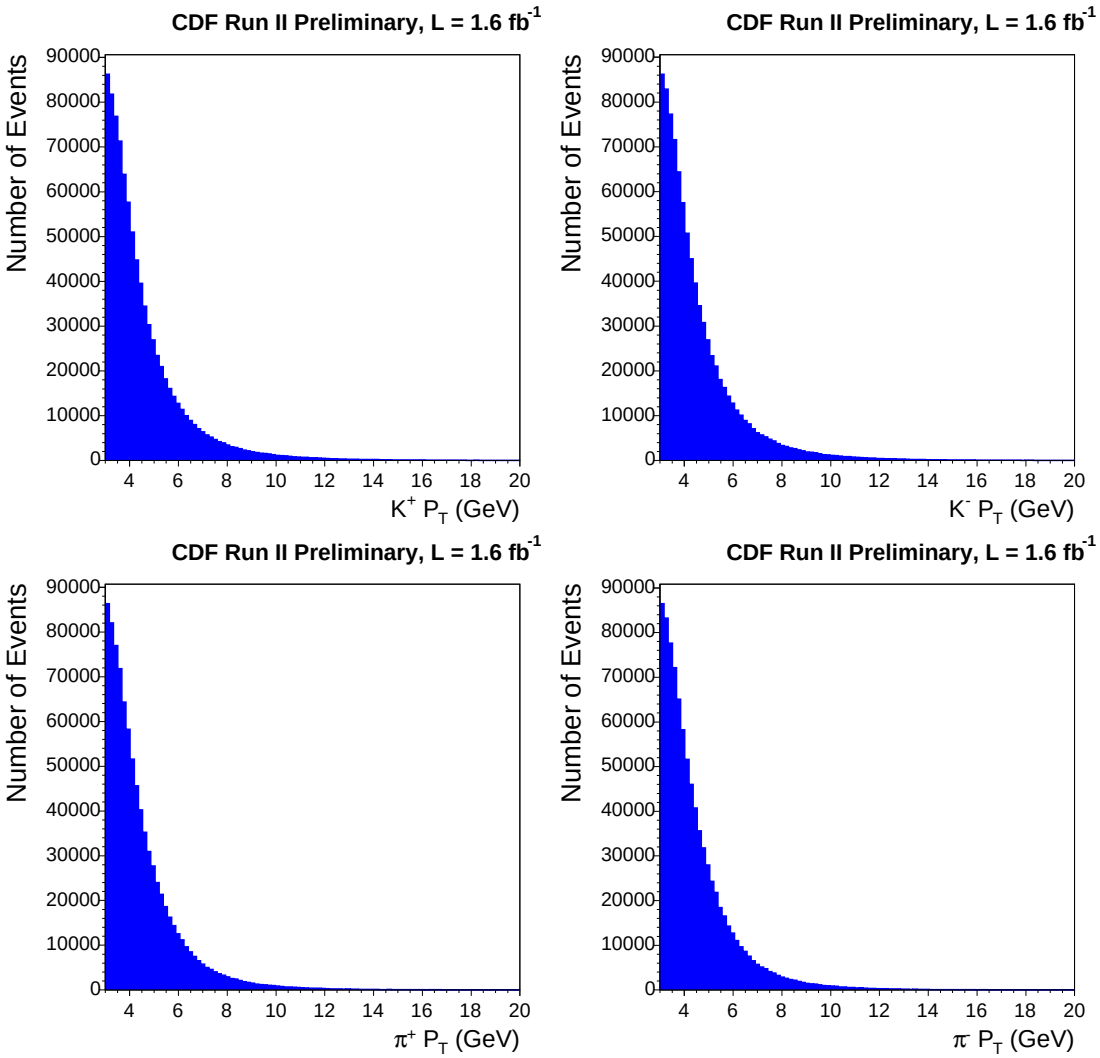

Figure 6.2: P_T distributions for (a)K^+, (b)K^-, (c)π^+ and (d)π^- before D^0 mass fitting

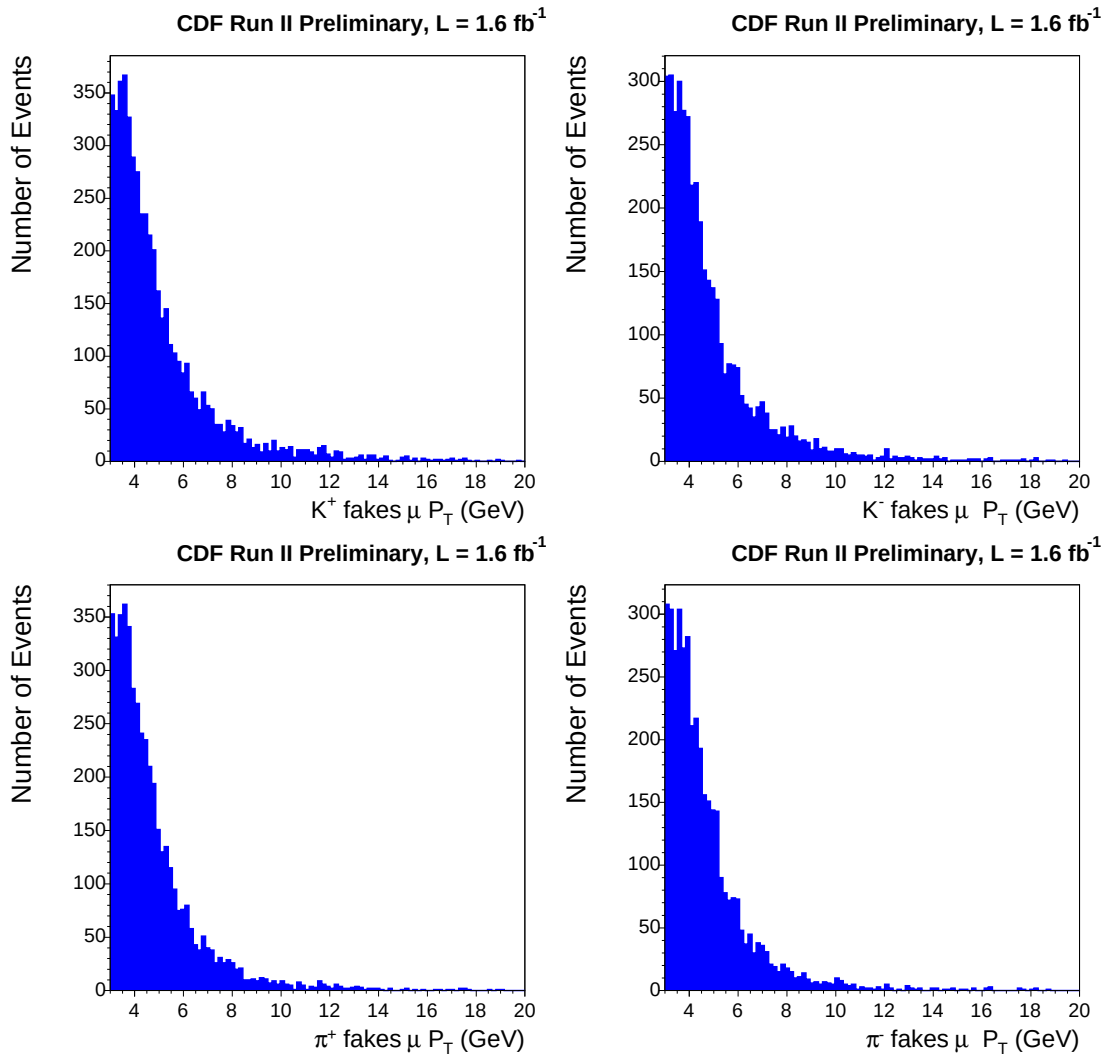

Figure 6.3: P_T distributions for (a)K^+, (b)K^-, (c)π^+ and (d)π^- which are reconstructed as muons before D^0 mass fitting

- π^- Fakes: 745, Rate: 0.0018 ± 0.0002

Examining Kinematic Dependence

Additionally, subsamples of the data were examined for strong η or P_T dependencies. Table 6.1 lists the muon fake rate for three P_T regions and five η regions. The P_T dependence suggests that the fake correction will be sensitive to differences in the muon P_T spectra between D and B decays. Therefore a comparison was made of the P_T spectrum of hadrons from D^* data used in the fake calculation to the spectrum expected from B decays in from the BB Monte Carlo sample. As seen in Figure 6.8, no significant discrepancies between the samples was found.

Subsample	Frac. of total	π^-	π^+	K^-	K^+
$P_T \leq 3.5$	0.18	0.13%	0.25%	0.34%	0.47%
$3.5 < P_T < 5.0$	0.42	0.18%	0.24%	0.41%	0.61%
$5.0 \geq P_T$	0.40	0.29%	0.34%	0.55%	0.89%
Full dataset	1.00	0.18 %	0.24%	0.40%	0.61%
$-0.6 < \eta < -0.35$	0.17	0.17%	0.22%	0.37%	0.50%
$-0.35 < \eta < -0.1$	0.26	0.32%	0.36%	0.60%	0.80%
$-0.1 < \eta < 0.1$	0.16	0.18%	0.30%	0.38%	0.63%
$0.1 < \eta < 0.35$	0.26	0.22%	0.26%	0.50%	0.81%
$0.35 < \eta < 0.60$	0.15	0.18%	0.22%	0.34%	0.47%

Table 6.1: Fake rates measured in the hadron subsamples of η and P_T. Uncertainties are on the order of .03% - .05%.

Kaon Monte Carlo Cross-check

A Monte Carlo sample of kaons was produced using FakeEvent[3] with the same P_T spectrum of CMUP muons in the dimuon analysis data. This MC sample was used as a cross check that the fake asymmetry measured in the D^* events valid in the dimuon analysis data. Figure 6.9 shows that the P_T spectrum of kaons faking CMUP muons is in good agreement with the MC generated kaons using the dimuon data P_T spectrum. We also verified that the ratio of K^+/K^- muon fake rates in the MC are in good agreement with the D^* measurement where the errors are statistical.

- Ratio of K^+/K^- fake rate from $D^* = 1.60 \pm 0.06$
- Ratio of K^+/K^- fake rate for MC $= 1.54 \pm 0.02$

These checks against the Monte Carlo and dimuon data give confidence that the fake rates measured for the hadrons in the D^* sample are accurate within their uncertainties and valid for use in the asymmetry correction. The measured fake rates are then used in combination with other normalizing probabilities described below to find the overall correction to the same-sign dimuon totals.

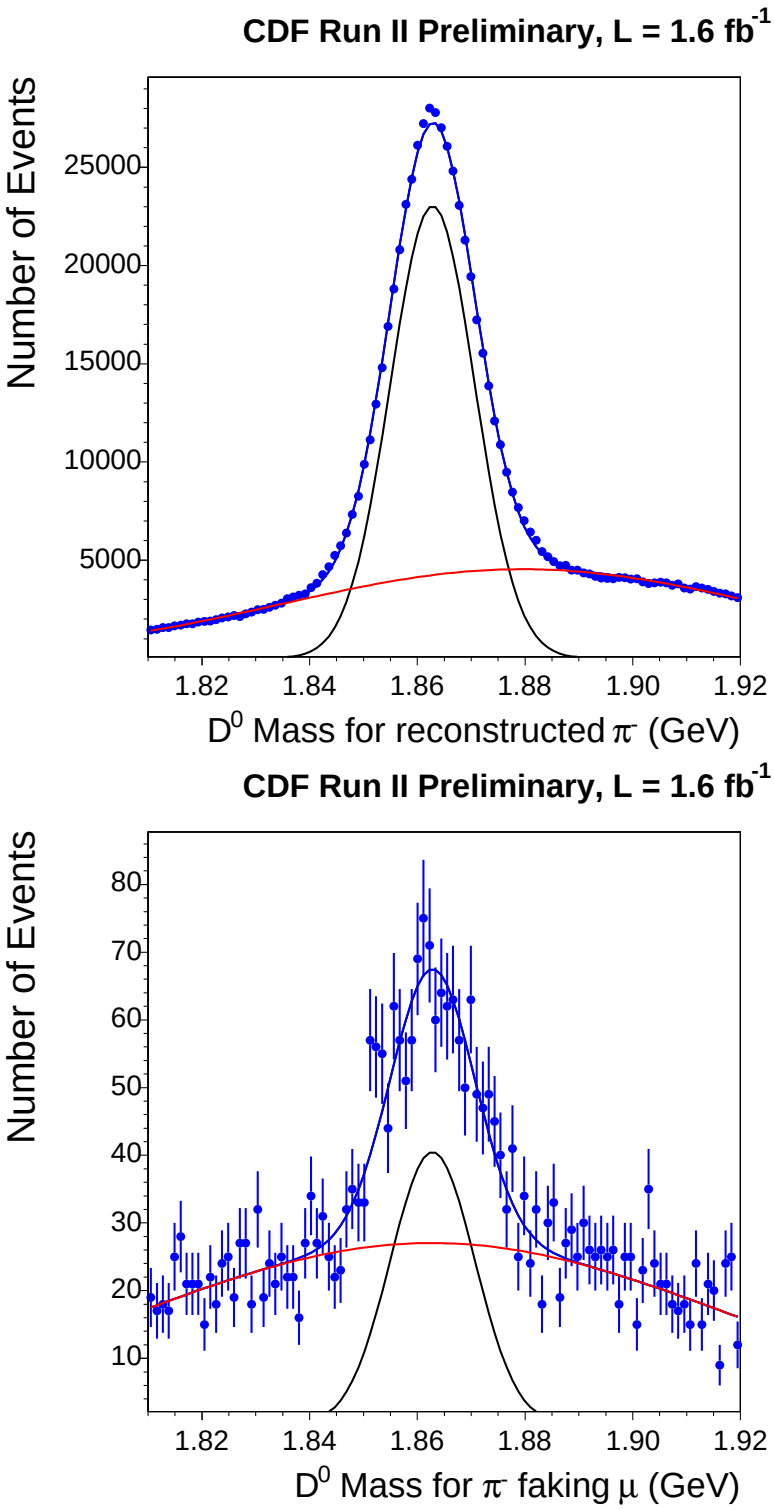

Figure 6.4: D^0 signal and background mass fits for all π^- candidates passing the dimuon analysis track selection requirements (top) and only those candidates which are reconstructed as a CMUP muon (bottom). The combined fit, and the signal and background fits are all displayed.

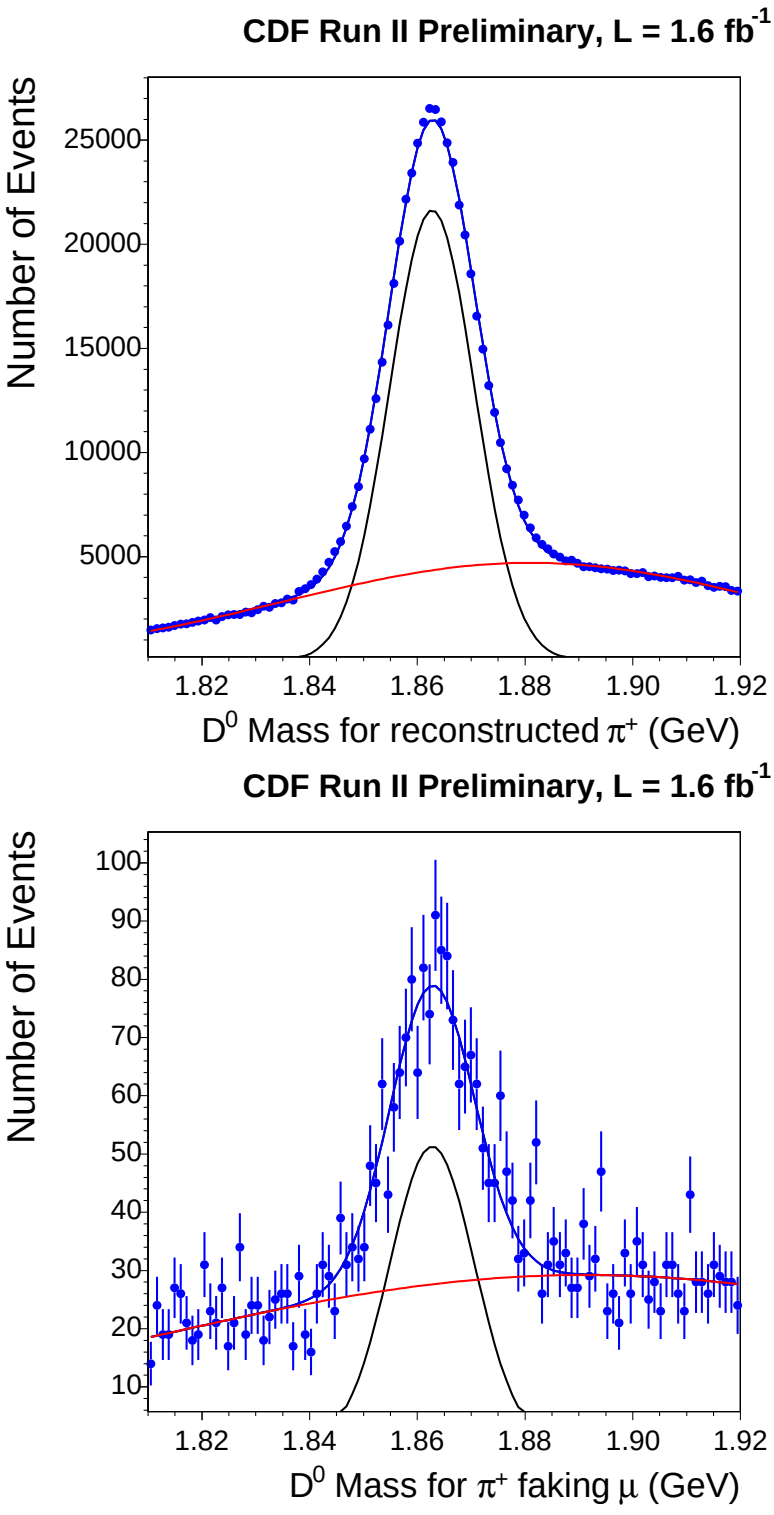

Figure 6.5: D^0 signal and background mass fits for all π^+ candidates passing the dimuon analysis track selection requirements (top) and only those candidates which are reconstructed as a CMUP muon (bottom). The combined fit, and the signal and background fits are all displayed.

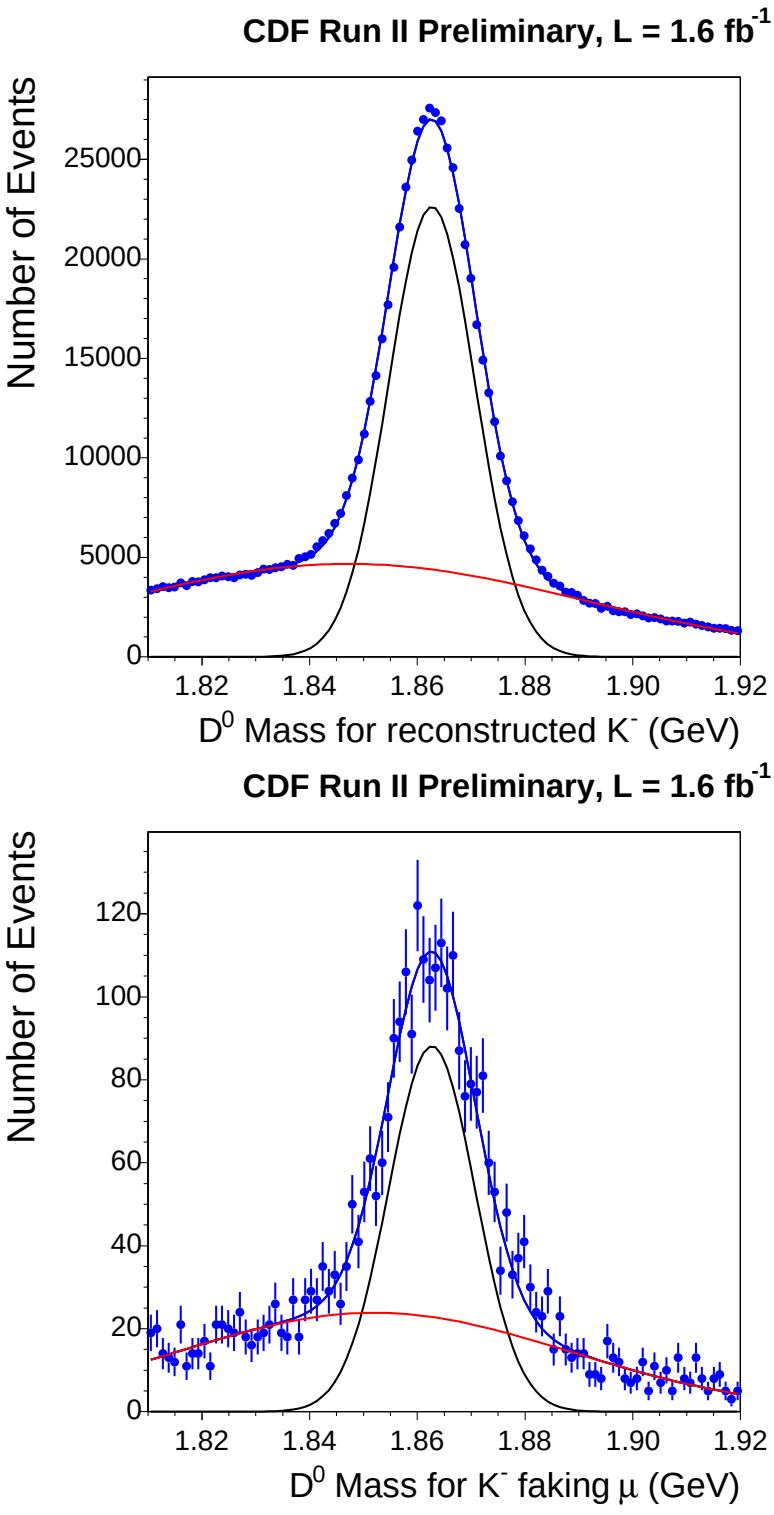

Figure 6.6: D^0 signal and background mass fits for all K^- candidates passing the dimuon analysis track selection requirements (top) and only those candidates which are reconstructed as a CMUP muon (bottom). The combined fit, and the signal and background fits are all displayed.

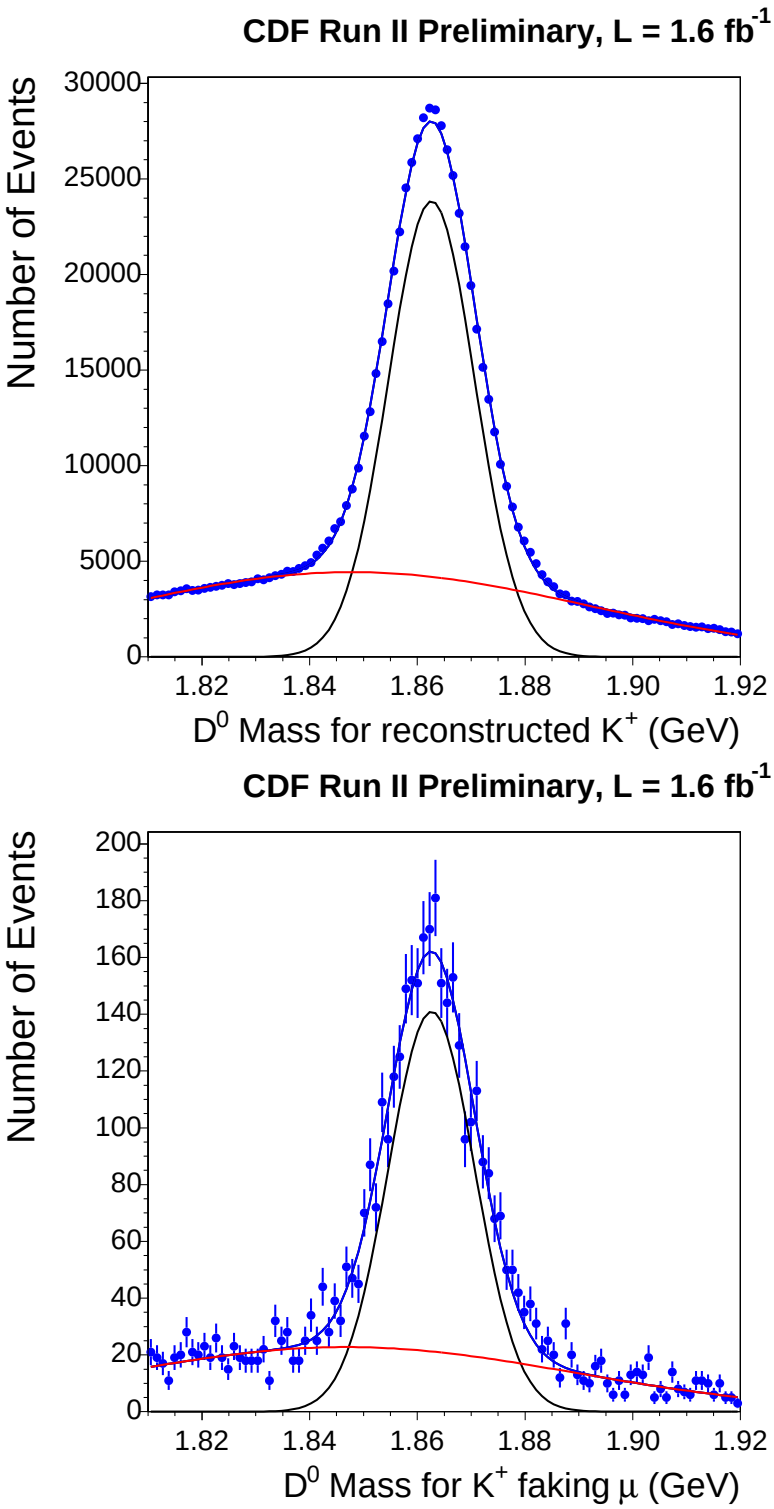

Figure 6.7: D^0 signal and background mass fits for all K^+ candidates passing the dimuon analysis track selection requirements (top) and only those candidates which are reconstructed as a CMUP muon (bottom). The combined fit, and the signal and background fits are all displayed.

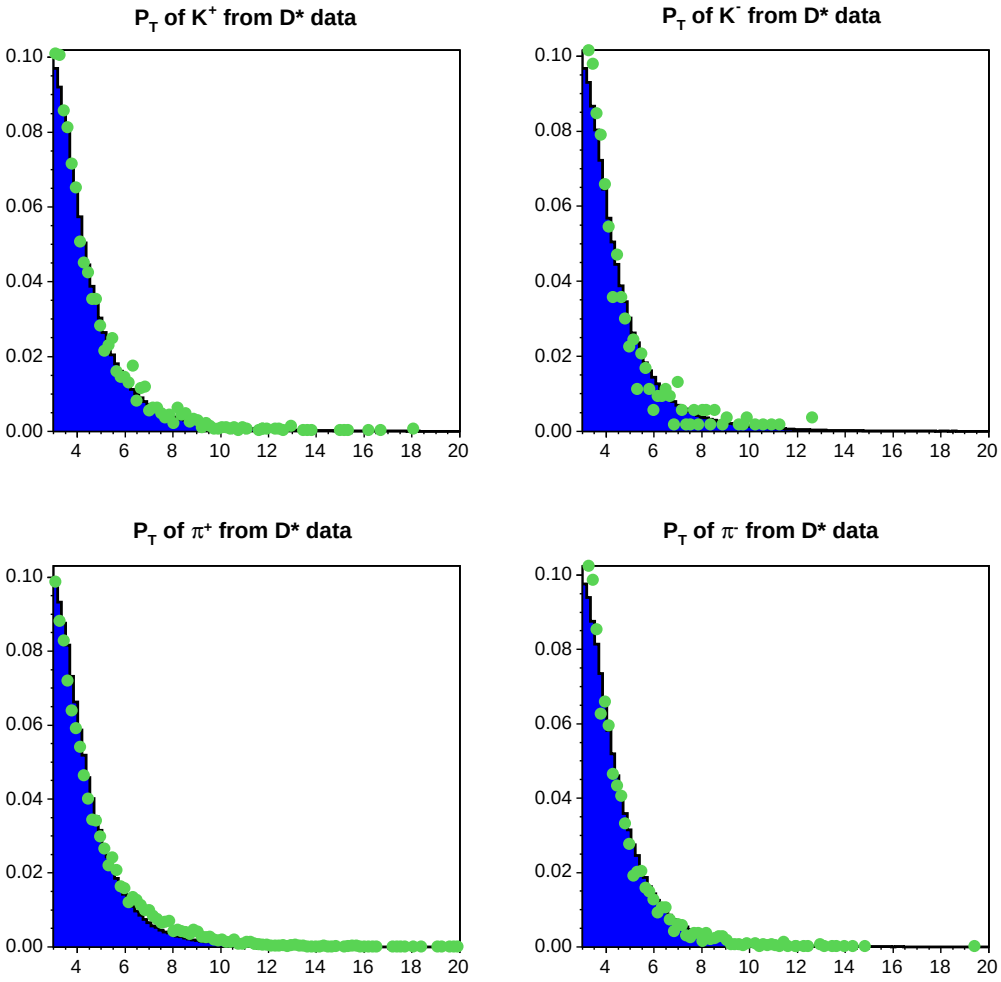

Figure 6.8: Comparison of normalized P_T distributions from pions and kaons in the D^* data meeting analysis requirements (points) and in the B Monte Carlo used for BB template (histogram).

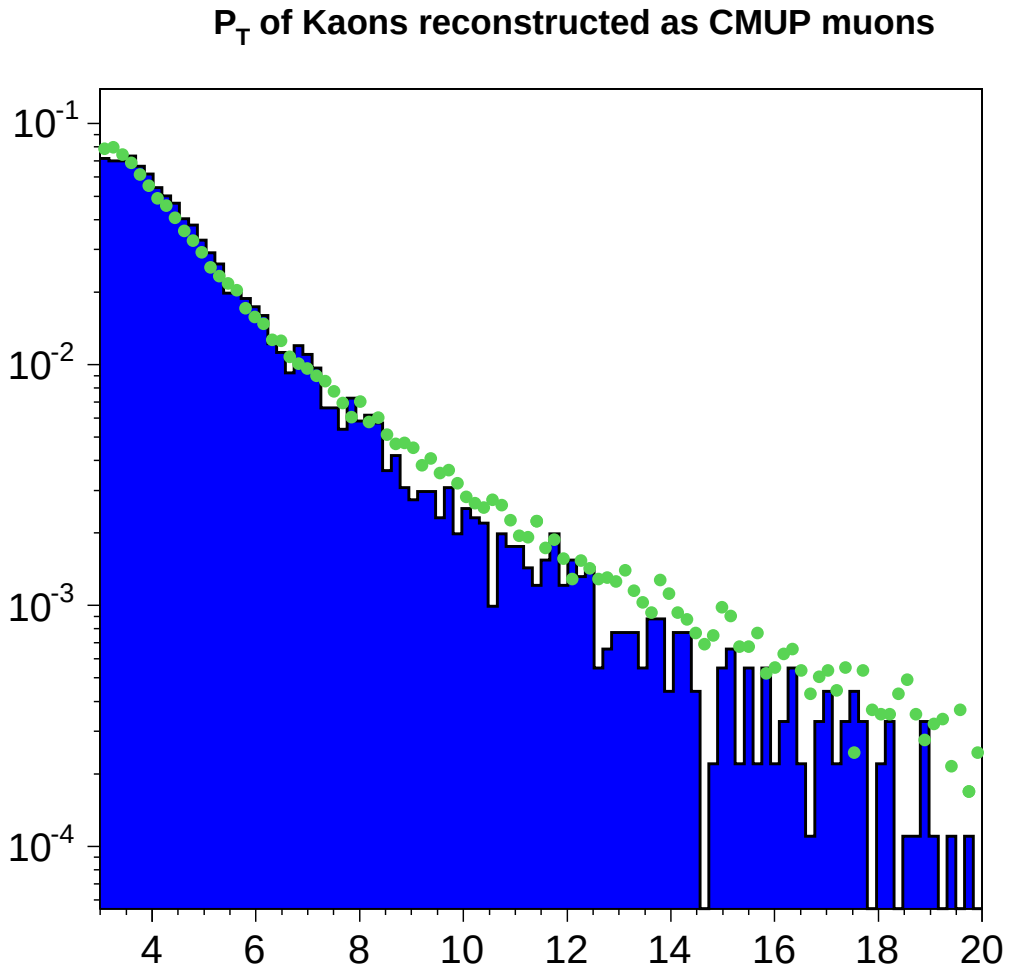

Figure 6.9: A comparison of the P_T spectrum of the kaons faking CMUP muons from the D^* data (histogram) to the MC fake kaons which use the analysis data muon P_T spectrum (points).

6.1.4 The Fake Asymmetry Correction

In order to correct the total number of dimuon pairs found for the fake contribution, the ratio of kaons and pions per muon in b decays meeting the analysis cuts is needed. The sample of MC $b\overline{b}$ pairs used to construct the BB and PB templates provides a total number of kaons, pions, and muons from b decays[4] meeting the requirements. The results found were 17,145 kaons, 38,569 pions and 10,584 muons, which correspond to ratios of

- $\frac{\pi}{\mu} = 3.64 \pm 0.04$, and
- $\frac{K}{\mu} = 1.50 \pm 0.02$,

where the errors are statistical. A 10% systematic uncertainty to each ratio of hadrons to muons is assessed because of uncertainty in the branching ratios for B hadron decays.

Additionally, for the fake rate correction only muons which are reconstructed as CMUP muon candidates with the analysis ΔX cuts are considered. This CMUP acceptance corresponds to the fake rates calculated for the hadrons as it is the probability of a real muon being reconstructed as a muon candidate, and it is 0.59 where the uncertainty is negligible.

The various probabilities and rates were combined and weighted in the following way:

- Every possibility is considered for each being reconstructed as a CMUP muon candidate(μ^+, μ^-, π^+, π^-, K^+, K^-)
- Each of the 36 cases is weighted according to 5 probabilities
  - Probability to find a track from B decays meeting the analysis kinematic requirements for both particles
    - Assessed from the ratios K/μ and π/μ in BB MC
  - Probability to be reconstructed as a CMUP muon candidate for both particles
    - Fake rates from D^* data
    - Muon rates from CMUP acceptance study
  - Charge correlation for the pair(i.e. μ^+K^- is more likely than μ^+K^+ due to BB correlation
    - We used 10% dilution (systematic uncertainty $\pm$100%)
    - Two hadron cases, a very small contribution, are assessed a 1% dilution
    - The dimuon correlation does not affect the fake rate. The number used in Table 6.2 returns the observed ratio of same-sign/opposite-sign pairs
- Each contribution is normalized so that the total number of fitted dimuons from BB is recovered

[3] FakeEvent is single particle generator. The CDF detector and trigger are also simulated for studies using FakeEvent, see Appendix D.

[4] Only decays which are not forced to a muon are used.

- 462,558 is total number used and reflects the removal of same-sign pairs in the Υ mass region

Table 6.2 summarizes all the probabilities for every case and weights the the total number of BB pairs.

Summing the total number of $\mu^+\mu^+$ and $\mu^-\mu^-$ pairs which include at least one hadron and multiplying by a factor of 1.158 to account for the inclusion of same-sign pairs in the Υ mass region being used for the asymmetry, we find a contamination of 7,382 $\mu^+\mu^+$ and 5,130 $\mu^-\mu^-$ pairs from fake muons.

6.2 Instrumentation Corrections

6.2.1 Detector Dimuon Asymmetry

The muon chamber same-sign dimuon acceptance is the greatest concern for any systematic asymmetry introduced by the detector and trigger as the CMP geometry is not axially symmetric. In order to quantify this effect, we examine Monte Carlo events produced with FakeEvent that contain muons with P_T above 2.8 GeV and have $|\eta| < 0.8$. Selecting only events with a good track that has $P_T > 3.0$ GeV and have $|\eta| < 0.6$ we measure the efficiency/acceptance for the muons being properly reconstructed as CMUP muons. The events are divided by charge and into several P_T bins of about 500,000 events each. Binomial errors are used to calculate uncertainty in the acceptance fractions. The results which are listed in Table 6.3 show a ratio of $+/-$ events that is inconsistent with 1 only for the P_T bin between 3.6 and 4.3 GeV.

A correction factor of $a_+/a_- = 1.00076 \pm 0.00036$ is be applied to account for the asymmetries introduced by the detector acceptance, efficiency, and offline reconstruction. The uncertainty on this correction is treated as a systematic uncertainty of the asymmetry measurement. The trigger asymmetry is measured separately (see Section 6.2.4).

6.2.2 Single Muon Chamber Asymmetry

For a single muon of P_T greater than 3 GeV the efficiency of the CMU and CMP muon chambers is expected to be identical for μ^+ and μ^- since the track curvature is small. As a cross-check of this assumption, we examine the CMU muon chamber hit information in the dimuon dataset. This check essentially verifies that there is no detector asymmetry which is not modeled and corrected in the MC measurement described in Section 6.2.1.

Any charge asymmetry in efficiency can be understood as a higher probability to miss hits and should then appear in the ratio of muon candidates with 3-hits to those with 4-hits. The ratios of 3-hit CMU muon stubs to 4-hit CMU muon stubs for positive muons is measured to be 0.18315 $\pm$ 0.00035 where the uncertainty is statistical. The μ^+ ratio is consistent with the measured ratio for negative muons of 0.18251 $\pm$ 0.00035. The ratio of positive to negative 3 to 4 CMU hit ratios is 1.0035 $\pm$ 0.0027, and no additional correction or systematic uncertainty is assessed.

Case	CMUP	CMUP	Corr.	P($B \to X$)	P($B \to X$)	Total
$\mu^+\mu^+$	0.5898	0.5898	0.39	0.1596	0.1596	85251
μ^+K^+	0.5898	0.00609	0.45	0.1596	0.2586	1651
$\mu^+\pi^+$	0.5898	0.00243	0.45	0.1596	0.5818	1482
$\mu^+\mu^-$	0.5898	0.5898	0.61	0.1596	0.1596	134043
μ^+K^-	0.5898	0.004	0.55	0.1596	0.2586	1325
$\mu^+\pi^-$	0.5898	0.00181	0.55	0.1596	0.5818	1349
$\mu^-\mu^+$	0.5898	0.5898	0.61	0.1596	0.1596	134043
μ^-K^+	0.5898	0.00609	0.55	0.1596	0.2586	2018
$\mu^-\pi^+$	0.5898	0.00243	0.55	0.1596	0.5818	1811
$\mu^-\mu^-$	0.5898	0.5898	0.39	0.1596	0.1596	85251
μ^-K^-	0.5898	0.004	0.45	0.1596	0.2586	1084
$\mu^-\pi^-$	0.5898	0.00181	0.45	0.1596	0.5818	1104
$K^+\mu^+$	0.00609	0.5898	0.45	0.2586	0.1596	1651
K^+K^+	0.00609	0.00609	0.49	0.2586	0.2586	30
$K^+\pi^+$	0.00609	0.00243	0.49	0.2586	0.5818	27
$K^+\mu^-$	0.00609	0.5898	0.55	0.2586	0.1596	2018
K^+K^-	0.00609	0.004	0.51	0.2586	0.2586	21
$K^+\pi^-$	0.00609	0.00181	0.51	0.2586	0.5818	21
$K^-\mu^+$	0.004	0.5898	0.55	0.2586	0.1596	1325
K^-K^+	0.004	0.00609	0.51	0.2586	0.2586	21
$K^-\pi^+$	0.004	0.00243	0.51	0.2586	0.5818	18
$K^-\mu^-$	0.004	0.5898	0.45	0.2586	0.1596	1084
K^-K^-	0.004	0.004	0.49	0.2586	0.2586	13
$K^-\pi^-$	0.004	0.00181	0.49	0.2586	0.5818	13
$\pi^+\mu^+$	0.00243	0.5898	0.45	0.5818	0.1596	1482
π^+K^+	0.00243	0.00609	0.49	0.5818	0.2586	27
$\pi^+\pi^+$	0.00243	0.00243	0.49	0.5818	0.5818	24
$\pi^+\mu^-$	0.00243	0.5898	0.55	0.5818	0.1596	1811
π^+K^-	0.00243	0.004	0.51	0.5818	0.2586	18
$\pi^+\pi^-$	0.00243	0.00181	0.51	0.5818	0.5818	19
$\pi^-\mu^+$	0.00181	0.5898	0.55	0.5818	0.1596	1349
π^-K^+	0.00181	0.00609	0.51	0.5818	0.2586	21
$\pi^-\pi^+$	0.00181	0.00243	0.51	0.5818	0.5818	19
$\pi^-\mu^-$	0.00181	0.5898	0.45	0.5818	0.1596	1104
π^-K^-	0.00181	0.004	0.49	0.5818	0.2586	13
$\pi^-\pi^-$	0.00181	0.00181	0.49	0.5818	0.5818	13

Table 6.2: Fake Muon Correction Cases and Weights

Pt bin (GeV)	pos. muons	neg. muons	Ratio +/-
tracks below 3.6	0.59057 ± 0.00031	0.59041 ± 0.00031	1.00026 ± 0.00074
tracks from 3.6 - 4.3	0.62767 ± 0.00033	0.62663 ± 0.00033	1.00167 ± 0.00074
tracks from 4.3 - 6.0	0.63426 ± 0.00030	0.63389 ± 0.00030	1.00059 ± 0.00068
tracks above 6.0	0.63888 ± 0.00032	0.63838 ± 0.00032	1.00079 ± 0.00072
whole dataset	0.62170 ± 0.00016	0.62122 ± 0.00016	1.00076 ± 0.00036

Table 6.3: Ratios of CMUP acceptance for μ^+ and μ^- over subsets of transverse momentum.

6.2.3 COT Asymmetry Checks

It is worthy of note that we are only considering triggered tracks for this measurement. Thus the XFT did find all of these tracks and any XFT trigger bias is accounted for in Section 6.2.4. An additional COT bias that does not appear in the trigger seems implausible. However, two cross-checks were explored to verify that no obvious charge bias was being introduced by COT tracking in the dimuon data.

The first check examined the PYTHIA BB Monte Carlo events for muons with P_T >3.0 GeV and $|\eta| \leq 0.6$ which were not reconstructed as tracks. There are more μ^- in these events from the forced decays, so the ratio of unreconstructed muons to reconstructed muons was used. There were 103 selected μ^+ which were not reconstructed as tracks out of 221,181 selected μ^+ corresponding to a ratio of $(4.7 \pm 0.4) \times 10^{-4}$. There were 746 selected μ^- which were not reconstructed as tracks out of 1,553,663 selected μ^- corresponding to a ratio of $(4.8 \pm 0.2) \times 10^{-4}$.

Additionally, the D^* data was used for a second cross-check. Kaon tracks passing the selection cuts for the fake rate calculation were examined by P_T binning. The ratio of K^+/K^- showed only statistical variation from 1 over the range of P_T from 3 to 20 GeV (see Figure 6.10). No additional correction or systematic uncertainty is assessed from these checks for COT asymmetry.

6.2.4 Trigger Charge Asymmetry

Using the measured values of the CDF trigger efficiency from [64], the μ^+/μ^- trigger asymmetry can be calculated. An example of the efficiency for the Level 1 trigger on CMU muons which is binned by $1/P_T$ and separated by charge from [64] is shown in Figure 6.11. Table 6.4 summarizes the differences in efficiency by P_T bins over the whole dataset used in this analysis. Each bin is weighted according to the muon P_T spectrum used in the BB template. The P_T spectrum weighting is in good agreement with the weighting according to the dimuon analysis data. The measured difference in efficiency is -0.00101 ± 0.00059. The asymmetry correction due to the single trigger efficiency is then $\epsilon_+^{trig}/\epsilon_-^{trig} = 0.99899 \pm 0.00059$.

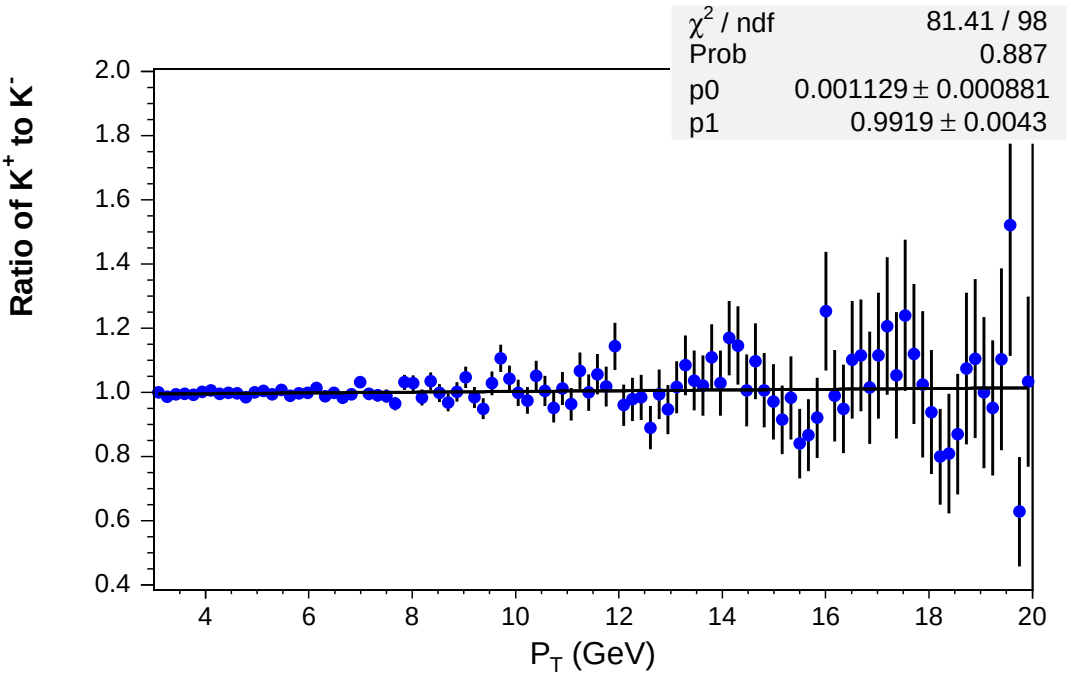

Figure 6.10: Ratio of K^+/K^- passing selection cuts from the D^* data used in the fake rate calculation.

6.3 Symmetric Background Contributions to the BB Fraction

The physics of interest for this analysis is that in which each muon is a direct decay product of a different B hadron, but both b quarks in those hadrons are correlated by pair production. Some physics contributions to the dimuon sample do not arise from this scenario but are indistinguishable from the signal process by impact parameter. However, in both cases discussed below the contributions are symmetric and thus they merely dilute rather than bias any CP asymmetry measured in the B system. The corrected A_{CP} can be adjusted for these contributions to yield a true semileptonic (SL) CP asymmetry A_{SL}.

Pt bin (GeV)	$\epsilon(\mu^+)$	$\epsilon(\mu^-)$	$\Delta(\epsilon)$	Uncert.	Weight(W)	W* $\Delta(\epsilon)$	W*Uncert.
3.0 - 3.6	.977	.977	0.000	0.001	0.28	0.00000	0.00028
3.6 - 4.0	.980	.979	-0.001	0.001	0.14	-0.00014	0.00014
4.0 - 5.3	.980	.981	0.001	0.001	0.29	0.00029	0.00029
5.3 - 7.7	.982	.985	0.003	0.002	0.18	0.00054	0.00036
7.7 - 10.0	.984	.986	0.002	0.002	0.06	0.00012	0.00012
above 10	.982	.986	0.004	0.005	0.05	0.00020	0.00025
combined	-	-	-	-	1.00	0.00101	0.00059

Table 6.4: Level 1 trigger efficiency asymmetry

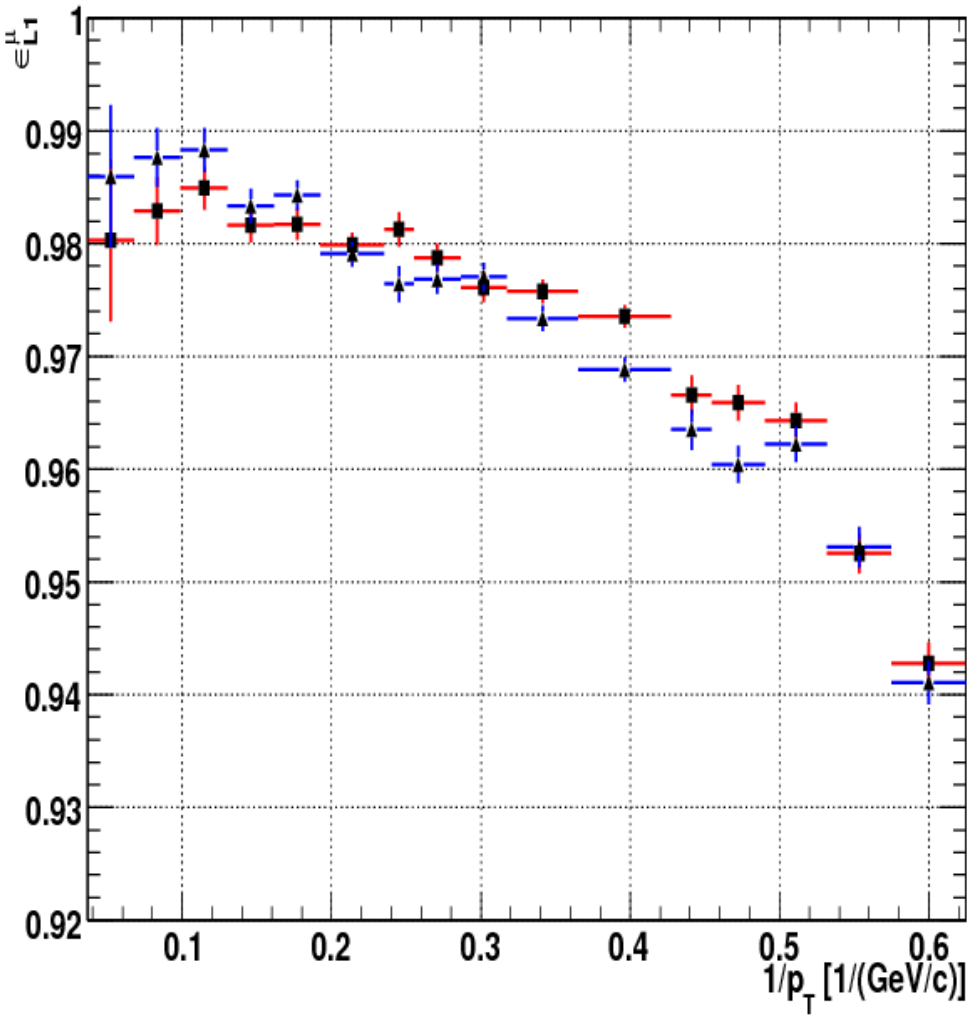

Figure 6.11: Level 1 CMU muon trigger efficiency as a function of $1/P_T$ for μ^+ (red, boxes) and μ^- (blue, triangles).

6.3.1 Multiple Heavy Flavor Production

We expect a small contribution of dimuon pairs passing the analysis cuts which fall under the classification of multiple heavy flavor production. These pairs contain a muon from a b or $\overline{b}$ decay of given charge and a second muon from another b or c quark which is not pair produced with the first b quark. There is no charge bias introduced by these pairs since it is equally likely that a second muon of the same charge as the first is positive or negative.

6.3.2 Sequential Decays

Some same-sign dimuon pairs with high impact parameter significance will include a muon sequential decay. Sequential decays are defined as muons originating from c daughters of b quarks which decayed hadronically. These pairs should not contribute asymmetrically. In order to correct the same-sign total to yield an effective asymmetry or to compare the same-sign and opposite-sign totals, the fraction of muons identified to be B decay muons that are sequential decays must be measured and removed.

Chapter 7

Asymmetry Results

This chapter describes the method of applying corrections to the measured raw asymmetry to extract physics quantities which can be compared to Standard Model predictions and combined with other measurements. The determination of systematic uncertainty to the analysis results is also summarized.

7.1 Application of Measured Corrections

The measured raw asymmetry is $A_{raw} = 0.0146 \pm 0.0049$ before applying any corrections and considering only statistical uncertainty. The asymmetry corrected for instrumentation bias is related to the raw asymmetry in the following way:

$$A_{corr} = \frac{N^{++}_{true} - N^{--}_{true}}{N^{++}_{true} + N^{--}_{true}}, \quad A_{raw} = \frac{N^{++}_{obs} - N^{--}_{obs}}{N^{++}_{obs} + N^{--}_{obs}} \tag{7.1}$$

where the raw asymmetry is constructed of observed number of muon candidate pairs N_{obs}, and the corrected asymmetry of true number of pairs, N_{true}. The true number takes into account the loss of real same-sign muon pairs from B hadron decays because of trigger efficiency or detector acceptance which is less than 100%. With two uncorrelated muon candidates in each pair, the true number of same-sign dimuons is related to the observed number by the squared corrections for both the single muon trigger efficiency and the detector acceptance for a single muon. In Equation 7.2, ϵ is used to represent the product of both correction factors.

$$\begin{aligned} N^{++}_{true} &= N^{++}_{pass} + N^{++}_{fail} \\ N^{++}_{obs} &= N^{++}_{true} \times \epsilon^2_+ \\ N^{++}_{fail} &= N^{++}_{true} \times 2\epsilon_+(1-\epsilon_+) + N^{++}_{true} \times (1-\epsilon_+)^2 \end{aligned} \tag{7.2}$$

The relationships found in equation 7.2 also holds true for $N(\mu^-\mu^-)$, but the correction factor $\epsilon_+ \neq \epsilon_-$. Since N_{obs} is the observed number of dimuons from fitting the data,

$$A_{corr} = \frac{N_{obs}^{++}(\frac{1}{\epsilon_+^2}) - N_{obs}^{--}(\frac{1}{\epsilon_-^2})}{N_{obs}^{++}(\frac{1}{\epsilon_+^2}) + N_{obs}^{--}(\frac{1}{\epsilon_-^2})} = \frac{N_{obs}^{++} - N_{obs}^{--}(\frac{\epsilon_+}{\epsilon_-})^2}{N_{obs}^{++} + N_{obs}^{--}(\frac{\epsilon_+}{\epsilon_-})^2} \tag{7.3}$$

Using $(a_+/a_-)^2 = 1.0015 \pm 0.0007$ from section 6.2.1, and $(\epsilon_+^{trig}/\epsilon_-^{trig})^2 = 0.9980 \pm 0.0012$ from section 6.2.4, we apply the correction $(\epsilon_+/\epsilon_-)^2 = 0.9995 \pm 0.0014$ to equation 7.3. Using the values of N_{obs} before they have been corrected for fake muons we find $A_{corr} = 0.0149 \pm 0.0049$ where the uncertainty is still only the statistical uncertainty.

Finally, the true BB asymmetry must be corrected for the physical asymmetry introduced by hadrons which are reconstructed as muon candidates. The corrected asymmetry, after removing these hadrons from B decays as described in Section 6.1, is measured to be $A_{BB} = 0.0044 \pm 0.0049$. This asymmetry for real muons from all $b\overline{b}$ events and is still not corrected for the symmetric backgrounds described in Section 6.3.

7.2 Systematic Error Evaluation

Systematic uncertainty from fake asymmetry correction is measured by varying each hadron fake rate - K^+, K^-, π^+, and π^- - by 1σ to find δA for the correction. Additionally, the ratios of hadrons to muons and charge correlation each are varied by 1σ and all δAs are summed in quadrature. The total measured systematic uncertainty from the fake correction is $\delta A = 0.0028$.

Systematic uncertainty for the single muon trigger efficiency and detector acceptance corrections are evaluated as twice the uncertainty on each correction, since each is squared for dimuon pairs. The systematic uncertainty of the asymmetry due to the trigger efficiency is $\delta A = 0.0012$ as derived in Section 6.2.4. It is $\delta A = 0.0007$ for the detector acceptance as described in Section 6.2.1.

To assess a systematic uncertainty from possible bias in the fitting technique, we look at the variation in raw asymmetry from the robustness checks listed in Table 5.3. A significant majority of the checks returns a value for the asymmetry that is within 0.2% of the nominal value. While not an exhaustive check, the variations shown in Table 5.3 represent a variety of possible fitting configurations in all of the relevant quantities. Therefore, we estimate a fitting uncertainty based on the fit variations of 0.2%.

Table 7.1: Systematic Uncertainties

Source of Uncertainty	δA
Fake muon corr.	0.0028
Trigger efficiency corr.	0.0012
Detector acceptance corr.	0.0007
Fitting Uncertainty	0.0020
Total	0.0037

7.3 Extraction of Physics Quantities

The semileptonic asymmetry is obtained by removing the contribution of CP symmetric backgrounds described in Section 6.3. We measure the fraction of these backgrounds to be $f_{WS} = 0.102 \pm 0.015$, where this fraction is all wrong-sign contributions of a single muon B decay. This includes multiple heavy flavor production, but is primarily sequential decays. There is also a small contribution of right-sign sequential decays from the case where the virtual W from the $b \to c$ transition decays hadronically to charm rather than semimuonically and the charm decays to a muon. For dimuon events we find the following fractions:

- $f_{DD} = 0.768 \pm 0.019$, two direct muon decays
- $f_{DS} = 0.183 \pm 0.027$, one sequential decay resulting in a wrong-sign muon
- $f_{DS}^{RS} = 0.039 \pm 0.004$, one direct decay, and one sequential decay resulting in a right-sign muon
- $f_{SS} = 0.010 \pm 0.002$, two sequential decays resulting in two wrong-sign muons

Thus $N(\mu^+\mu^+)$ and $N(\mu^-\mu^-)$ can be defined as follows where χ is the mixing probability for B, $\overline{\chi}$ is the mixing probability for $\overline{B}$, and $\chi_0 = \frac{1}{2}(\chi + \overline{\chi})$:

$$\begin{aligned} N(\mu^+\mu^+) &= N_{BB}\{(f_{DD} + f_{DS}^{RS})\chi(1-\chi_0) + \frac{1}{2}f_{DS}[1 - 2\chi_0(1-\chi_0)] + f_{SS}\overline{\chi}(1-\chi_0)\} \\ N(\mu^-\mu^-) &= N_{BB}\{(f_{DD} + f_{DS}^{RS})\overline{\chi}(1-\chi_0) + \frac{1}{2}f_{DS}[1 - 2\chi_0(1-\chi_0)] + f_{SS}\chi(1-\chi_0)\} \end{aligned} \quad (7.4)$$

$$A_{BB} = \frac{N(\mu^+\mu^+) - N(\mu^-\mu^-)}{N(\mu^+\mu^+) + N(\mu^-\mu^-)} = \frac{(f_{DD} + f_{DS}^{RS} - f_{SS})(\chi - \overline{\chi})(1-\chi_0)}{(f_{DD} + f_{DS}^{RS} + f_{SS})(\chi + \overline{\chi}) + f_{DS}[1 - 2\chi_0(1-\chi_0)]} \quad (7.5)$$

We now use the definition of χ_0 and divide through by $2\chi_0(1-\chi_0)$ to obtain the following relation between the physics asymmetry from CP violation in mixing, $(\chi - \overline{\chi})/(\chi + \overline{\chi})$, and A_{BB}:

$$A_{BB} = \frac{(f_{DD} + f_{DS}^{RS} - f_{SS}) \times [\frac{\chi - \overline{\chi}}{\chi + \overline{\chi}}]}{f_{DD} + f_{DS}^{RS} + f_{SS} + f_{DS}\frac{1 - 2\chi_0(1-\chi_0)}{2\chi_0(1-\chi_0)}} \quad (7.6)$$

Using the world average $\chi_0 = 0.127 \pm 0.006$ [10], and the fractions measured above we find

$$A_{SL}^{\mu\mu} = \frac{(\chi - \overline{\chi})}{(\chi + \overline{\chi})} = (1.83 \pm 0.15) \times A_{BB} \quad (7.7)$$

which yields

$$A_{SL}^{\mu\mu} = 0.0080 \pm 0.0090(stat) \pm 0.0068(syst). \tag{7.8}$$

The world's best measurement of the same-sign dimuon charge asymmetry was made by $D0$, $A_{SL}^{\mu\mu} = -0.0053 \pm 0.0025(stat) \pm 0.0018(syst)$ [54].

We can also constrain the B_s contribution to $A_{SL}^{\mu\mu}$ by following the strategy outlined in [32]. Using the B factory measurements of $A_{SL}^{d} = -0.0005 \pm 0.0056$, and world averages of the quantities $f_s Z_s = 0.110 \pm 0.012$ and $f_d Z_d = 0.150 \pm 0.004$, we can extract A_{SL}^{s} from Equation 7.9[1].

$$A_{SL}^{\mu\mu} = \frac{(f_d Z_d) A_{SL}^{d} + (f_s Z_s) A_{SL}^{s}}{f_d Z_d + f_s Z_s} \tag{7.9}$$

We find the following, where the systematic error is our measured systematic and there is an additional contribution to the uncertainty that arises from the inputs f_s, Z_s, f_d, Z_d, and A_{SL}^{d}.

$$A_{SL}^{s} = 0.020 \pm 0.021(stat) \pm 0.016(syst) \pm 0.009(inputs), \tag{7.10}$$

We can then use the relation [34]:

$$A_{SL}^{s} = \frac{\Delta\Gamma_s}{\Delta m_s} \tan\phi_s \tag{7.11}$$

to extract an allowed contour in the (ϕ_s,$\Delta\Gamma_s$) plane. Using $\Delta M_s = 17.8 \pm 0.1\,\mathrm{ps}^{-1}$, the 68% contour is shown in Fig. 7.1. This result can be combined with CDF measurements of $\Delta\Gamma_s$ as a constraint to extract an allowed range for ϕ_s. The most current CDF $\Delta\Gamma_s$ measurement with ϕ_s fixed to 0 in $B_s \to J/\Psi\phi$ decays is [66]

$$\Delta\Gamma_s = 0.08 \pm 0.06. \tag{7.12}$$

7.4 Result Synopsis

We have measured the same-sign dimuon asymmetry from decays of $b\bar{b}$ production using pairs of muon candidates with $P_T > 3$ GeV and an invariant mass of at least 5 GeV. Muon candidate pairs meeting selection requirements were fitted to signal and background templates to determine the fraction of BB hadron pairs using the impact parameter significance of both muon tracks as an indication of lifetime. Corrections were made for measured asymmetries from the detector, event

[1] f_d and f_s are the fractions for B_d and B_s mesons as discussed in Section 1.4.3. Z_d and Z_s are mixing related weights as described in [33]. Quantitatively, $A_{SL} = 0.6A_{SL}^{d} + 0.4A_{SL}^{s}$ since B_s mixes faster than B_d but more B_d are produced in collisions

trigger, and hadrons from B decays which were reconstructed as muon candidates. Removing the symmetric backgrounds dominated by sequential decays we find a semileptonic asymmetry of

$$A_{SL}^{\mu\mu} = 0.0080 \pm 0.0113. \tag{7.13}$$

This measurement can be interpreted as a determination of the CP asymmetry from B_s mixing using known values for the B_d mixing and the weights of contribution to the overall asymmetry:

$$A_{SL}^{s} = 0.0200 \pm 0.0283. \tag{7.14}$$

The value of A_{SL}^{s} taken with the recent measurements of B_s mass difference, Δm_s and decay width difference $\Delta\Gamma_s$ provides a constraint on the complex mixing phase of B_s mixing, ϕ_s. We find no evidence for CP violating physics beyond the Standard Model in B_s mixing, however, some new physics contribution to ϕ_s is not ruled out.

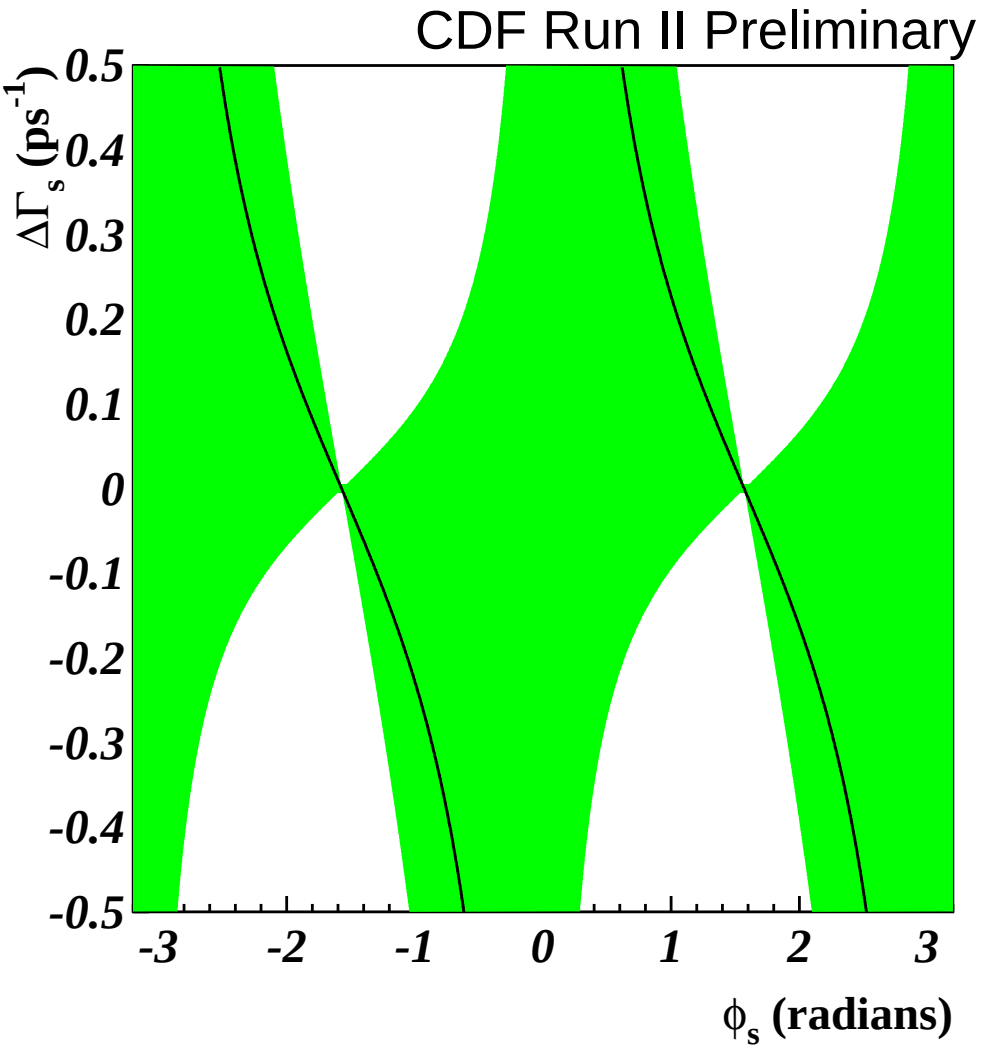

Figure 7.1: This result shown in the ϕ_s-$\Delta\Gamma_s$ plane. The lines represent the central value, the green region is the 68% allowed contour.

Chapter 8

Conclusions

This measurement of CP asymmetry in B_s mixing is consistent with Standard Model expectations. It provides a second precision determination of A^s_{SL}, and since the Tevatron is currently the only place to study B_s hadrons, it is the only available confirmation of the $D0$ analysis. An approach complimentary to the $D0$ analysis is used by isolating the signal fraction in the dimuon data by fitting the impact parameter. We have also corrected for pions which can contribute to the hadron asymmetry correction at the same level as kaons.

The greatest difficulty encountered in this dissertation research and perhaps the area in which there is the most room for future improvement is the high rate of hadrons from heavy flavor which are reconstructed as muon candidates. The correction for hadrons from B decays was the most complicated part of the analysis and contributed the largest systematic uncertainty to the asymmetry. Additionally, the effect of the high fake rates was present also in the charm decays. Previous analyses did not even consider contributions to same-sign muon candidate pairs where both muon candidates come from charm [51, 54], but we found that neglecting hadronic fakes from charm introduced a significant asymmetry. Another CDF analysis using a dimuon data selection from the same trigger found similarly high fake rates relative to Run I [56]. For this measurement to be made more accurately, the selection criteria may need to be tightened in areas that could yield a higher muon purity. At the analysis level the ΔX threshold for the muon matching could be decreased. Another option might be raising the P_T threshold which has the added benefit of reducing the fraction sequential decays that must be removed. Also, since the dimuon trigger used in this analysis has been prescaled[1] for higher luminosity, it is worth considering such changes to the trigger selection.

Other improvements might be made in a future asymmetry measurement to decrease the statistical uncertainty. Obviously, CDF is continuing to collect additional data and the high Tevatron luminosities will quickly provide increased statistical power. But, significant improvement can be achieved with the current data by increasing the muon acceptance. Muon candidates collected with triggers involving the CMX sub detector could provide increased $|\eta|$ acceptance, but would require careful determination of the associated hadron fake rates. Additionally, electrons are just as valid a source of semileptonic B decays as muons and have a similarly large branching ratio. Using electron candidates would of course introduce additional background considerations such as photon conversions. Electrons would also require high precision deter-

[1] A trigger prescale rejects a certain fraction of events which otherwise meet the selection criteria in order to conserve bandwidth for triggers with a lower cross-section.

minations of hadron fakes and any asymmetric effects in the calorimeters. From a technical aspect, an electron based CP asymmetry measurement is almost a completely different analysis. However, it could have comparable statistical power and could potentially be combined with the muon analysis to include $e\mu$ events. The addition of ee and $e\mu$ data would effectively triple the statistical power

Finally, the dimuon dataset is a rich source for studying b quark physics. As discussed in Appendix F, most of the necessary pieces for a measurement of the time-integrated mixing parameter $\overline{\chi}$ are in place. A better isolation of the relative background fractions and a more precise determination of the sequential fraction would likely be all that is necessary to measure $\overline{\chi}$ given more statistics. Such a measurement would help to understand the difference between the CDF measurement of $\overline{\chi}$ in Run I relative to those made in e^+e^- collisions [10, 55], and help to constrain the values of fragmentation fractions for B hadrons. Another soon to be published CDF analysis [56] uses similarly isolated dimuon data from BB decays to measure cross-section of correlated $b\overline{b}$ production. This measurement would also improve with increased lepton acceptance and muon candidate purity.

Appendix A

Glossary

$\mathbf{A_{CP}}$: Charge asymmetry introduced by CP violation in neutral B mixing.
$\mathbf{A_{SL}}$: A_{CP} measured in inclusive semileptonic B decays.
$\mathbf{A_{SL}^{s}}$: A_{SL} measured in semileptonic B_s mixing decays.
BB: Sample of muon pairs where both muon candidates are from B hadron decays.
CC: Sample of muon pairs where both muon candidates are from C hadron decays.
CDF: Collider Detector at Fermilab.
CLC: Cherenkov Luminosity Counter.
CKM: Cabibbo-Kobayashi-Maskawa matrix describing quark flavor changing transitions.
CMP: Central Muon uPgrade.
CMU: Central MUon Detector.
CMX: Central Muon eXtension.
COT: Central Outer Tracker.
CP: Charge-Parity
L1: Level 1 of the CDF Trigger.
L2: Level 2 of the CDF Trigger.
L3: Level 3 of the CDF Trigger.
MI: Main Injector.
MC: Monte Carlo.
OS: Opposite-sign muon pair sample.
PB, PC, and PP: Sample of muon pairs where one muon candidate is from a prompt source, and the second muon comes from a B hadron, a C hadron, or prompt source respectively.
RF: Radio-frequency.
SL: Semileptonic; heavy flavor decays which produce both hadrons and leptons.
SM: Standard Model of particle physics
SS: Same-sign muon pair sample
SVT: Silicon Vertex Trigger.
SVX: Silicon VerteX Tracker.
XFT: eXtremely Fast Tracker.
XTRP: eXTRaPolation Unit.

Appendix B

CDF Author List

CDF Default Author List from July 2006 to January 2007:

A. Abulencia,[23] J. Adelman,[13] T. Aolder,[10] T. Akimoto,[55] M.G. Albrow,[16] D. Ambrose,[16] S. Amerio,[43] D. Amidei,[34] A. Anastassov,[52] K. Anikeev,[16] A. Annovi,[18] J. Antos, [1] M. Aoki,[55] G. Apollinari,[16] J.-F. Arguin,[33] T. Arisawa,[57] A. Artikov,[14] W. Ashmanskas,[16] A. Attal,[8] F. Azfar,[42] P. Azzi-Bacchetta,[43] P. Azzurri,[46] N. Bacchetta,[43] W. Badgett,[16] A. Barbaro-Galtieri,[28] V.E. Barnes,[48] B.A. Barnett,[24] S. Baroiant,[7] V. Bartsch,[30] G. Bauer,[32] F. Bedeschi,[46] S. Behari,[24] S. Belforte,[54] G. Bellettini,[46] J. Bellinger,[59] A. Belloni,[32] D. Benjamin,[15] A. Beretvas,[16] J. Beringer,[28] T. Berry,[29] A. Bhatti,[50] M. Binkley,[16] D. Bisello,[43] R.E. Blair,[2] C. Blocker,[6] B. Blumenfeld,[24] A. Bocci,[15] A. Bodek,[49] V. Boisvert,[49] G. Bolla,[48] A. Bolshov,[32] D. Bortoletto,[48] J. Boudreau,[47] A. Boveia,[10] B. Brau,[10] L. Brigliadori,[5] C. Bromberg,[35] E. Brubaker,[13] J. Budagov,[14] H.S. Budd,[49] S. Budd,[23] S. Budroni,[46] K. Burkett,[16] G. Busetto,[43] P. Bussey,[20] K. L. Byrum,[2] S. Cabrera,[15] M. Campanelli,[19] M. Campbell,[34] F. Canelli,[16] A. Canepa,[48] S. Carrillo,[17] D. Carlsmith,[59] R. Carosi,[46] S. Carron,[33] M. Casarsa,[54] A. Castro,[5] P. Catastini,[46] D. Cauz,[54] M. Cavalli-Sforza,[3] A. Cerri,[28] L. Cerrito,[30] S.H. Chang,[27] Y.C. Chen, [1] M. Chertok,[7] G. Chiarelli,[46] G. Chlachidze,[14] F. Chlebana,[16] I. Cho,[27] K. Cho,[27] D. Chokheli,[14] J.P. Chou,[21] G. Choudalakis,[32] S.H. Chuang,[59] K. Chung,[12] W.H. Chung,[59] Y.S. Chung,[49] M. Ciljak,[46] C.I. Ciobanu,[23] M.A. Ciocci,[46] A. Clark,[19] D. Clark,[6] M. Coca,[15] G. Compostella,[43] M.E. Convery,[50] J. Conway,[7] B. Cooper,[35] K. Copic,[34] M. Cordelli,[18] G. Cortiana,[43] F. Crescioli,[46] C. Cuenca Almenar,[7] J. Cuevas,[11] R. Culbertson,[16] J.C. Cully,[34] D. Cyr,[59] S. DaRonco,[43] S. D'Auria,[20] T. Davies,[20] M. D'Onofrio,[3] D. Dagenhart,[6] P. de Barbaro,[49] S. De Cecco,[51] A. Deisher,[28] G. De Lentdecker,[49] M. Dell'Orso,[46] F. Delli Paoli,[43] L. Demortier,[50] J. Deng,[15] M. Deninno,[5] D. De Pedis,[51] P.F. Derwent,[16] C. Dionisi,[51] B. Di Ruzza,[54] J.R. Dittmann,[4] P. DiTuro,[52] C. Dörr,[25] S. Donati,[46] M. Donega,[19] P. Dong,[8] J. Donini,[43] T. Dorigo,[43] S. Dube,[52] J. Efron,[39] R. Erbacher,[7] D. Errede,[23] S. Errede,[23] R. Eusebi,[16] H.C. Fang,[28] S. Farrington,[29] I. Fedorko,[46] W.T. Fedorko,[13] R.G. Feild,[60] M. Feindt,[25] J.P. Fernandez,[31] R. Field,[17] G. Flanagan,[48] A. Foland,[21] S. Forrester,[7] G.W. Foster,[16] M. Franklin,[21] J.C. Freeman,[28] I. Furic,[13] M. Gallinaro,[50] J. Galyardt,[12] J.E. Garcia,[46] F. Garberson,[10] A.F. Garfinkel,[48] C. Gay,[60] H. Gerberich,[23] D. Gerdes,[34] S. Giagu,[51] P. Giannetti,[46] A. Gibson,[28] K. Gibson,[47] J.L. Gimmell,[49] C. Ginsburg,[16] N. Giokaris,[14] M. Giordani,[54] P. Giromini,[18] M. Giunta,[46] G. Giurgiu,[12] V. Glagolev,[14] D. Glenzinski,[16] M. Gold,[37] N. Goldschmidt,[17] J. Goldstein,[42] G. Gomez,[11] G. Gomez-Ceballos,[11] M. Goncharov,[53]

O. González,[31] I. Gorelov,[37] A.T. Goshaw,[15] K. Goulianos,[50] A. Gresele,[43] M. Griths,[29] S. Grinstein,[21] C. Grosso-Pilcher,[13] R.C. Group,[17] U. Grundler,[23] J. Guimaraes da Costa,[21] Z. Gunay-Unalan,[35] C. Haber,[28] K. Hahn,[32] S.R. Hahn,[16] E. Halkiadakis,[52] A. Hamilton,[33] B.-Y. Han,[49] J.Y. Han,[49] R. Handler,[59] F. Happacher,[18] K. Hara,[55] M. Hare,[56] S. Harper,[42] R.F. Harr,[58] R.M. Harris,[16] M. Hartz,[47] K. Hatakeyama,[50] J. Hauser,[8] A. Heijboer,[45] B. Heinemann,[29] J. Heinrich,[45] C. Henderson,[32] M. Herndon,[59] J. Heuser,[25] D. Hidas,[15] C.S. Hill,[10] D. Hirschbuehl,[25] A. Hocker,[16] A. Holloway,[21] S. Hou,[1] M. Houlden,[29] S.-C. Hsu,[9] B.T. Human,[42] R.E. Hughes,[39] U. Husemann,[60] J. Huston,[35] J. Incandela,[10] G. Introzzi,[46] M. Iori,[51] Y. Ishizawa,[55] A. Ivanov,[7] B. Iyutin,[32] E. James,[16] D. Jang,[52] B. Jayatilaka,[34] D. Jeans,[51] H. Jensen,[16] E.J. Jeon,[27] S. Jindariani,[17] M. Jones,[48] K.K. Joo,[27] S.Y. Jun,[12] J.E. Jung,[27] T.R. Junk,[23] T. Kamon,[53] P.E. Karchin,[58] Y. Kato,[41] Y. Kemp,[25] R. Kephart,[16] U. Kerzel,[25] V. Khotilovich,[53] B. Kilminster,[39] D.H. Kim,[27] H.S. Kim,[27] J.E. Kim,[27] M.J. Kim,[12] S.B. Kim,[27] S.H. Kim,[55] Y.K. Kim,[13] N. Kimura,[55] L. Kirsch,[6] S. Klimenko,[17] M. Klute,[32] B. Knuteson,[32] B.R. Ko,[15] K. Kondo,[57] D.J. Kong,[27] J. Konigsberg,[17] A. Korytov,[17] A.V. Kotwal,[15] A. Kovalev,[45] A.C. Kraan,[45] J. Kraus,[23] I. Kravchenko,[32] M. Kreps,[25] J. Kroll,[45] N. Krumnack,[4] M. Kruse,[15] V. Krutelyov,[10] T. Kubo,[55] S. E. Kuhlmann,[2] T. Kuhr,[25] Y. Kusakabe,[57] S. Kwang,[13] A.T. Laasanen,[48] S. Lai,[33] S. Lami,[46] S. Lammel,[16] M. Lancaster,[30] R.L. Lander,[7] K. Lannon,[39] A. Lath,[52] G. Latino,[46] I. Lazzizzera,[43] T. LeCompte,[2] J. Lee,[49] J. Lee,[27] Y.J. Lee,[27] S.W. Lee,[53] R. Lefèvre,[3] N. Leonardo,[32] S. Leone,[46] S. Levy,[13] J.D. Lewis,[16] C. Lin,[60] C.S. Lin,[16] M. Lindgren,[16] E. Lipeles,[9] A. Lister,[7] D.O. Litvintsev,[16] T. Liu,[16] N.S. Lockyer,[45] A. Loginov,[36] M. Loreti,[43] P. Loverre,[51] R.-S. Lu,[1] D. Lucchesi,[43] P. Lujan,[28] P. Lukens,[16] G. Lungu,[17] L. Lyons,[42] J. Lys,[28] R. Lysak,[1] E. Lytken,[48] P. Mack,[25] D. MacQueen,[33] R. Madrak,[16] K. Maeshima,[16] K. Makhoul,[32] T. Maki,[22] P. Maksimovic,[24] S. Malde,[42] G. Manca,[29] F. Margaroli,[5] R. Marginean,[16] C. Marino,[25] C.P. Marino,[23] A. Martin,[60] M. Martin,[24] V. Martin,[20] M. Martínez,[3] T. Maruyama,[55] P. Mastrandrea,[51] T. Masubuchi,[55] H. Matsunaga,[55] M.E. Mattson,[58] R. Mazini,[33] P. Mazzanti,[5] K.S. McFarland,[49] P. McIntyre,[53] R. McNulty,[29] A. Mehta,[29] P. Mehtala,[22] S. Menzemer,[11] A. Menzione,[46] P. Merkel,[48] C. Mesropian,[50] A. Messina,[51] T. Miao,[16] N. Miladinovic,[6] J. Miles,[32] R. Miller,[35] C. Mills,[10] M. Milnik,[25] A. Mitra,[1] G. Mitselmakher,[17] A. Miyamoto,[26] S. Moed,[19] N. Moggi,[5] B. Mohr,[8] R. Moore,[16] M. Morello,[46] P. Movilla Fernandez,[28] J. Mülmenstädt,[28] A. Mukherjee,[16] Th. Muller,[25] R. Mumford,[24] P. Murat,[16] J. Nachtman,[16] A. Nagano,[55] J. Naganoma,[57] S. Nahn,[32] I. Nakano,[40] A. Napier,[56] V. Necula,[17] C. Neu,[45] M.S. Neubauer,[9] J. Nielsen,[28] T. Nigmanov,[47] L. Nodulman,[2] O. Norniella,[3] E. Nurse,[30] S.H. Oh,[15] Y.D. Oh,[27] I. Oksuzian,[17] T. Okusawa,[41] R. Oldeman,[29] R. Orava,[22] K. Osterberg,[22] C. Pagliarone,[46] E. Palencia,[11] V. Papadimitriou,[16] A.A. Paramonov,[13] B. Parks,[39] S. Pashapour,[33] J. Patrick,[16] G. Pauletta,[54] M. Paulini,[12] C. Paus,[32] D.E. Pellett,[7] A. Penzo,[54] T.J. Phillips,[15] G. Piacentino,[46] J. Piedra,[44] L. Pinera,[17] K. Pitts,[23] C. Plager,[8] L. Pondrom,[59] X. Portell,[3] O. Poukhov,[14] N. Pounder,[42] F. Prokoshin,[14] A. Pronko,[16] J. Proudfoot,[2] F. Ptochos,[18] G. Punzi,[46] J. Pursley,[24] J. Rademacker,[42] A. Rahaman,[47] N. Ranjan,[48] S. Rappoccio,[21] B. Reisert,[16] V. Rekovic,[37] P. Renton,[42] M. Rescigno,[51] S. Richter,[25] F. Rimondi,[5] L. Ristori,[46] A. Robson,[20] T. Rodrigo,[11] E. Rogers,[23] S. Rolli,[56] R. Roser,[16] M. Rossi,[54] R. Rossin,[17] A. Ruiz,[11] J. Russ,[12] V. Rusu,[13] H. Saarikko,[22] S.

Sabik,[33] A. Safonov,[53] W.K. Sakumoto,[49] G. Salamanna,[51] O. Saltó,[3] D. Saltzberg,[8] C. Sánchez,[3] L. Santi,[54] S. Sarkar,[51] L. Sartori,[46] K. Sato,[16] P. Savard,[33] A. Savoy-Navarro,[44] T. Scheidle,[25] P. Schlabach,[16] E.E. Schmidt,[16] M.P. Schmidt,[60] M. Schmitt,[38] T. Schwarz,[7] L. Scodellaro,[11] A.L. Scott,[10] A. Scribano,[46] F. Scuri,[46] A. Sedov,[48] S. Seidel,[37] Y. Seiya,[41] A. Semenov,[14] L. Sexton-Kennedy,[16] A. Sfyrla,[19] M.D. Shapiro,[28] T. Shears,[29] P.F. Shepard,[47] D. Sherman,[21] M. Shimojima,[55] M. Shochet,[13] Y. Shon,[59] I. Shreyber,[36] A. Sidoti,[46] P. Sinervo,[33] A. Sisakyan,[14] J. Sjolin,[42] A.J. Slaughter,[16] J. Slaunwhite,[39] K. Sliwa,[56] J.R. Smith,[7] F.D. Snider,[16] R. Snihur,[33] M. Soderberg,[34] A. Soha,[7] S. Somalwar,[52] V. Sorin,[35] J. Spalding,[16] F. Spinella,[46] T. Spreitzer,[33] P. Squillacioti,[46] M. Stanitzki,[60] A. Staveris-Polykalas,[46] R. St. Denis,[20] B. Stelzer,[8] O. Stelzer-Chilton,[42] D. Stentz,[38] J. Strologas,[37] D. Stuart,[10] J.S. Suh,[27] A. Sukhanov,[17] H. Sun,[56] T. Suzuki,[55] A. Taffard,[23] R. Takashima,[40] Y. Takeuchi,[55] K. Takikawa,[55] M. Tanaka,[2] R. Tanaka,[40] M. Tecchio,[34] P.K. Teng,[1] K. Terashi,[50] J. Thom,[16] A.S. Thompson,[20] E. Thomson,[45] P. Tipton,[60] V. Tiwari,[12] S. Tkaczyk,[16] D. Toback,[53] S. Tokar,[14] K. Tollefson,[35] T. Tomura,[55] D. Tonelli,[46] S. Torre,[18] D. Torretta,[16] S. Tourneur,[44] W. Trischuk,[33] R. Tsuchiya,[57] S. Tsuno,[40] N. Turini,[46] F. Ukegawa,[55] T. Unverhau,[20] S. Uozumi,[55] D. Usynin,[45] S. Vallecorsa,[19] N. van Remortel,[22] A. Varganov,[34] E. Vataga,[37] F. Vázquez,[17] G. Velev,[16] G. Veramendi,[23] V. Veszpremi,[48] R. Vidal,[16] I. Vila,[11] R. Vilar,[11] T. Vine,[30] I. Vollrath,[33] I. Volobouev,[28] G. Volpi,[46] F. Würthwein,[9] P. Wagner,[53] R.G. Wagner,[2] R.L. Wagner,[16] J. Wagner,[25] W. Wagner,[25] R. Wallny,[8] S.M. Wang,[1] A. Warburton,[33] S. Waschke,[20] D. Waters,[30] M. Weinberger,[53] W.C. Wester III,[16] B. Whitehouse,[56] D. Whiteson,[45] A.B. Wicklund,[2] E. Wicklund,[16] G. Williams,[33] H.H. Williams,[45] P. Wilson,[16] B.L. Winer,[39] P. Wittich,[16] S. Wolbers,[16] C. Wolfe,[13] T. Wright,[34] X. Wu,[19] S.M. Wynne,[29] A. Yagil,[16] K. Yamamoto,[41] J. Yamaoka,[52] T. Yamashita,[40] C. Yang,[60] U.K. Yang,[13] Y.C. Yang,[27] W.M. Yao,[28] G.P. Yeh,[16] J. Yoh,[16] K. Yorita,[13] T. Yoshida,[41] G.B. Yu,[49] I. Yu,[27] S.S. Yu,[16] J.C. Yun,[16] L. Zanello,[51] A. Zanetti,[54] I. Zaw,[21] X. Zhang,[23] J. Zhou,[52] and S. Zucchelli[5]

(CDF Collaboration)

[1] *Institute of Physics, Academia Sinica, Taipei, Taiwan 11529, Republic of China*

[2] *Argonne National Laboratory, Argonne, Illinois 60439*

[3] *Institut de Fisica d'Altes Energies, Universitat Autonoma de Barcelona, E-08193, Bellaterra (Barcelona), Spain*

[4] *Baylor University, Waco, Texas 76798*

[5] *Istituto Nazionale di Fisica Nucleare, University of Bologna, I-40127 Bologna, Italy*

[6] *Brandeis University, Waltham, Massachusetts 02254*

[7] *University of California, Davis, Davis, California 95616*

[8] *University of California, Los Angeles, Los Angeles, California 90024*

[9] *University of California, San Diego, La Jolla, California 92093*

[10] *University of California, Santa Barbara, Santa Barbara, California 93106*

[11] *Instituto de Fisica de Cantabria, CSIC-University of Cantabria, 39005 Santander, Spain*

[12] *Carnegie Mellon University, Pittsburgh, PA 15213*

[13] *Enrico Fermi Institute, University of Chicago, Chicago, Illinois 60637*

[14] *Joint Institute for Nuclear Research, RU-141980 Dubna, Russia*

[15] *Duke University, Durham, North Carolina 27708*
[16] *Fermi National Accelerator Laboratory, Batavia, Illinois 60510*
[17] *University of Florida, Gainesville, Florida 32611*
[18] *Laboratori Nazionali di Frascati, Istituto Nazionale di Fisica Nucleare, I-00044 Frascati, Italy*
[19] *University of Geneva, CH-1211 Geneva 4, Switzerland*
[20] *Glasgow University, Glasgow G12 8QQ, United Kingdom*
[21] *Harvard University, Cambridge, Massachusetts 02138*
[22] *Division of High Energy Physics, Department of Physics,*
University of Helsinki and Helsinki Institute of Physics, FIN-00014, Helsinki, Finland
[23] *University of Illinois, Urbana, Illinois 61801*
[24] *The Johns Hopkins University, Baltimore, Maryland 21218*
[25] *Institut für Experimentelle Kernphysik, Universität Karlsruhe, 76128 Karlsruhe, Germany*
[26] *High Energy Accelerator Research Organization (KEK), Tsukuba, Ibaraki 305, Japan*
[27] *Center for High Energy Physics: Kyungpook National University,*
Taegu 702-701, Korea; Seoul National University, Seoul 151-742,
Korea; and SungKyunKwan University, Suwon 440-746, Korea
[28] *Ernest Orlando Lawrence Berkeley National Laboratory, Berkeley, California 94720*
[29] *University of Liverpool, Liverpool L69 7ZE, United Kingdom*
[30] *University College London, London WC1E 6BT, United Kingdom*
[31] *Centro de Investigaciones Energeticas Medioambientales y Tecnologicas, E-28040 Madrid,*
Spain
[32] *Massachusetts Institute of Technology, Cambridge, Massachusetts 02139*
[33] *Institute of Particle Physics: McGill University, Montréal,*
Canada H3A 2T8; and University of Toronto, Toronto, Canada M5S 1A7
[34] *University of Michigan, Ann Arbor, Michigan 48109*
[35] *Michigan State University, East Lansing, Michigan 48824*
[36] *Institution for Theoretical and Experimental Physics, ITEP, Moscow 117259, Russia*
[37] *University of New Mexico, Albuquerque, New Mexico 87131*
[38] *Northwestern University, Evanston, Illinois 60208*
[39] *The Ohio State University, Columbus, Ohio 43210*
[40] *Okayama University, Okayama 700-8530, Japan*
[41] *Osaka City University, Osaka 588, Japan*
[42] *University of Oxford, Oxford OX1 3RH, United Kingdom*
[43] *University of Padova, Istituto Nazionale di Fisica Nucleare,*
Sezione di Padova-Trento, I-35131 Padova, Italy
[44] *LPNHE, Universite Pierre et Marie Curie/IN2P3-CNRS, UMR7585, Paris, F-75252 France*
[45] *University of Pennsylvania, Philadelphia, Pennsylvania 19104*
[46] *Istituto Nazionale di Fisica Nucleare Pisa, Universities of Pisa, Siena and Scuola Normale*
Superiore, I-56127 Pisa, Italy
[47] *University of Pittsburgh, Pittsburgh, Pennsylvania 15260*
[48] *Purdue University, West Lafayette, Indiana 47907*

[49] *University of Rochester, Rochester, New York 14627*
[50] *The Rockefeller University, New York, New York 10021*
[51] *Istituto Nazionale di Fisica Nucleare, Sezione di Roma 1, University of Rome "La Sapienza," I-00185 Roma, Italy*
[52] *Rutgers University, Piscataway, New Jersey 08855*
[53] *Texas A&M University, College Station, Texas 77843*
[54] *Istituto Nazionale di Fisica Nucleare, University of Trieste/ Udine, Italy*
[55] *University of Tsukuba, Tsukuba, Ibaraki 305, Japan*
[56] *Tufts University, Medford, Massachusetts 02155*
[57] *Waseda University, Tokyo 169, Japan*
[58] *Wayne State University, Detroit, Michigan 48201*
[59] *University of Wisconsin, Madison, Wisconsin 53706*
[60] *Yale University, New Haven, Connecticut 06520*
(Dated: September 1, 2006)

Appendix C

Impact Parameter Significance

The original approach to this analysis was to fit the impact parameter of both muons as in the Run I χ_0 analysis, [55]. However, as Figure C.1 demonstrates, there was significant disagreement of the fitted components compared to the data at large impact parameter. Our concern was that this divergence in the tail was caused by pattern recognition failures or tracks with larger impact parameter uncertainty. By incorporating the measured uncertainty of each impact parameter to construct a significance much of this discrepancy was accounted for.

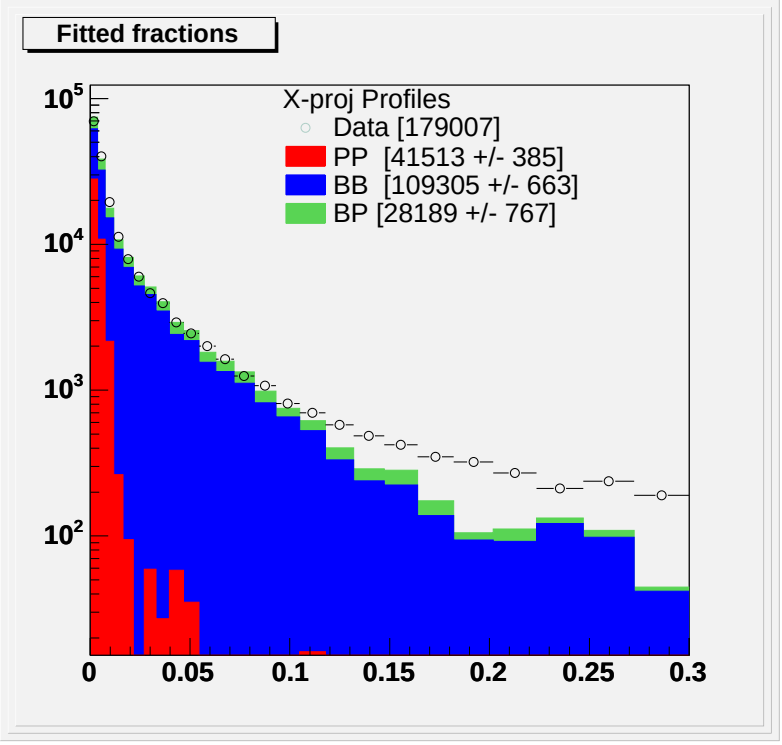

Figure C.1: The fractional contributions as determined by the likelihood fit are stacked and compared to the combined same-sign dimuon data set.

Appendix D

Monte Carlo Samples

The Monte Carlo samples generated for this analysis used software release 5.3.4 and followed the B group prescription specified in [65].

D.1 Pythia/Evtgen Samples

The bottom and charm samples that were utilized to derive the BB, PB, CC and PC templates were generated with Pythia. Pythia is a Monte Carlo tool used in high-energy physics to model events of outgoing particles produced in interactions of two incoming particles [58]. To get a realistic mixture of $b\bar{b}$ production processes, we generated all $2 \to 2$ processes (msel=1). The minimum $\hat{p}_T$ was set to 10 GeV. We generated an additional sample with minimum $\hat{p}_T$ set to 8 GeV to verify that we did not see any sculpting in the 10 GeV sample. B hadrons were decayed with Evtgen. EvtGen is another Monte Carlo event generator explicitly designed for simulating the physics of B hadron decays and is particularly helpful in modeling sequential decays, semileptonic decays, and CP violating decays [59].

For the b MC, mixing was turned off and we forced the bottom quark to decay muonically. The $\bar{b}$ was allowed to decay freely. Events were then filtered to require at least one real muon with $p_T > 2.8$ GeV and $|\eta| < 0.7$ before simulation and subsequent analysis. We supplemented the original $b\bar{b}$ MC with a flavor creation (msel=5) sample. The msel=1 and msel=5 samples were compared and found to produce similar impact distributions.

The charm MC was generated in Pythia using flavor creation (msel=4) with minimum $\hat{p}_T = 8$ GeV. The charm hadrons were decayed using the standard Evtgen decay table. (No decays were forced.) [Note: The original charm MC for this analysis was msel=1 without Evtgen. That sample is no longer used in the analysis.]

For control studies, we additionally generated a Pythia sample of all $2 \to 2$ processes where we did not select heavy flavor events. This u,d,s was used to study the PP template.

All Pythia samples were generated using Peterson fragmentation, with $\epsilon_P = 0.006$ along with underlying event "tune A". The ratio of vector to pseudo-scalar heavy hadron production ($P_v = V/(V+P)$) is set to the default value of 0.75.

A full CDF detector simulation is run for the MC samples using the Geant [60] software package. Geant models the passage of particles through matter, and the CDF detector components. The tracking response in particular is simulated in great detail.

D.2 FakeEvent Samples

FakeEvent is the name of the single particle generator in CDF simulation software. The species of particle as well as the distributions of P_T, η and ϕ for the particles are input to the generator. The detector response is simulated using GEANT.

For dedicated systematic studies, we followed the 5.3.4 MC prescription while using FakeEvent to generate the following samples:

1. $\Upsilon(1s) \rightarrow \mu^+\mu^-$,
2. $\mu^-\mu^-$,
3. $\mu^+\mu^+$,
4. single μ^+ and μ^-,
5. single K^+, K^-, π^+ and π^-.

Since these were single (or double) track events with no other activity, we were able to generate extremely large samples for systematic study.

In all cases, the p_T spectrum used came from the data (Υ or dimuon p_T spectrum). In all cases, the events were generated flat in $0 < \phi < 360^\circ$ and flat in $-1 < y < 1$. The Υ sample was used to compare to the PP template derived from real $\Upsilon \rightarrow \mu^+\mu^-$ decays. The muon samples were used to map out the acceptance for same sign dimuon events.

The single hadron MC ($K^\pm$, $\pi^\pm$) was generated to check our measurement of the fake muon asymmetry coming from hadrons. In these samples, we passed every event through the simulation and reconstruction and then kept only events with an identified CMUP muon candidate.

Appendix E

Further Analysis Checks

E.1 Additional Kinematic Profiles

Figures E.1 - E.3 show some additional checks of the average impact parameter significance over a range of different kinematic variables. It is not the average values themselves that are of interest but the shape of the distributions that we are checking for any biases. The shape of the distributions for ϕ and Z_0 of the muon candidates reflects the geometrical structure of the SVX detector as described in Section 2.2.3. Where there is less silicon information the average impact parameter uncertainty is greater and thus the average significance is smaller. It was verified that the same distribution shapes are reflected in the Monte Carlo used for template construction.

E.2 Toy Experiments

In order to validate the templates and fitting code a number of toy experiments were created and fitted. Many of these were used in testing and improving the fitting templates and strategy. We used a number of differing input values for the components and found that the output values were also very consistent. Once the technique was settled and the data had been fit we generated 2500 experiments of 500,000 events with the final templates and used input values based on the fitted values of the data. The results are given in Table E.1 and the pull distributions are shown in Figures E.4 - E.7. Several sets of toy experiments using differing input values for the components were repeated and found to be consistently unbiased, but only the default results are listed here.

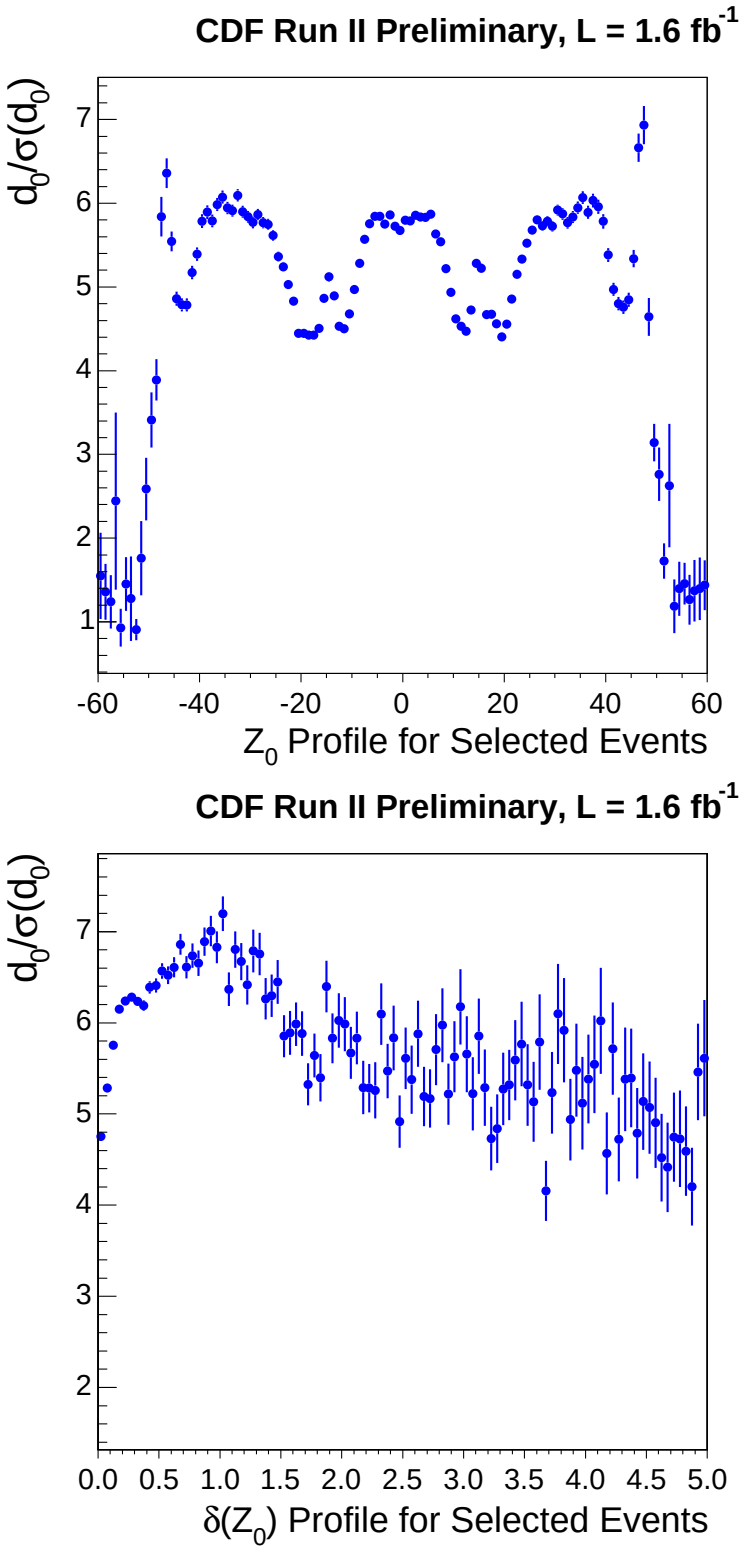

Figure E.1: Signal dimuon kinematic distributions for all muon candidates pairs passing analysis cuts: (top)Z_0 profile over d_0 and (bottom)$\delta(Z_0)$.

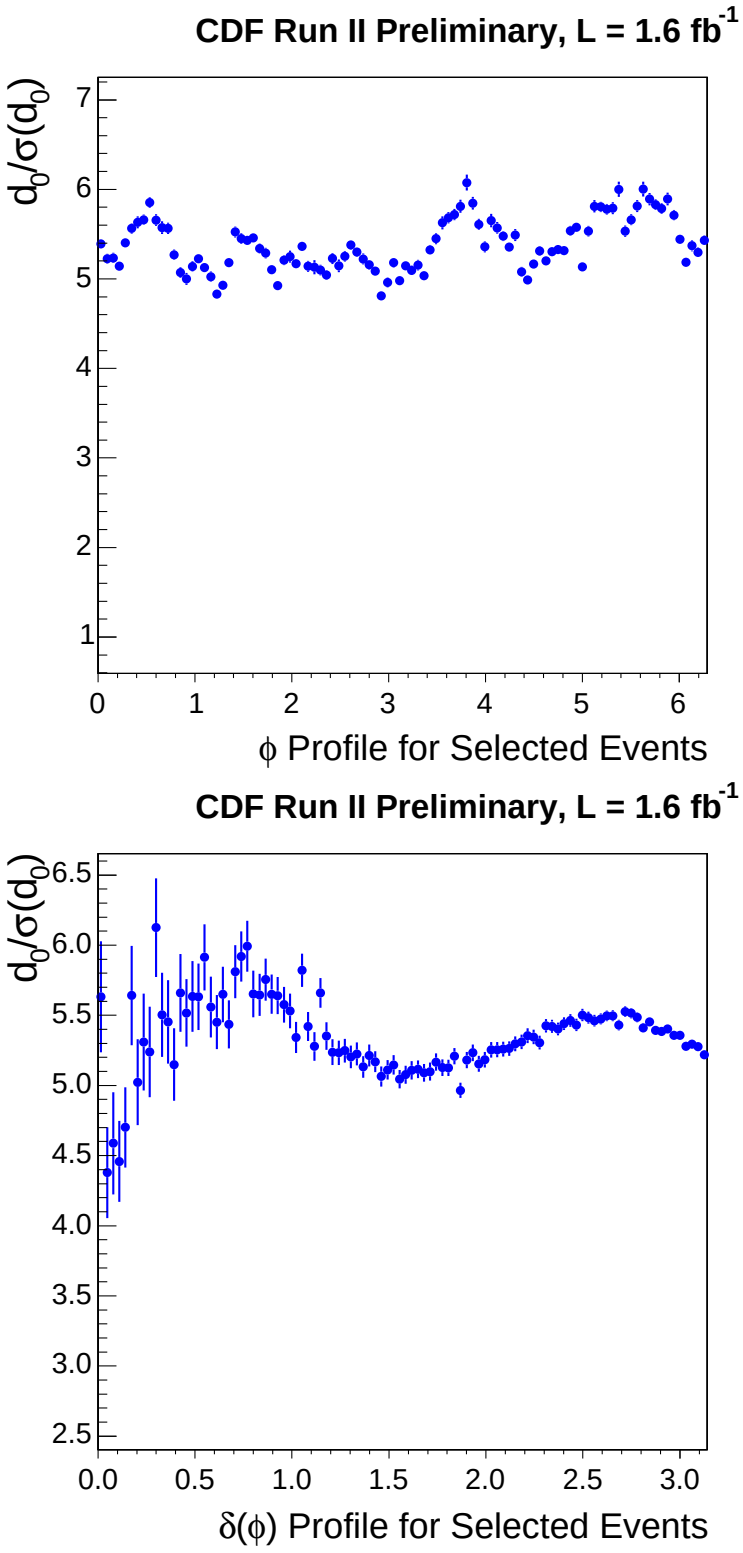

Figure E.2: Signal dimuon kinematic distributions for all muon candidates pairs passing analysis cuts: (top)ϕ profile over d_0 and (bottom)$\delta(\phi)$.

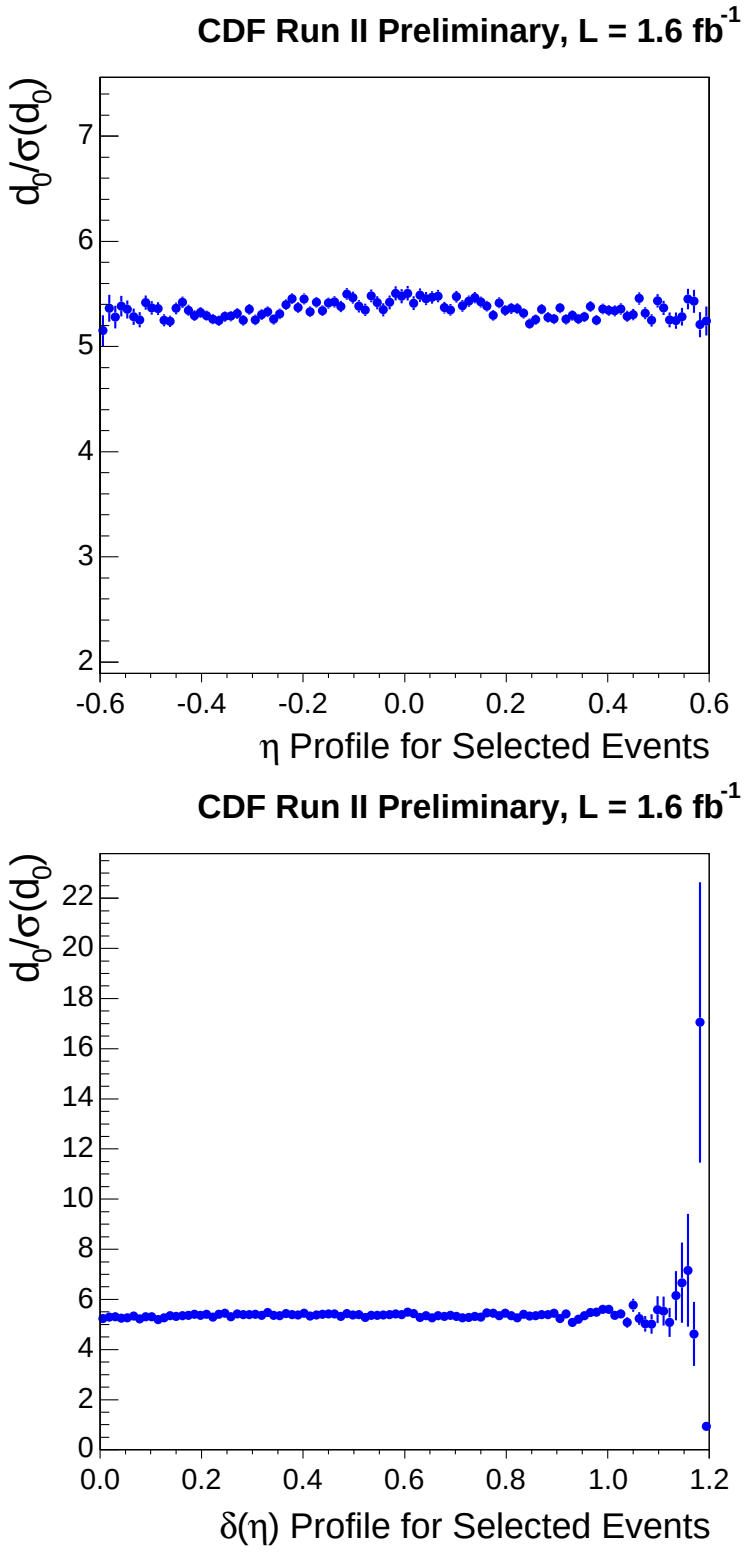

Figure E.3: Signal dimuon kinematic distributions for all muon candidates pairs passing analysis cuts: (top)η profile over d_0 and (bottom)$\delta(\eta)$.

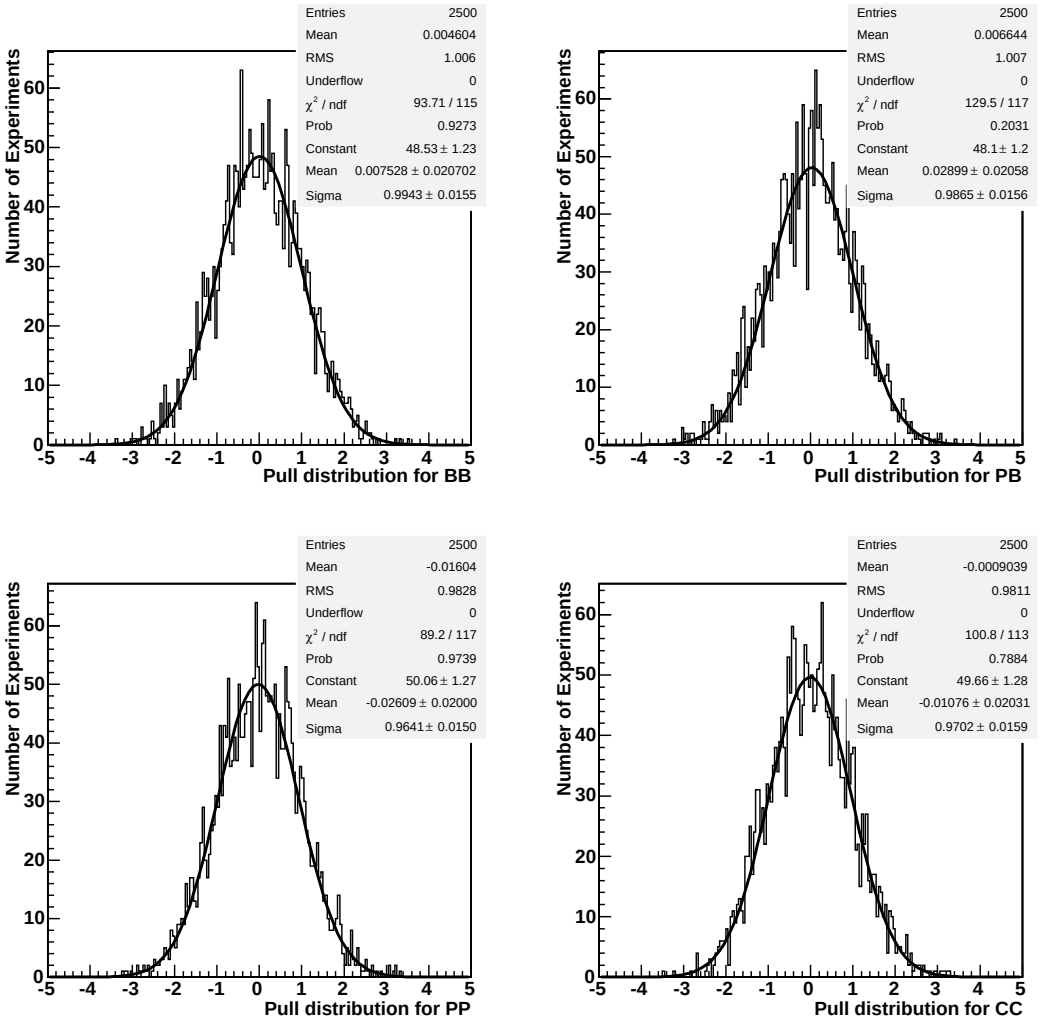

Figure E.4: Pull distributions for $\mu^+\mu^-$ fitting of BB, PB, PP, and CC.

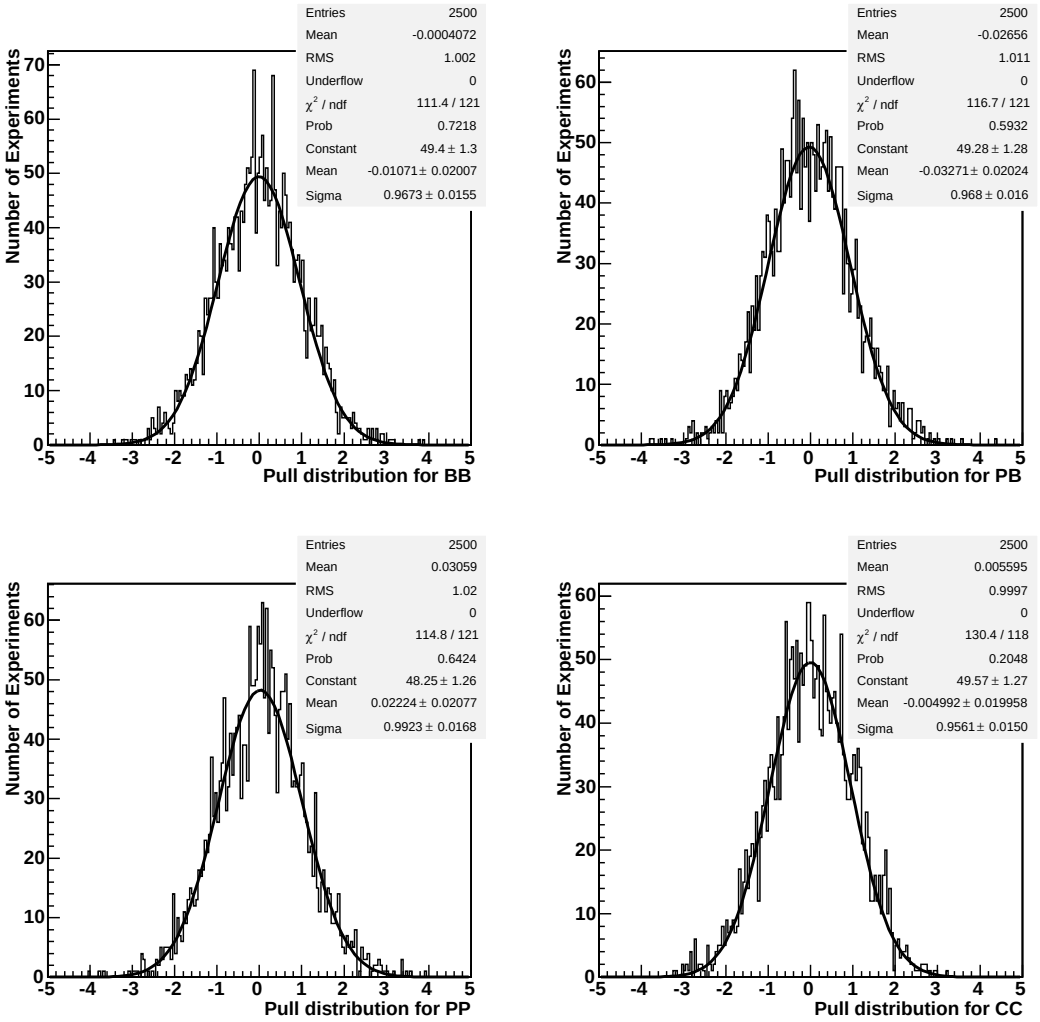

Figure E.5: Pull distributions for $\mu^+\mu^+$ fitting of BB, PB, PP, and CC.

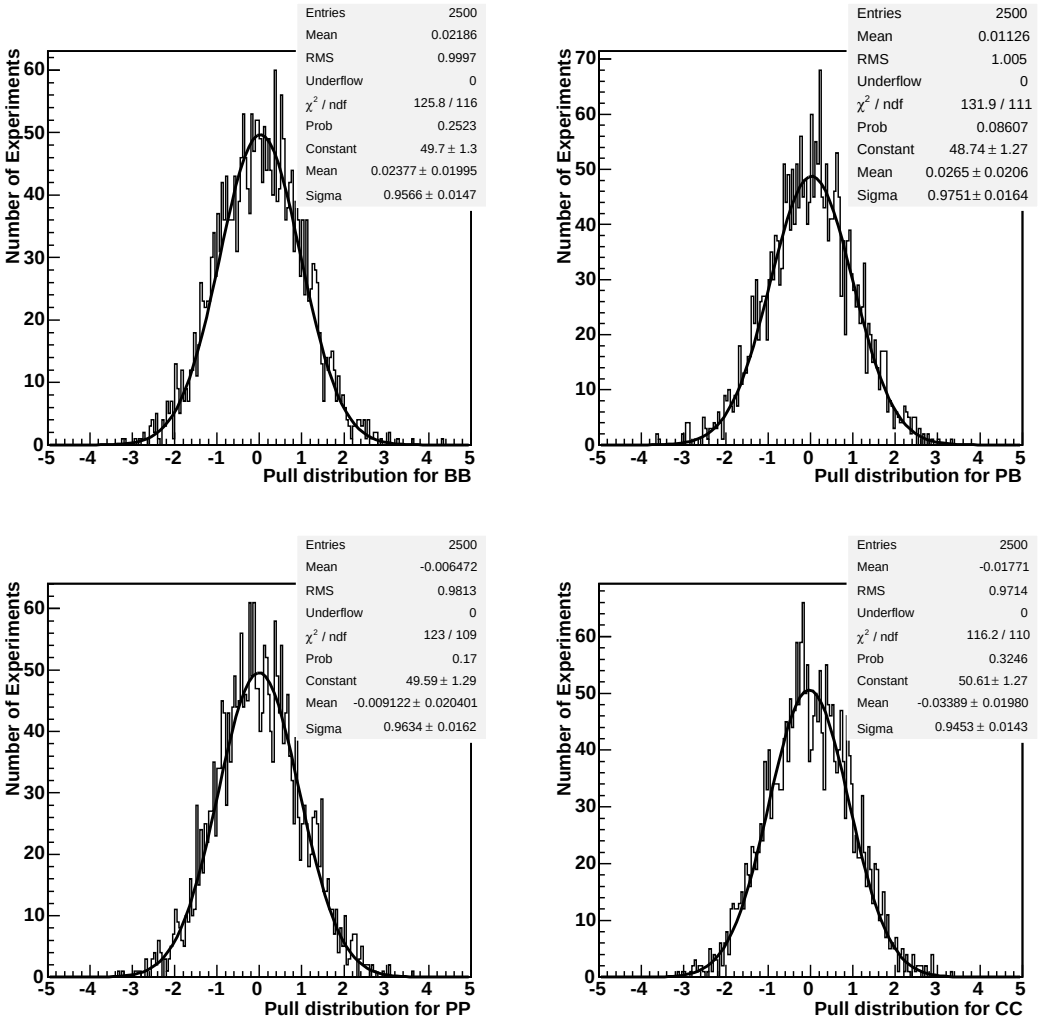

Figure E.6: Pull distributions for $\mu^-\mu^-$ fitting of BB, PB, PP, and CC.

Component	Avg. Value	Avg. Error	Pull Mean	Pull Width
$+-BB$	43.0	0.28	0.01 ± 0.02	0.99 ± 0.02
$+-PB$	7.0	0.42	0.03 ± 0.02	0.99 ± 0.02
$+-PP$	21.0	0.25	-0.03 ± 0.02	0.96 ± 0.02
$+-CC$	29.0	0.57	-0.01 ± 0.02	0.97 ± 0.02
$++BB$	48.0	0.49	-0.01 ± 0.02	0.97 ± 0.02
$++PB$	17.0	0.75	-0.03 ± 0.02	0.97 ± 0.02
$++PP$	27.0	0.43	0.02 ± 0.02	0.99 ± 0.02
$++CC$	8.0	0.99	0.00 ± 0.02	0.96 ± 0.02
$--BB$	48.0	0.49	0.02 ± 0.02	0.96 ± 0.02
$--PB$	17.0	0.75	0.03 ± 0.02	0.98 ± 0.02
$--PP$	27.0	0.43	-0.01 ± 0.02	0.96 ± 0.02
$--CC$	8.0	0.99	-0.03 ± 0.02	0.95 ± 0.02

Table E.1: Toy Experiment Results: each experiment contains 300k opposite-sign events and 200k same-sign events split evenly between $\mu^+\mu^+$ and $\mu^-\mu^-$subsets.

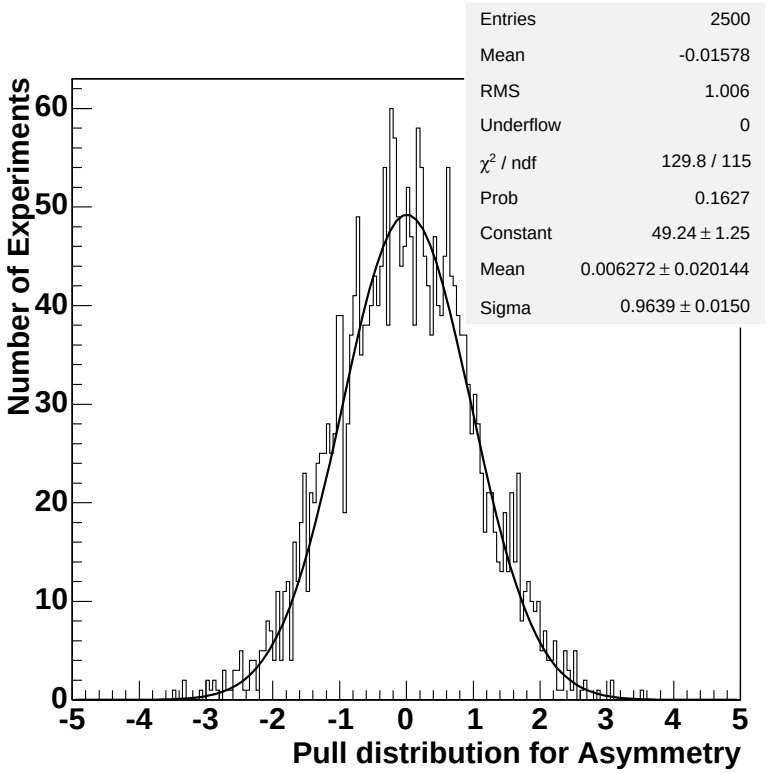

Figure E.7: Pull distribution for the fitted raw asymmetry

Appendix F

Time-integrated Mixing Parameter

The time-integrated mixing parameter[1], χ_0, is the ratio of same-sign (SS) muon pairs from B hadron mixing over all muon pairs from B hadron decays. It is an admixture of muon pairs from B^0 and B_s mixing decays where

$$\chi_0 = f_d\chi_d + f_s\chi_s. \tag{F.1}$$

By using the fitted number of BB SS muon pairs and the corresponding number of BB opposite-sign (OS) muon pairs we should be able to extract a value for χ_0. It is important to note that there are systematic uncertainties involved in a precise measurement of χ_0 that we are not attempting to account for.

To calculate χ_0 we use the ratio of SS to OS muon pairs and the fraction of muons which decay sequentially (f_{seq}), i.e., $b \to c \to \mu$ according to

$$R = \frac{N_{bb}(SS)}{N_{bb}(OS)} = \frac{2\chi_0(1-\chi_0)[f_{seq}^2 + (1-f_{seq})^2] + 2[\chi_0^2 + (1-\chi_0)^2]f_{seq}(1-f_{seq})}{[\chi_0^2 + (1-\chi_0)^2][f_{seq}^2 + (1-f_{seq})^2] + 4\chi_0(1-\chi_0)f_{seq}(1-f_{seq})}. \tag{F.2}$$

We are allowing SS pairs in the Υ mass window to increase the statistics for the asymmetry, but these must be removed for χ_0. We use $f_{seq} = 0.102 \pm 0.015$, the value calculated from our BB Monte Carlo. The uncertainty is dominated by the uncertainty of the semileptonic branching ratios. The current world average is $\chi_0 = 0.128 \pm 0.008$ [10], and the best measurement made at the Tevatron is $\chi_0 = 0.152 \pm 0.013$ from CDF Run I. In the fitted dimuon data used for this dissertation we found $\chi_0 = 0.203 \pm 0.015$. The uncertainty is dominated by the systematic uncertainty in the fraction of sequential decays. We have not included an uncertainty for template fitting.

One concern might be that this is an indication that the fake correction of the BB fitted fraction is too small which would have a significant affect on the measured A_{CP}. In assessing systematic uncertainties on the asymmetry, we also examined χ_0. Adjusting each fake correction input by its uncertainty, we assess χ_0 still using the default correction. χ_0 is completely unchanged in each of these variations. In an effort to significantly affect χ_0, we increased the hadron/muon normalization by 50%. This effectively increases the fake rate by 50%, but it reduces χ_0 by less than 1%. The reason for such small variations in χ_0 is that to first order the fake rate is dominated by μ-fake pairs, and thus there is a proportional shift in the OS total for any change

[1] The time-integrated mixing parameter is also commonly referred to as $\overline{\chi}$, but we have reserved χ and $\overline{\chi}$ as the time-integrated mixing probabilities for neutral B and $\overline{B}$ hadrons respectively. χ_0 then is $\frac{1}{2}(\chi + \overline{\chi})$.

in the SS total. More fake muons in the BB sample means removing more $\mu^+\mu^+$ events but also means removing more $\mu^+\mu^-$ and $\mu^-\mu^+$ events. The asymmetry is affected, but χ_0 is not. Furthermore, we used the BB fake rate correction method to calculate the expected contribution of SS CC since all SS CC pairs all have at least one fake. For this we used the same species fake rates measured in the D^* data, but replaced the normalization and correlation probabilities with corresponding values from CC MC. There are 36k $\pm$ 2k predicted SS CC pairs, and the default fit finds 31k $\pm$ 2k SS CC pairs. This provides additional confirmation that a high value of χ_0 is not indicating too low of a fake correction. It could be an indication that the fitted SS CC fractions are slightly low; this possibility is discussed below. Ultimately, χ_0 is essentially decoupled from the fake correction.

Another possibility is that we are incorrectly assessing the BB fractions in the fit. Among the fitting and template variations used for cross-checks, there is some variation of BB but this often does not affect χ_0. One of the more powerful cross-checks uses templates from the correlated $b\overline{b}$ production analysis generated with HERWIG rather than PYTHIA. This check changes the BB fractions but not the asymmetry or χ_0. In addition, as shown in Figure F.1, the shape of the SS data confirms what we would expect from BB mixing, that a higher fraction of SS dimuon pairs are BB and thus higher impact parameter. If there is too much BB in the fit, it must affect the SS fit more than the OS fit to affect χ_0, and yet must still return BB fractions for SS which are larger than OS. One cross-check where this can be seen is in adding an extra PP background comprised of only fakes. This check finds lower BB fractions, higher CC fractions and returns a χ_0 consistent with previous measurements. The relative fit quality is not quite as good. The fitted raw asymmetry is 0.0159 ± 0.0070, and the full fit results are shown in Table F.1 and Figure F.2.

Finally, we performed a cross-check includes χ_0 as a constraint. The asymmetry is 0.0134 ± 0.0050 and the relative fit quality is equivalent to the default. The full fit results are shown in Table F.2 and Figure F.3. Again, the SS CC fractions are higher in this fit.

In conclusion, we find a value for χ_0 which is significantly higher than expected; we believe this result can be attributed to a high rate of fake muons in the fitted backgrounds and is only very weakly correlated with the CP asymmetry. Examining the fake correction to fitted BB events we find that χ_0 is very insensitive to any uncertainties in this calculation. We are confident that the anomalous χ_0 is not an indication that the fake removal is insufficient. Fake muons also come into this analysis as backgrounds from which the signal is isolated in the likelihood fitting. The relative weights of PB, PP, and CC (all containing fake muons) seem to be much more important to χ_0 than to the asymmetry. We have documented fitting variations that can change the value of χ_0 very significantly while leaving the asymmetry essentially unaffected. The systematic uncertainty on the asymmetry from the fitting has been assessed already, and it is relatively insignificant compared to the uncertainties from statistics and the fake correction. However, χ_0 is much more sensitive to fitting variation than the asymmetry, and would need a significant fitting systematic uncertainty if we were trying to measure it. This uncertainty would reduce the significance of any deviation in χ_0 from the world average.

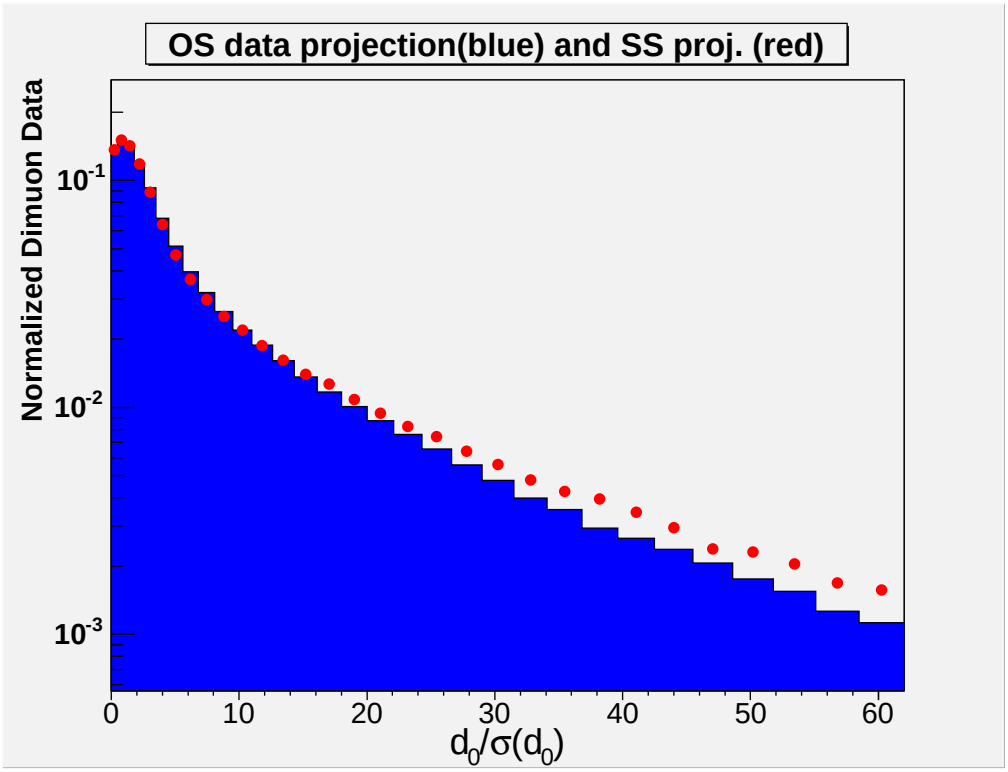

Figure F.1: Normalized OS(histogram) and SS(points) projection of data

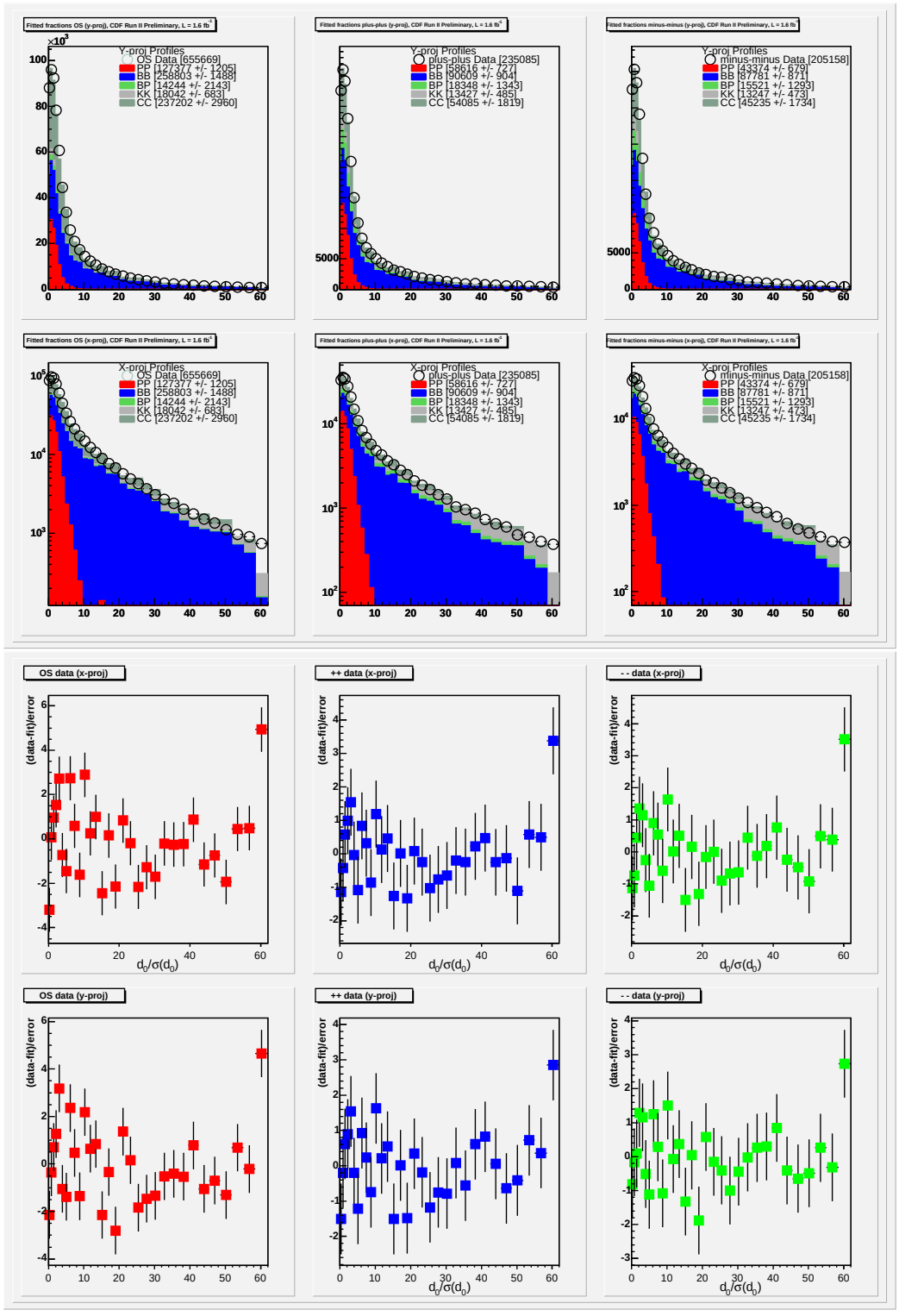

Figure F.2: Fit results for cross-check containing an additional prompt (fake hadron) background.

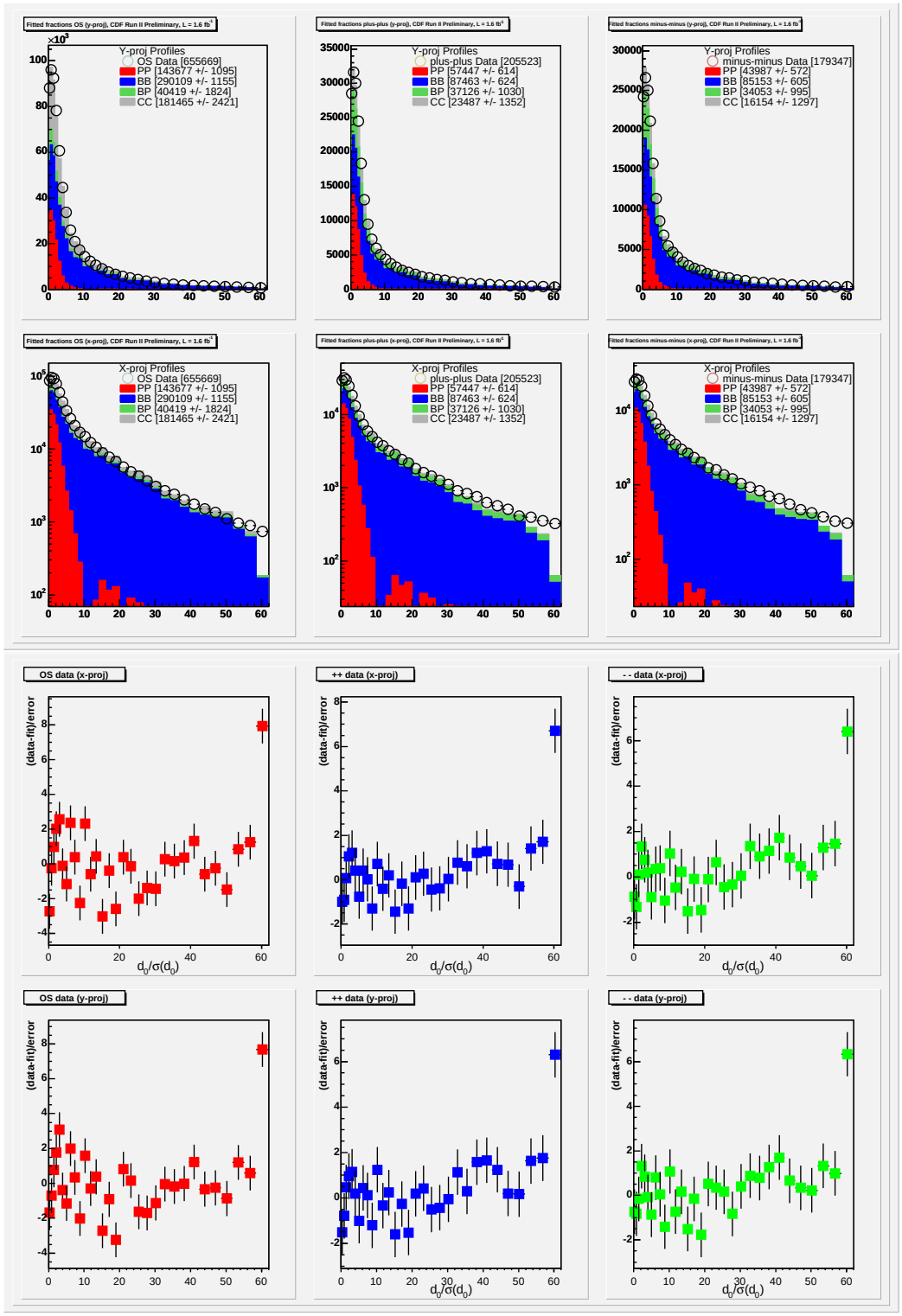

Figure F.3: Fit results for cross-check constraining χ_0

component	opposite sign ($\mu^+\mu^-$)	same-sign ($\mu^+\mu^+$)	same-sign ($\mu^-\mu^-$)
PP	19.4 ± 0.2	24.9 ± 0.3	21.1 ± 0.3
BB	39.5 ± 0.2	38.5 ± 0.4	42.8 ± 0.4
PB	2.2 ± 0.3	7.8 ± 0.6	7.6 ± 0.6
CC	36.2 ± 0.5	23.0 ± 0.8	22.0 ± 0.8
KK	2.8 ± 0.1	5.7 ± 0.2	6.4 ± 0.2

Table F.1: Additional prompt (fake hadron) background fit results. All numbers listed in percent.

component	opposite sign ($\mu^+\mu^-$)	same-sign ($\mu^+\mu^+$)	same-sign ($\mu^-\mu^-$)
PP	21.9 ± 0.2	28.0 ± 0.3	24.5 ± 0.3
BB	44.2 ± 0.2	42.6 ± 0.3	47.5 ± 0.3
PB	6.2 ± 0.3	18.1 ± 0.5	20.0 ± 0.6
CC	27.7 ± 0.4	11.4 ± 0.7	9.0 ± 0.7

Table F.2: χ_0 constraint fit results. All numbers listed in percent.

References

[1] S.W. Herb, et al., *EPhys. Rev. Lett.* **39**, 252 (1977).

[2] M. Gell-Mann, Symmetries of Baryons and Mesons, *EPhys. Rev.* **125**, 1067 (1962).
G. Zweig, Preprint CERN (1964). M. Gell-Mann, *EPhys. Lett.* **8** 214 (1964).

[3] S.L. Glashow, J. Iliopoulos, L. Maiani, *EPhys. Rev.* **D2**, 1285 (1970);

S. Weinberg, Phys. Rev. Lett. **19** 1264 (1967);

A. Salam, p.367 of *Elementary Particle Theory*, ed. N. Svartholm (Almquist and Wiksells, Stockholm, 1969).

[4] D.J. Gross, F. Wilczek, *EPhys. Rev. Lett.* **30** 1343(1973).

H.D. Politzer, *EPhys. Rev. Lett.* **30** 1346 (1973).

[5] N. Cabbibo, *EPhys. Rev. Lett.* **10**, 531 (1963).

[6] M. Kobayashi and T. Maskawa, *EProg. Theor. Phys.* **49**, 652 (1973).

[7] L.L. Chau and W.Y. Keung, *EPhys. Rev. Lett.* **53**, 1802 (1984).

[8] L. Wolfenstein, *EPhys. Rev. Lett.* **51**, 1945 (1983).

[9] Colin Gay, "B Mixing", *Annu. Rev. Nucl. Part. Sci.* 50:577-641 (2000).

[10] W.-M. Yao et al., Particle Data Group, *Review of Particle Physics, J. Phys.* **G33** (2006).

[11] I. Yu, Ph.D. Thesis, Yale University, May 1996 (unpublished).

[12] B. Aubert et al., The BABAR Collaboration, "Improved Measurement of CP Asymmetries in $B0 \to (c\overline{c})K0^*$ Decays", *EPhys. Rev. Lett.* **94** 161803 (2005).

K. Abe et al., The BELLE Collaboration, *EPhys. Rev.* **D66** 071102 (2002).

T. Affolder et al., The CDF Collaboration, "Measurement of $\sin 2\beta$ from $B \to J\Psi/K^0_S$ with the CDF detector", *Phys. Rev.* **D61**, 072005 (2000).

[13] K. Abe, et al., "Improved measurement of CP-violation parameters $\sin 2\phi_1$ and $|\lambda|$, B meson lifetimes, and $B0 - \overline{B}0$ mixing parameter Δm_d", The BELLE Collaboration, *Phys. Rev.* **D71** 072003 (2005).

B. Aubert et al., The BABAR Collaboration, *Phys. Rev.* **D73** 012004 (2006).

[14] M. Gell-Mann, A. Pais, *Phys. Rev.* **97**, 1387 (1955).

[15] K. Lande, *et al.*, *Phys. Rev.* **103**, 1901 (1956).

[16] P. Renton *Electroweak Interactions: An Introduction to the Physics of Quarks and Leptons.* Cambridge, U.K.: Cambridge University Press, (1990).

[17] M. Staric, *et al.*, The BELLE Collaboration, "Evidence for D0-D0bar Mixing", *Phys. Rev. Lett.* **98**, 211803 (2007).

[18] B. Aubert, The BABAR Collaboration,'Evidence for D0-D0bar Mixing", *Phys. Rev. Lett.* **97**, 211802 (2007).

[19] V. M. Abazov *et al.*, The D0 Collaboration, "Direct Limits on the Bs0 Oscillation Frequency," *Phys. Rev. Lett.* **97**, 021802 (2006)

[20] A. Abulencia *et al.*, The CDF Collaboration, "Observation of Bs-Bsbar Oscillations", *Phys. Rev. Lett.* **97** 242003 (2006).

[21] Baym G. *Lectures on Quantum Mechanics.* Perseus Books, Cambridge, Mass (1990).

[22] A. J. Buras, W. Slominski, and H. Steger, "$B0 - \overline{B}0$ mixing, CP violation and the B-meson decay", *Nucl. Phys.* **B238**, 529 (1984).

[23] A.D. Sakharov, "CP Symmetry Violation, C-Asymmetry and Baryonic Asymmetry of the Universe". *Pisma Zh. Eksp. Teor. Fiz.* **5** 32 (1967).

[24] I. I. Bigi et al., "CP Violation", edited by C. Jarlskog (World Scientific, Singapore, 1989).

[25] J.H. Christenson, J.W. Cronin, V.L. Fitch, R. Turlay, "Evidence for the 2π decay of the K_2^0 meson", *Phys. Rev. Lett.* **13** 138 (1964).

[26] D.H. Perkins, *Introduction to High Energy Physics, 4th ed*, Cambridge University Press, (2000).

[27] H. Burkhardt et al., NA31 Collaboration, *Phys. Lett.* **B206** 169 (1988).
V. Fanti et al., NA48 Collaboration, *Phys. Lett.* **B465** 335 (1999).
A. Alavi-Harati et al., KTeV Collaboration, *Phys. Rev. Lett.* **83** 22 (1999).

[28] Y. Grossman, *et al.*, "CP Violation Beyond the Standard Model", *Heavy Flavors II, Advanced Series on directions in High Energy Physics*, 15 (1998).

[29] D. Acosta et al., CDF Collaboration, "First Evidence for $B_s^0 \to \phi\phi$ Decay and Measurements of Branching Ratio and A_{CP} for $B^+ \to \phi K^+$", *Phys. Rev. Lett.* **95** 031801 (2005).

[30] B. Aubert et al., BaBar Collaboration, "Direct CP Violating Asymmetry in $B0 \to K^+\pi^-$ Decays", *Phys. Rev. Lett.* **93** 131801 (2004).

[31] B. Aubert, The BABAR Collaboration, "Search for T and CP Violation in $B^0 - \overline{B}^0$ Mixing with Inclusive Dilepton Events.", *Phys. Rev. Lett.* **88** 231801 (2002).

[32] V. M. Abazov et al., The D0 Collaboration, "Combined D0 Measurements Constraining the CP-violating Phase and Width Difference in the B_s^0 System", hep-ex/0702030v1, FERMILAB-PUB-07/044-E.

[33] Y. Grossman, Y.Nir, and G. Raz, "Constraining the Phase of $B_s - \overline{B_s}$ Mixing", *Phys. Rev. Lett.* **97** 151801 (2006).

[34] M. Beneke, G. Buchalla, A. Lenz and U. Nierste, *Phys. Lett.* **B576**, 173 (2003).

[35] I. Dunietz, R. Fleischer, and U. Nierste, "In Pursuit of New Physics with B_s Decays", *Phys. Rev.* **D63** 114015 (2001).

[36] R. D. Fields, "The Sources of b-Quarks at the Tevatron and their Correlations", *Phys. Rev.* **D65**, 094006, (2002).

[37] CDF II Collaboration. The CDF Run II Technical Design Report. FERMILAB-Pub-96-390-E (1996).

[38] A. Affolder et al. CDF Central Outer Tracker. *Nucl.Instrum.Meth.* **A526** 249-299, (2004).

[39] SVX-II: CDF Run II Silicon Tracking Projects by A. Sill. 2000. Prepared for 8th International Workshop on Vertex Detectors (Vertex 99), Texel, Netherlands, 20-25 June 1999. *Nucl. Instrum. Meth.* **A447** 1-8, (2000).

[40] A. Artikov et al. Design and construction of new central and forward muon counters for CDF II submitted to *Nucl. Instrum. Meth.* (available online Oct. 12, 2004).

[41] D. Acosta et al. The CDF Cherenkov Luminosity Monitor. *Nucl. Instrum. Meth.*, **A461** 540-544, (2001).

[42] D. Acosta et al. A Time-Of-Flight Detector in CDF-II. *Nucl. Instrum. Meth.* **A518** 605-608, (2004).

[43] R. Downing et al., Track Extrapolation and Distribution for the CDF-II Trigger System. *Nucl. Instrum. Meth.* **A570** 36-50, (2007).

[44] E.J. Thomson et al., FERMILAB-CONF-02/144-E (CDF Note 5990) (2002).

[45] W. Ashmanskas et al. Performance of the CDF Online Silicon Vertex Tracker. *IEEE Trans. Nucl. Sci.*, **49** 1177-1184, (2002).

[46] "Run II XFT Linker Design Specification,"
http://www.physics.ohio-state.edu/~hughes/xft/linker/doc/linker_spec.ps

[47] T. Aaltonen et al., The CDF Collaboration, "Observation and mass measurement of the baryon Xi(b)-" *Phys. Rev. Lett.* **99** 052002 (2007).

[48] A. Abulencia et al., The CDF Collaboration, "Observation of Bs-¿K+K- and Measurements of Branching Fractions of Charmless Two-body Decays of B0 and Bs Mesons in p-pbar Collisions at sqrt(s)=1.96 TeV" *Phys. Rev. Lett.* **97**, 211802 (2006).

[49] B.Aubert et al., The Babar Collaboration, *Phys. Rev. Lett.* **88**, 231801 (2002).

[50] D. Jaffe et al., The CLEO Collaboration, *Phys. Rev. Lett.* **86**, 5000 (2001).

[51] I. Yu et al., "SEARCH FOR CP VIOLATION IN LOW PT DIMUON EVENTS", CDF note 3113; F. Abe et al., The CDF Collaboration, *Phys. Rev.* **D55**, 2546 (1997).

[52] K. Ackerstaff et al., The OPAL Collaboration, *Z. Phys.* **C76** 401 (1997).

[53] R. Barate, et al., The ALEPH Collaboration, *Eur. Phys.* **J C20** 431 (2001).

[54] V. Abazov et al., The D0 Collaboration, "Measurement of the CP-violation parameter of B^0 mixing and decay with $p\overline{p} \to \mu\mu X$ data", *Phys. Rev.* **D74** 092001 (2006).

[55] D. Acosta et al., The CDF Collaboration, "Measurement of the Average Time-Integrated Mixing Probability of b-Flavored Hadrons Produced at the Tevatron", *Phys. Rev.* **D69** 012002 (2004).

[56] A. Annovi et al., "Measurement of Correlated $b\overline{b}$ Production in $p\overline{p}$ Collisions at $\sqrt{s}$ = 1960 GeV", CDF Note 8733, (2007).

[57] A. Taffard, "Run II Cosmic Ray Tagger", CDF note 6100.

[58] T. Sjstrand et al., "High-Energy-Physics Event Generation with PYTHIA 6.1", *Comput. Phys. Commun.* **135** 238 (2001).

[59] D.J. Lange, "The EvtGen particle decay simulation package", *Nucl. Instrum. Meth.* **A462** 152 (2001).

[60] S. Agostinelli et al., "GEANT4 - A simulation toolkit", *Nucl. Instr. and Meth.* **A506** 250 (2003).

[61] F. James. "MINUIT, A package of programs to minimize a function of n variables, compute the covariance matrix, and find the true errors" program library code D507, CERN, (1978).

[62] J. Heinrich, *In the Proceedings of PHYSTAT2003: Statistical Problems in Particle Physics, Astrophysics, and Cosmology, Menlo Park, California, 8-11 Sep 2003, pp MOCT001*

[63] E. Berry et al., "Study of Muon Matching Efficiencies and Mistag Rates", CDF note 8042.

[64] D.Glenzinski et al., "Measurement of Level 1, 2 and 3 low p_T dimuon efficiencies for the $B_s \to \mu\mu$ analysis", CDF note 7314.

[65] http://www-cdf.fnal.gov/internal/physics/bottom/b-montecarlo/instructions-5_3_4.html

[66] D. Acosta, et al. The CDF Collaboration, "Measurement of the Lifetime Difference Between B_s Mass Eigenstates", *Phys. Rev. Lett.* **94** 101803 (2005). (Updated in CDF Public Note 8950).